Experimental Tests of Electroweak Theory with $\mu^+\mu^-$ and $\mu^+\mu^-\gamma$ Final States from e^+e^- Annihilation

Thesis by

Hong Ma

In Partial Fulfillment of the Requirements

for the Degree of

Doctor of Philosophy

California Institute of Technology

Pasadena, California

1988

(submitted Feb 2, 1988)

Acknowledgements

This thesis was only possible because of the successful construction and operation of the MARK J experiment over a period of more than 8 years by the members of the collaboration. I would like to thank all of them for their contributions, from which I benefitted.

I would like to take this opportunity to thank Prof. Harvey Newman, my thesis advisor, for his support and help during my study both at DESY and at Caltech. He has given me many suggestions and corrections throughout the course of this work, and has taught me a great deal of physics along the way.

It has been a great pleasure and an invaluable experience to work in the MARK J experiment at DESY. I thank Prof. Samuel C. C. Ting for his outstanding leadership in building the detector, running the experiment and understanding the resulting physics questions. I wish to thank Prof. M. Chen, Prof. A. Böhm and Prof. R. Rau for their helpful and stimulating discussions and advice. From the discussions with Dr. Carlos Maña, I greatly improved my knowledge of the electroweak theory. Special thanks to Dr. Renyuan Zhu, with whom I worked at Caltech, for the help and numerous interesting discussions.

Various communications with my colleagues at DESY proved to be beneficial. In particular, I thank, Drs. M. Marguina, M. Martinez, J. Muich, S. Rodriguez, H. Stone, H. G. Wu, S. X. Wu, B. Zhou, for the work we fulfilled, the knowledge we gained and the joy we shared together.

I would also like to acknowledge the DESY directorate for their hospitality during my stay at DESY, and the PETRA Machine Group for the excellent performance of PETRA. Support for this research was partially provided through a Department of Energy Contract, DE-AC03-81-ER40050.

Last, but not least, my thanks to my parents and all members of my family for their continuous support and love, to which I will forever be indebted.

Abstract

The MARK J detector at PETRA was used in an experimental study of $\mu^+\mu^-$ and $\mu^+\mu^-\gamma$ events. Data were collected at the center of mass energy range from 14 to 46 GeV. The standard model of electroweak interactions has been tested by the data with high statistics. Stringent limits on the extensions of the standard model have been derived.

The rate and angular distribution of muon pair events have been measured and are found to be in good agreement with the standard model. The R-value and charge asymmetry of the muon pairs are used to determine the electroweak parameters. For $M_Z = 93$ GeV, we find, $\sin^2\theta_w = .20^{+.04}_{-.025}$. Assuming e-μ universality, the lepton coupling constants are, $g_A^2 = .265 \pm .032$, $g_V^2 = 0.038 \pm .043$. Special emphasis has been placed on the understanding of the radiative effects by studying acollinear muon pairs and $\mu^+\mu^-\gamma$ events. This provides a test of the electroweak theory to higher than leading order. Various distributions of $\mu^+\mu^-\gamma$ events have been compared to the standard model predictions. The data and electroweak theoretical predictions are in excellent agreement.

Investigations have been carried out to constrain various non-standard processes and to search for new particles. Limits are set on the cutoff parameters, mass and coupling of excited muons, four fermion contact interaction, etc.. Muons can be regarded as pointlike particles down to a distance of $8\times10^{-17}cm$. The pair production of excited muons is limited by the $\mu^+\mu^-\gamma\gamma$ event analysis, and the μ^* mass is expected to be greater than 23 GeV at 95% confidence level. The fact that there is no excess in the production of $\mu^+\mu^-\gamma$ events gives a tight constraint on the single production of excited muons.

Our results are compared to other experiments and the status of experimental tests of the standard model is summarized. Perspectives of testing the standard model in the near future at LEP are discussed. Precision measurements of quantities such as the gauge boson masses, widths and various asymmetries will confront the standard model with more stringent constraints and/or reveal new physics.

Contents

List of Tables

List of Figures

Chapter 1

Introduction

The outline of this thesis is as follows. Chapter 1 gives a brief review of the theory and remarks on experimental tests of electroweak theory in general. Detailed theoretical predictions for $e^+e^- \rightarrow \mu^+\mu^-(\gamma)$ are given in Chapter 2. Chapter 3 describes the Mark J detector at PETRA with the emphasis on the muon spectrometer and the electromagnetic calorimeter. Although the hadron calorimeter is an important part of the detector, it is not discussed because it is not directly relevant to this analysis. Chapter 4 reports the results from the analysis of the muon pair ($\mu^+\mu^-$) final states, which tests the standard model and gives the measurements of the electroweak parameters. Chapter 5 reports on the results from the analysis of hard radiative dimuon ($\mu^+\mu^-\gamma$) final states, which tests the theory to a higher order. A search for possible excited states of muons is reported in Chapter 6, based upon the study of $\mu^+\mu^-\gamma$ events. Comparison with the limits obtained with (g-2) measurements is also given. Conclusions are drawn in Chapter 7, where our results are also compared to that of other experiments. Chapter 8 presents some experimental tests of the standard model that will be carried out at LEP in the near future.

1.1 Review of the Theory

One of the most successful advances in elementary particle physics in the recent past has been the theoretical development and the experimental confirmation of the electroweak gauge theory based on $SU_L(2)\otimes U_Y(1)$ model (frequently referred to as the standard model) from Glashow [1], Weinberg [2] and Salam [3].

The electromagnetic interactions of elementary particles are described by Quantum Electrodynamics (QED), which is based on the gauge group U(1). The boson mediating the interactions is generated when local gauge invariance of the Lagrangian is required. It explains many important electromagnetic interaction phenomena, such as the scattering of charged particles and the anomalous magnetic moment of electrons and muons.

It has been over 50 years since the first weak interaction theory was invented by Fermi [4] to explain the β decay of nuclei. Like QED, which was formulated a decade later, the Fermi theory was based upon the current-current interaction (although the concept of the propagator was missing). It was further developed into a (V-A) weak interaction theory when the parity violating nature of the weak interaction was proposed and verified [5,6]. A great amount of experimental and theoretical knowledge on the nature of weak interactions at low energy has been derived from the study of nuclear β-decay, muon capture, muon decay and semileptonic decays of low mass mesons and baryons.

It was known, however, that the current-current theory had to be modified at high energies because of the violation of unitarity. The standard model which unifies the electromagnetic and weak interaction assumes that $SU_L(2)\otimes U_Y(1)$ is the fundamental gauge group of the electroweak interaction. The left-handed fermions are isospin (commonly called "weak isospin") doublets under $SU_L(2)$ transformations, while the right-handed fermions are isospin singlets. The assignment of isospin and

Fermion	ν_L	e_L	e_R	u_L	d_L	u_R	d_R
Q	0	-1	-1	2/3	-1/3	2/3	-1/3
Y	-1	-1	-2	1/3	1/3	4/3	-2/3
T_3	1/2	-1/2	0	1/2	-1/2	0	0

Table 1.1 Quantum numbers of leptons and quarks of the first family.

hypercharge of the fermions are given in Table 1.1 .

The two subgroups are further related by the electric charge of the particles.

$$Q = T_3 + \frac{Y}{2} \tag{1.1}$$

where T_3 is the third component of the isospin of $SU_L(2)$, and Y is the hypercharge of U(1). The intermediate bosons are introduced by applying the local gauge invariance of the fields. The theory would not be acceptable to describe the weak interaction if the symmetry were exact because most of the particles in nature are massive. It was the discovery of Higgs mechanism [7,8] that made it possible for a gauge theory to be a theory of the weak interaction. After a Lagrangian is constructed with massless fermions , vector bosons and scalar Higgs so as to be invariant under a gauge group, a specific Higgs potential is chosen to spontaneously break the symmetry to generate the masses for the fermions and bosons with the exception of photon and neutrinos.

The Lagrangian of the electroweak interaction can be written as :

$$L = L_0 + L_{int} + L_h \tag{1.2}$$

where

$$L_0 = \bar{\Psi}(i\gamma^\mu\partial_\mu)\Psi - \frac{1}{4}\mathrm{W}_{\mu\nu}\cdot\mathrm{W}^{\mu\nu} - \frac{1}{4}B_{\mu\nu}B^{\mu\nu}, \tag{1.3}$$

$$L_{int} = -g\bar{\chi}_L\gamma_\mu\mathrm{T}\cdot\mathrm{W}^\mu\chi_L - g'\bar{\chi}_L\gamma_\mu\frac{Y}{2}\chi_L B^\mu - g'\bar{\Psi}_R\gamma_\mu\frac{Y}{2}\Psi_R B^\mu, \tag{1.4}$$

$$L_h = \mid(i\partial_\mu - g\mathrm{T}\cdot\mathrm{W}_\mu - g'\frac{Y}{2}B_\mu)\Phi\mid^2 - V(\Phi) \tag{1.5}$$

$$-(G_1\bar{\chi}_L\Phi\Psi_R + G_2\bar{\Psi}_R\Phi_c\chi_L + h.c.), \tag{1.6}$$

where $\mathbf{W}^\mu$ and B^μ are the vector bosons, and

$$\mathbf{W}_{\mu\nu} = \partial_\mu \mathbf{W}_\nu - \partial_\nu \mathbf{W}_\mu - g\mathbf{W}_\mu \times \mathbf{W}_\nu \tag{1.7}$$

$$B_{\mu\nu} = \partial_\mu B_\nu - \partial_\nu B_\mu \tag{1.8}$$

χ_L is an isospin doublet for the left-handed fermions, e.g.,

$$\chi_L = \begin{pmatrix} \nu \\ e \end{pmatrix}_L \text{ or } \begin{pmatrix} u \\ d \end{pmatrix}_L \ldots \tag{1.9}$$

Ψ_R is the isospin singlet for a right-handed fermion:

$$\Psi_R = e_R, \ u_R \ or \ d_R \ \ldots \tag{1.10}$$

Φ is the Higgs field; L_0 is the Lagrangian for free field; L_{int} governs the interaction between the fermion fields and the intermediate vector boson fields; L_h is the interaction between Higgs and the fermions or bosons, which is responsible for the generation of the masses of these particles; $h.c.$ stands for hermitian conjugate; Φ_c is the charge conjugate state of the Higgs field; G_1, G_2 are fermion-Higgs coupling constants adjusted to give the physical mass of the fermions.

The photon and the weak neutral intermediate boson are mixtures of the bosons in the bare theory, which are identified as:

$$A_\mu = \cos\theta_w B_\mu + \sin\theta_w W_\mu^3 \tag{1.11}$$

$$Z_\mu = -\sin\theta_w B_\mu + \cos\theta_w W_\mu^3 \tag{1.12}$$

where $\tan\theta_w = g'/g$. The electric charge of an electron is $e = g\sin\theta_w = g'\cos\theta_w$.

In the standard model, the Higgs field is chosen to be an isospin doublet with weak hypercharge Y=1. After the spontaneous symmetry breakdown, the Higgs field takes the form,

$$\Phi = \frac{1}{\sqrt{2}} \begin{pmatrix} 0 \\ v + h(x) \end{pmatrix}, \tag{1.13}$$

where v is the vacuum expectation value of the Higgs field.

Only one component of the field remains while three other components are eliminated by the gauge transformation, giving the degrees of freedom to the longitudinal components of the three massive intermediate bosons.

The masses of the fermions and bosons are therefore,

$$M_Z = \frac{1}{2}v\sqrt{g^2+g'^2}, \tag{1.14}$$

$$M_W = \frac{1}{2}vg, \tag{1.15}$$

$$m_e = \frac{G_1 v}{\sqrt{2}}, \tag{1.16}$$

and

$$\sin^2\theta_w = 1 - \frac{M_W^2}{M_Z^2} \tag{1.17}$$

A higher level of understanding in physics is reached when two seemingly unrelated classes of interactions are unified. One of the most important predictions of the standard model is the existence of the weak neutral current. It is by this specific structure of neutral current that the standard model is distinguished from other gauge models of electroweak theories.

1.2 Earlier experimental tests of electroweak theory

Two kinds of tests of the standard model have been carried out since the 70's, the measurement of the neutral current parameters and the direct observation of the W and Z bosons.

A lot of experimental efforts were devoted to searches for the existence of the neutral current and to studies of its structure. The first evidence of the neutral current came in 1973 in a bubble chamber at CERN [9,10]. Since then, it has been measured in various interactions of lepton and quarks, such as ν_μ-e, ν_e-e, ν_μ-N, polarized electron-deuteron, polarized muon-carbon, e^+e^- scattering and annihilation, and etc..

W's and Z's have been produced in high energy $\bar{p}p$ collisions and have been unambiguously identified in their leptonic decay modes [11,12,13,14]. The experimental signature of the W boson is an isolated electron (or muon or tau) with large transverse momentum, associated with large missing transverse momentum, which is presumably the transverse momentum of the undetected neutrino. The decay modes of $Z \rightarrow e^+e^-$ or $\mu^+\mu^-$ are clear signals for the production of Z with very low background. The production properties of the W and Z boson, such as the cross sections and the angular distribution of electrons in the W rest frame, have also been studied and have been found to be consistent with the standard model [15,16].

The masses of the W and Z bosons have been measured in their productions in $\bar{p}p$ collisions with about 2–3% accuracy. $\sin^2\theta_w$ can be evaluated in a straightforward way by inserting both of the masses in Eq 1.17. A more precise value can be obtained if the Fermi coupling constant measured by muon lifetime is used. However, electroweak corrections must be taken into account in order to relate the low-Q^2 region (where G_F and α are measured) to the $Q^2 \sim M_Z^2$ region:

$$\sin^2\theta_w = \frac{\pi\alpha}{\sqrt{2}G_F(1-\Delta r)M_W^2}, \tag{1.18}$$

$$\Delta r = 0.0696 \pm 0.002, \tag{1.19}$$

where Δr is the radiative correction and is slightly dependent on the top and Higgs masses (see Chapter 8).

Neutrino experiments have played important roles in studying the neutral currents. The statistically most significant process is ν_μ–N scattering. Precise determinations of $\sin^2\theta_w$ have been obtained by electronic detectors [17,18,19], supplanting earlier bubble chamber experiments which had lower statistics. In order to reduce the systematic error, the ratio of the neutral current cross section to the charged current cross section is used to determine $\sin^2\theta_w$. Using the quark parton model description of the nucleon structure, the ratios for the isoscalar target can be written

as [20],

$$R_\nu = \frac{\sigma_\nu^{NC}}{\sigma_\nu^{CC}} = \frac{1}{2} - \sin^2\theta_w + \frac{5}{9}\sin^4\theta_w(1+r), \tag{1.20}$$

$$R_{\bar{\nu}} = \frac{\sigma_{\bar{\nu}}^{NC}}{\sigma_{\bar{\nu}}^{CC}} = \frac{1}{2} - \sin^2\theta_w + \frac{5}{9}\sin^4\theta_w(1+\frac{1}{r}), \tag{1.21}$$

$$r = \frac{\sigma_{\bar{\nu}}^{CC}}{\sigma_\nu^{CC}}. \tag{1.22}$$

For r=0.4 (near the experimentally measured value), ν_μ–N scattering data are more sensitive to $\sin^2\theta_w$ than that of $\bar{\nu}_\mu$–N scattering.

Although statistically less significant, neutrino-electron scattering serves as a unique process for the determination of the signs of the weak neutral current coupling constants of the leptons. Assuming $g_L^\nu = 1/2$ and $g_R^\nu = 0$, the cross sections of all the neutrino-electron scattering processes can be written as,

$$\frac{d\sigma}{dy} = \frac{G_F^2 s}{\pi}[A + B(1-y^2) + Cy], \tag{1.23}$$

where $s = 2m_e/E_\nu$, $y = E_e/E_\nu$ and C can be neglected for high energy neutrino experiments. A and B can be expressed in terms of helicity couplings for various elastic processes,

	A	B
$\nu_\mu e$	$g_L^{e\,2}$	$g_R^{e\,2}$
$\bar{\nu}_\mu e$	$g_R^{e\,2}$	$g_L^{e\,2}$
$\nu_e e$	$(g_L^e + 1)^2$	$g_R^{e\,2}$
$\bar{\nu}_e e$	$g_R^{e\,2}$	$(g_L^e + 1)^2$

The measured cross sections of these processes give a constraint of the allowed regions on g_L^e–g_R^e plane (or on g_A^e–g_V^e plane as presented in chapter 7) with an elliptical shape. Although the measurement of the cross section of each process is not sufficient to determine both coupling constants simultaneously, combined data from all neutrino-electron scattering processes together with the e^+e^- experiments or the charged lepton scattering experiments, however, have been used successfully to determine the coupling constants including the signs.

ν_μ-e scattering has been studied in a few experiments [21,22]. Given the many systematic uncertainties inherent in the cross section evaluations, a measurement of the ratio,

$$R = \frac{\sigma(\nu_\mu e)}{\sigma(\bar{\nu}_\mu e)} = \frac{1+\eta+\eta^2}{1-\eta+\eta^2}, \tag{1.24}$$

has been used, with $\eta = 1 - 4\sin^2\theta_w$. This gives a sensitive measurement of $\sin^2\theta_w$ while eliminating some of the systematics (such as the experimental acceptance).

The formula quoted above only takes into account the lowest order contribution to the scattering. When extracting $\sin^2\theta_w$ from the neutrino scattering data , radiative corrections have to be applied [23].

The first observation and cross section measurement of $\nu_e + e^- \rightarrow \nu_e + e^-$ was reported in 1985 [24]. Though low in statistics, it helps to determine the sign of the coupling constants. A more interesting study of this process is the destructive interference between charged and neutral currents [25].

The most precise measurement of $\sin^2\theta_w$ before 1980 came from the polarized electron scattering from deuterons [26], where the parity violating asymmetry was found. Since the electromagnetic interaction conserves parity, the parity nonconserving asymmetry is attributed to the interference between the electromagnetic current and the neutral current interaction.

In the next chapter, we discuss the properties of $\mu^+\mu^-$ and $\mu^+\mu^-\gamma$ production from e^+e^- annihilation based on the standard model. Most of the experimental results on the electroweak parameters are summarized in chapter 7.

Chapter 2

$\mu\mu(\gamma)$ from e^+e^- annihilation

High energy e^+e^- colliding machines provide unique opportunities to study the electroweak effects. Until now, the statistically most significant data on electroweak interference come from muon pair production.

2.1 $\mu^+\mu^-$ from e^+e^- annihilation

Using perturbation theory, we first consider the lowest order contribution to the $\mu^+\mu^-$ final state. The tree level Feynman diagrams of $\mu^+\mu^-$ production in e^+e^- collision are given in Fig 2.1. The first one is a QED process of one photon exchange, and the second one is the exchange of the weak neutral boson, Z°.

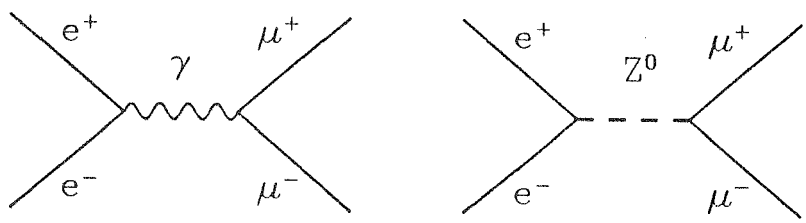

Figure 2.1 The lowest order Feynman diagrams of muon pair production.

The Lagrangian of the process can be written as:

$$L = -\frac{g}{\cos\theta_w}\bar{\Psi}\gamma^\mu\frac{1}{2}(g_V - g_A\gamma^5)\Psi Z_\mu - Qe\bar{\Psi}\gamma^\mu\Psi A_\mu, \tag{2.1}$$

where

$$g_V = T_3 - 2Q\sin^2\theta_w, \tag{2.2}$$

$$g_A = T_3, \tag{2.3}$$

are the vector and axial coupling constants of the fermion to the neutral current given in Table 2.1.

Fermion	g_A^f	g_V^f	g_V^f ($\sin^2\theta_w = .22$)
e^-, μ^-, τ^-	$-1/2$	$-\frac{1}{2} + 2\sin^2\theta_w$	-0.060
u, c	$+1/2$	$+\frac{1}{2} - \frac{4}{3}\sin^2\theta_w$	$+0.207$
d, s, b	$-1/2$	$-\frac{1}{2} + \frac{2}{3}\sin^2\theta_w$	$-.353$

Table 2.1 $Zf\bar{f}$ **vertex coupling constants in the standard model.**

The QED process gives the cross section as:

$$\frac{d\sigma^{QED}}{d\Omega^{\mu\mu}} = \frac{\alpha^2}{4s}(1+\cos^2\theta), \quad \text{or} \tag{2.4}$$

$$\sigma_{\mu\mu}^{QED} = \frac{4\pi\alpha^2}{3s}. \tag{2.5}$$

Taking into account the weak interaction and electroweak interference, the cross section becomes,

$$\frac{d\sigma}{d\Omega} = \frac{\alpha^2}{4s}(F_1(1+\cos^2\theta) + F_3\cos\theta), \quad \text{where} \tag{2.6}$$

$$F_1 = Q_f^2 - 2Q_f Re(\chi)g_V^e g_V^f + |\chi|^2 (g_A^{e2} + g_V^{e2})(g_A^{f2} + g_V^{f2}), \tag{2.7}$$

$$F_3 = -4Q_f Re(\chi)g_A^e g_A^f + 8|\chi|^2 g_A^e g_V^e g_A^f g_V^f, \tag{2.8}$$

$$\chi = \frac{1}{4\sin^2\theta_w\cos^2\theta_w}\cdot\frac{s}{s - M_Z^2 + iM_Z\Gamma_Z}$$

$$= \frac{\rho G_F M_Z^2}{2\sqrt{2}\pi\alpha} \cdot \frac{s}{s - M_Z^2 + iM_Z\Gamma_Z}, \tag{2.9}$$

$$\rho = \frac{M_w^2}{M_Z^2 \cos^2\theta_w}, \tag{2.10}$$

and Γ_Z is the width of Z^0. The ratio of total cross section to the QED cross section is therefore,

$$R = \frac{\sigma^{tot}}{\sigma_{\mu\mu}^{QED}} = F_1. \tag{2.11}$$

The formulae are valid for all fundamental massless fermions, both leptons and quarks with the exception of electron because of the additional t-channel Feynman diagrams. The forward-backward charge asymmetry of the muon pair production is defined as,

$$A_{FB}^{\mu\mu} = \frac{\int_0^{\frac{\pi}{2}} \frac{d\sigma}{d\Omega} d\Omega - \int_{\frac{\pi}{2}}^{\pi} \frac{d\sigma}{d\Omega} d\Omega}{\int_0^{\pi} \frac{d\sigma}{d\Omega} d\Omega}. \tag{2.12}$$

An event with angle between the negative muon and the electron, of less (greater) than 90° is a forward (backward) event. This is equivalent to defining forward and backward events according to the angle between the positive muon and the positron using the same criterion. Neglecting g_V^2, which is small for $\sin^2\theta_w$ near 1/4, we have,

$$A_{FB}^{\mu\mu} = \frac{3g_A^e g_A^f}{8\sin^2\theta_w \cos^2\theta_w} \cdot \frac{s}{s - M_Z^2}$$

$$= \frac{3\rho G_F}{4\sqrt{2}\pi\alpha} \cdot \frac{m_z^2 s}{s - M_Z^2} \cdot g_A^e g_A^f. \tag{2.13}$$

Because the vector coupling of the muon is rather small, the weak effect on the total cross section is hardly detectable. However, the charge asymmetry of the muon angular distribution is rather large in the high Q^2 range of PETRA. At $\sqrt{s}$ = 44 GeV, R = 1.0083 and $A_{FB}^{\mu\mu}$ = -15.6%.

Fig 2.2 shows the total cross section and the asymmetry as a function of the center of mass energy. It has to be noted that the position of the peak of the cross

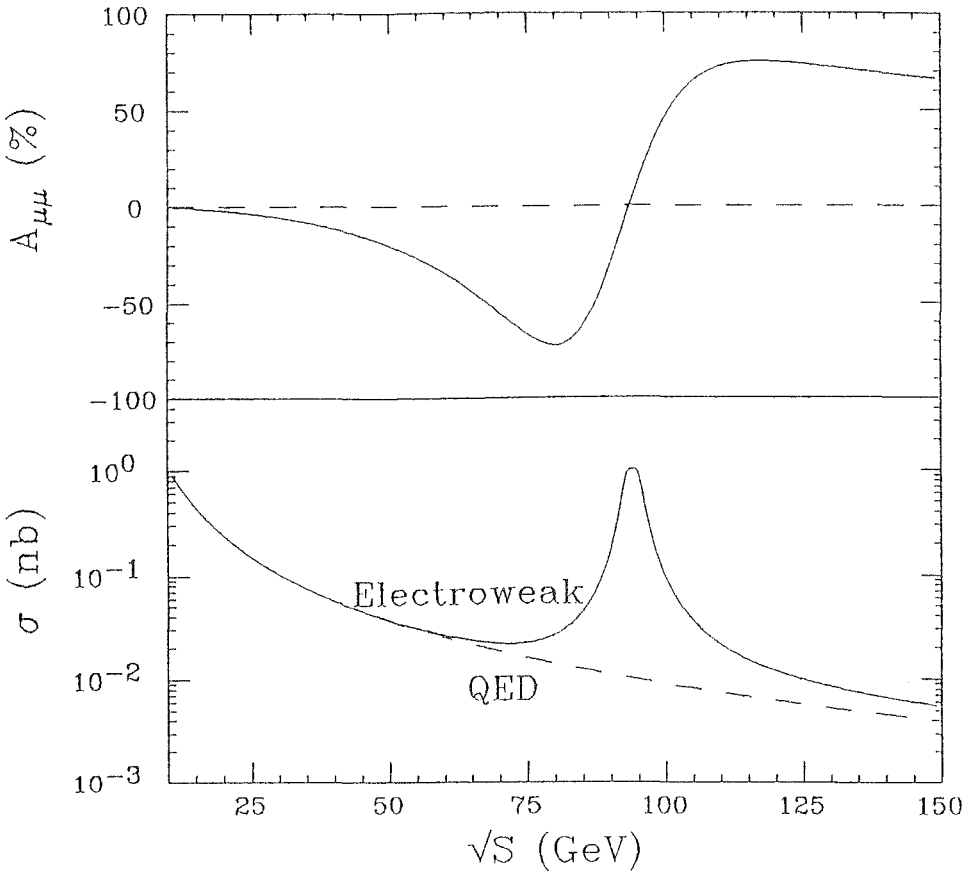

Figure 2.2 The lowest order cross section and asymmetry of $\mu^+\mu^-$ events as a function of center of mass energy.

section and the zero of the asymmetry will be shifted if the radiative corrections are taken into account, which become non-negligible when the center of mass energy approaches the mass of the weak neutral boson [27].

In contrast with other experimental tests of the electroweak theory, such as lepton nucleus scattering, and direct Z and W production from $\bar{p}p$ collisions, $e^+e^- \rightarrow \mu^+\mu^-(\gamma)$ cross section and asymmetry measurements over a large high-Q^2 range provide a sensitive test of the electroweak theory which is independent of the details of the nuclear structure.

2.2 Radiative corrections to $\mu^+\mu^-$ events

In order to perform a high precision test of the theory, higher order processes, such as those in Fig 2.3 with internal loops, that may also contribute to the same final state have to be well understood. Besides, those final states, such as those in Fig 2.3 with soft external photons, that can not be distinguished from the lowest order $\mu^+\mu^-$ final state because of the finite detector resolution in the experiment also have to be understood. Higher order contributions modify the cross section as well as the charge asymmetry depending on the kinematic cuts applied to the phase space [28,29]. With radiative corrections included, the asymmetry comes not only from the electroweak interference, but also from the interference of the two and one photon exchange diagrams (Fig 2.3a), the interference of the initial and final state radiation (Fig 2.3b) and etc.. Basically, in QED any interference between different charge conjugate (C) states of the muon pairs will contribute to the charge asymmetry. Since C is conserved in the QED interaction and the photon has C=-1, a muon pair from the one photon annihilation has C=-1 while a muon pair from two photon exchange has C=+1. A similar argument applies in the case of muon pairs with initial and final state photon radiation.

With the data collected at PETRA and PEP, the asymmetry is already sensitive to electroweak radiative corrections. Therefore in order to extract the Born term asymmetry of the electroweak interference from the data, a good understanding of the radiative corrections in the theory is necessary. In recent years, many efforts in theory have been made in understanding and calculating the radiative effects [30,31,32,29,33].

The renormalizability of the standard model was proved in 1971 by 't Hooft [34]. This means that those parts occurring in the evaluation of Feynman diagrams of higher order which without regulation would become ultraviolet divergent can

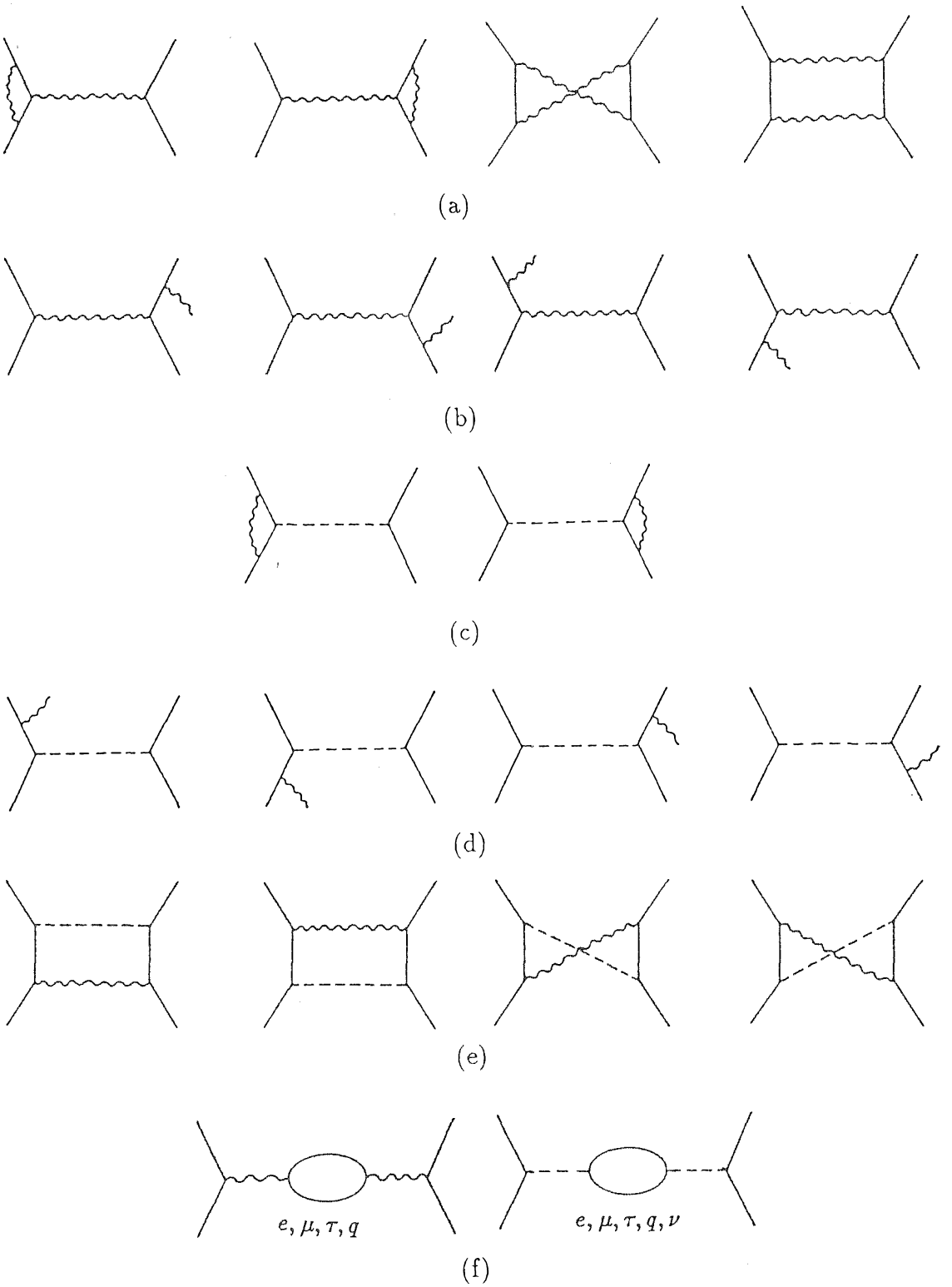

Figure 2.3 The Feynman diagrams of the radiative processes considered up to the order of g^3.

	$A_{FB}(\%)$ Intermediate	$A_{FB}(\%)$ on-shell
Born	-9.271	-8.64
Photon self energy (without fermion loops)	.0005	.0005
Z self energy	0.034	-.617
γZ mixing	-.003	-5×10^{-6}
Vertex corrections	.013	.012
Box diagram	-.012	-.010
Born+weak	-9.238	-9.257
QED	1.904	1.744
Full	-7.334	7.513

Table 2.2 The forward-backward asymmetry for $\sqrt{s} = 34.5$ GeV and $\cos\theta \leq 1.0$. The photon radiation is included with $\delta E/E_b \leq 0.1$.

be absorbed by the renormalization of the fields and the couplings. The choice of the renormalized parameters and their definition via measurable quantities is not unique beyond the tree level. Several different schemes exist in literature [35] giving somewhat different radiative corrections to the asymmetry due to the fact that there is a difference already evident in the schemes at the tree level. The asymmetry calculated from different schemes is consistent when, and only when higher order corrections are included [33]. Two commonly used schemes select the input parameters as follows,

- on shell scheme: e, M_W, M_Z, M_H *and* m_f
- intermediate scheme: e, G_F, M_Z, M_H *and* m_f

The tree level asymmetry calculated from the intermediate scheme is 7% larger in magnitude than that from the on shell scheme. However, the asymmetry after full

electroweak corrections is consistent up to higher order corrections. Table 2.2 shows the contributions from various processes to the asymmetry in these two different schemes. Further weak corrections at one loop level, such as two weak gauge boson exchange or Higgs boson exchange, are negligible because of the suppression either by the small coupling or relatively low momentum transfer.

In this analysis the on shell scheme is used. In this scheme, the weak corrections to the asymmetry, which is mainly from the Z self energy, is not negligible. Because the weak corrections have already been included in the definition of G_F, the weak corrections to the asymmetry in the intermediate scheme is negligible.

Fig 2.3 summarizes all the diagrams of the processes that have been taken into account up to the order of α^3. The cross sections of the processes are calculated analytically. The Monte Carlo event generator based on the cross sections of the diagrams in Fig 2.3 is used in this analysis [28,30,31]. To study the variations of the distributions of various quantities with the experimental acceptance, cuts are made after the events are generated. The most frequently used cuts are on the muon momenta and the acollinearity of the muon pairs to reduce the background from two photon muon pairs ($e^+e^- \rightarrow e^+e^-\mu^+\mu^-$), hard radiative muon pairs ($e^+e^- \rightarrow \mu^+\mu^-\gamma$) and τ pairs ($e^+e^- \rightarrow \tau^+\tau^- \rightarrow \mu^+\nu_\mu\mu^-\bar{\nu}_\mu\nu_\tau\bar{\nu}_\tau$). The events from these background processes tend to have large acollinearity and low muon momenta. The cuts effectively reduce the background contamination to the muon event sample less than 1%. The radiative corrections are then estimated with the accepted events. It turns out, under the cuts of our analysis, the corrections are about 5% for the cross section and +0.012 for the asymmetry almost independent of the center of mass energy because the dependence of the corrections on the center of mass energy is logarithmic. Fig 2.4 shows the corrections to the cross section and the asymmetry as a function of the center of mass energy,

$$\Delta A(.8) = A^{MC}(.8) - A_0^{EW}(.8) \tag{2.14}$$

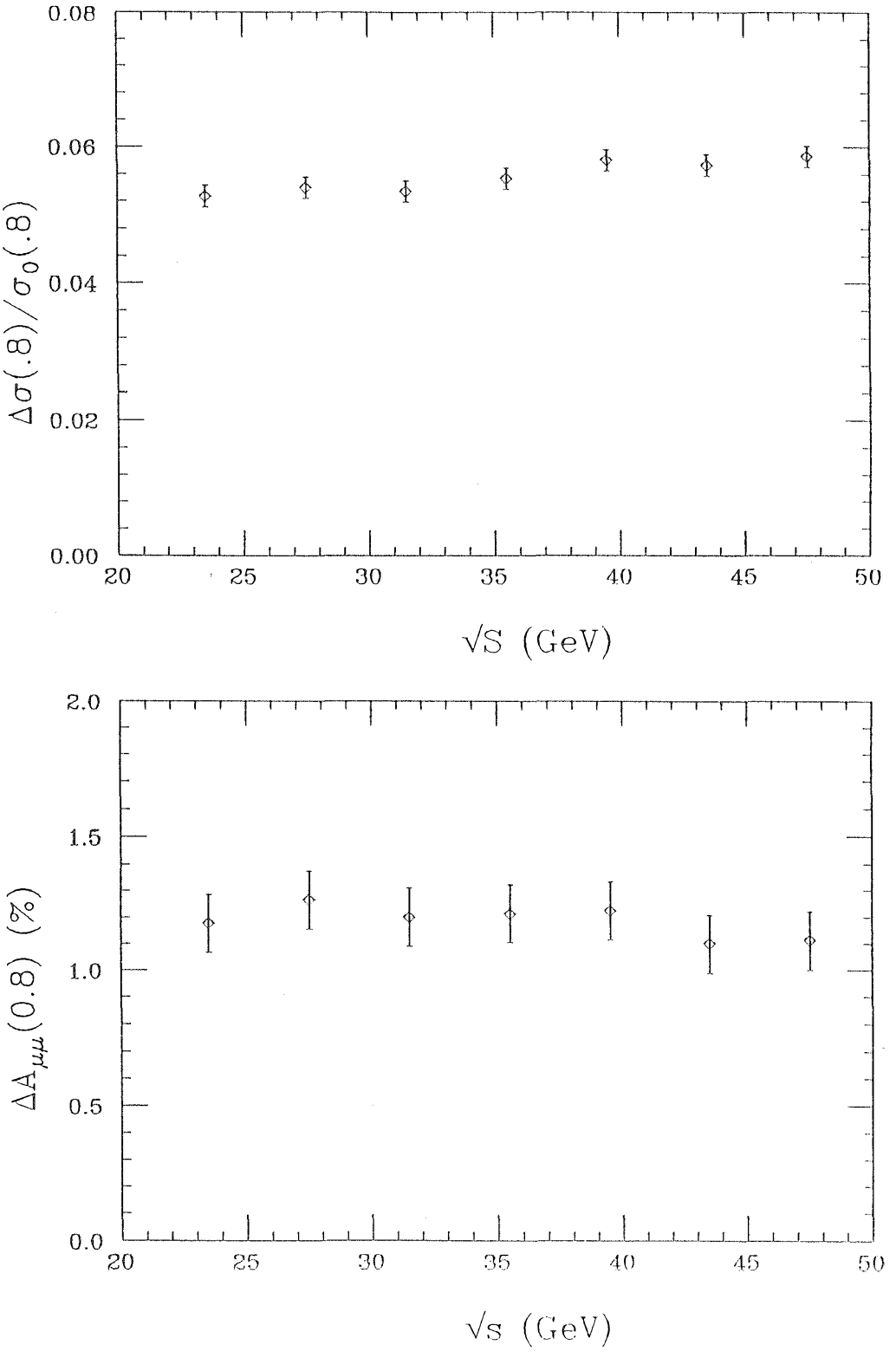

Figure 2.4 The radiative corrections to the cross section and asymmetry of $\mu^+\mu^-$ events as a function of the center of mass energy with acceptance cuts.

$$= A^{MC}(.8) - A_0^{EW}(1.) \times .879, \tag{2.15}$$

$$\frac{\Delta\sigma^{MC}(.8)}{\sigma_0(.8)} = \frac{\sigma^{MC}(.8) - \sigma_0(.8)}{\sigma_0(.8)}, \tag{2.16}$$

$$= \frac{\sigma^{MC}(.8) - \sigma_0(1.) \times .728}{\sigma_0(1.) \times .728}, \tag{2.17}$$

where the asymmetry and the cross section within the acceptance can be written as,

$$A(\theta_0) = \frac{\int_{\theta_0}^{\frac{\pi}{2}} \frac{d\sigma}{d\Omega} d\Omega - \int_{\frac{\pi}{2}}^{\pi-\theta_0} \frac{d\sigma}{d\Omega} d\Omega}{\int_{\theta_0}^{\pi-\theta_0} \frac{d\sigma}{d\Omega} d\Omega}, \tag{2.18}$$

$$\sigma(\theta_0) = \int_{\theta_0}^{\pi-\theta_0} \frac{d\sigma}{d\Omega} d\Omega. \tag{2.19}$$

The phase space cuts are,

$$Max(p_+, p_-) \geq \frac{E_b}{2}, \tag{2.20}$$

$$\xi = cos^{-1}(-\vec{p}_-, \vec{p}_+) \leq 20^o, \tag{2.21}$$

where E_b is the beam energy, ξ is the acollinearity of the muon pair. The corrections are defined as the difference between the first order calculation and the lowest order calculation within the acceptance. Fractional difference is used for cross section corrections.

The estimation of the contributions from all higher order processes are given in Appendix B based on the paper by Tsai [36].

Although the above phase space cuts are the same as the ones used in the data analysis, the detector efficiency and resolution, however, have yet to be taken into account. The more accurate corrections for the experimental data have to come from the complete detector simulation.

Although total QED radiative correction to the asymmetry is relatively small (but not negligible), cancellation between contributions from various diagrams plays an important role. The interference of two photon and one photon exchange diagrams gives a positive asymmetry while the interference of the final state and initial

state soft photon radiation gives a negative asymmetry with both magnitude as high as 20% (see Fig 2.7 in next section). Because they are in a different kinematic region, the total corrections are dependent on the kinematic cuts. With special selection cuts, these contributions may be separated and then can be studied experimentally.

2.3 $\mu^+\mu^-\gamma$ events from e^+e^- annihilation

Direct observation of $\mu^+\mu^-\gamma$ events is possible when the energy of radiative photons is large enough. Study of $\mu^+\mu^-\gamma$ events provides a test of the validity of higher order electroweak theory.

The analytic expressions of the cross section for QED $\mu^+\mu^-\gamma$ events are given in Appendix A. Similar to the effect on $\mu^+\mu^-$ events, the Z° exchange does not change the cross section by a significant amount, but does change the charge asymmetry. The photon radiated can be crudely classified as initial state radiation and final state radiation. In the limit of QED (without electroweak effects), the interference between the initial and final state radiation does not contribute to the total cross section because it is totally antisymmetric. The photon energy distribution of the initial and final state radiation is shown in Fig 2.5, where only events with photon energy greater than 3% of the center of mass energy are generated. The cross sections of both the final state and the initial state radiation falls steeply as the energy increases, which is a typical behavior of bremsstrahlung radiation. The cross section of the initial state radiation rises as the photon energy approaches the beam energy. This can be interpreted as follows: after the photon is emitted from the electron or positron, the center of mass energy of the e^+e^- pair is effectively lowered, giving rise to a larger cross section for the annihilation. The balance between the bremsstrahlung and the effective center of mass energy results in the

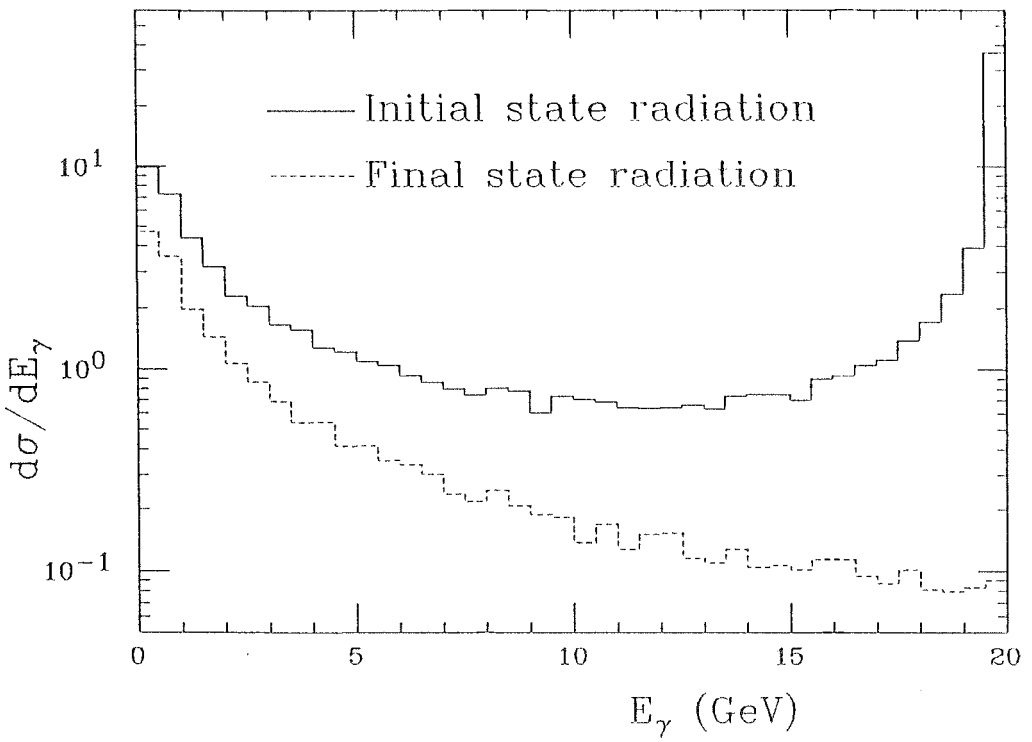

Figure 2.5 The photon energy distribution of initial and final state radiation.

photon energy distribution of the initial state radiation. Unfortunately, the events with hard photons ($k_\gamma/E_b > .75$) are always accompanied by a pair of very close muons, which can not be always resolved by our detector, hence, are not accepted as $\mu^+\mu^-\gamma$ events in our data sample.

Because of the nature of the bremsstrahlung radiation, the initial (final) state radiative photons tend to go in the direction of the beams (muons). Fig 2.6 is the photon angular distribution after applying the cuts:

$$Max(p_+, p_-) \geq \frac{E_b}{3}, \tag{2.22}$$

$$\xi \leq 160^\circ, \quad |\cos\theta_\mu| \leq 0.8 \tag{2.23}$$

$$E_\gamma \geq .03\sqrt{s} \tag{2.24}$$

Fig 2.6 also tells us that in the accepted event sample ($|\cos\theta_\gamma| \leq .9$), final state radiation dominates, with about a factor of two more than the initial state radiation.

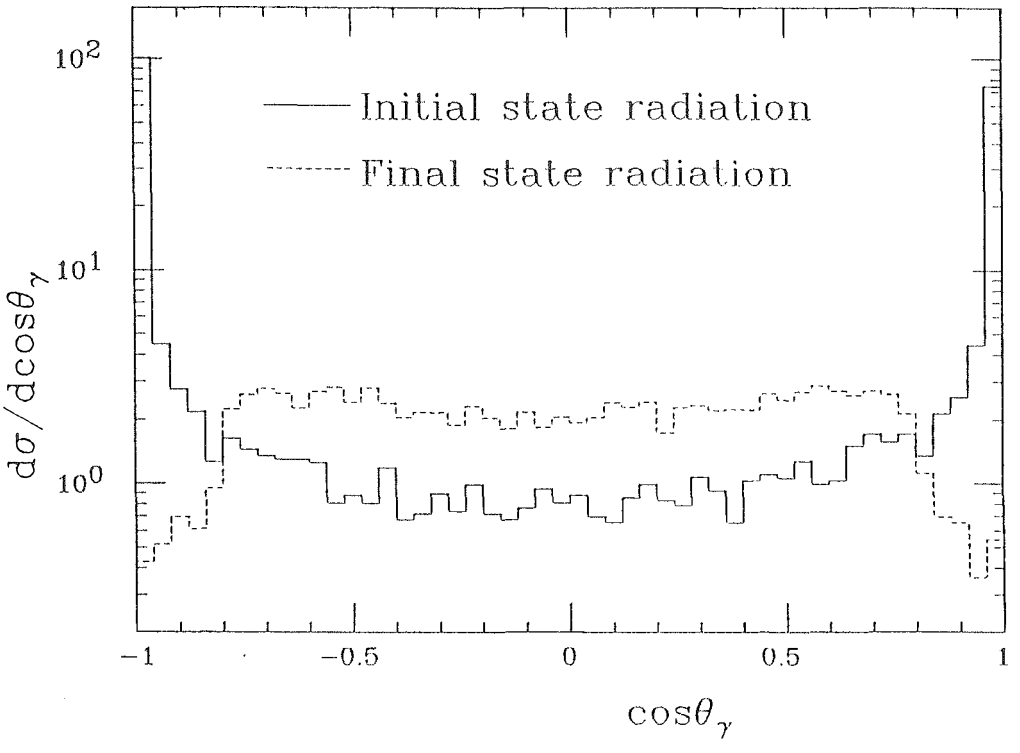

Figure 2.6 The photon angular distribution of the initial and final state radiation with the cuts explained in the text.

Since the muons in $\mu^+\mu^-\gamma$ events are not back to back, the definition of the asymmetry is somewhat modified. The positive and negative muons are considered separately. Each event gives two entries. As discussed in the previous section, the muon charge asymmetry of $\mu^+\mu^-\gamma$ events comes not only from the electroweak interference, but also from the interference between the initial and final state radiation. While the electroweak asymmetry depends mainly on the momentum transfer of the neutral intermediate boson, the asymmetry due to radiative interference strongly depends on the kinematic cuts on the muons and photon. In general, the asymmetry decreases as the photon energy gets larger. This can already be seen in the analytic expression of the cross section for soft photon radiation integrated up to photon energy k_1 where the muons are taken as back to back:

$$\frac{d\sigma}{d\Omega} = \frac{d\sigma_0}{d\Omega}(1+\beta\ln(\frac{k_1}{E})+\delta_{AR}+2\Pi), \tag{2.25}$$

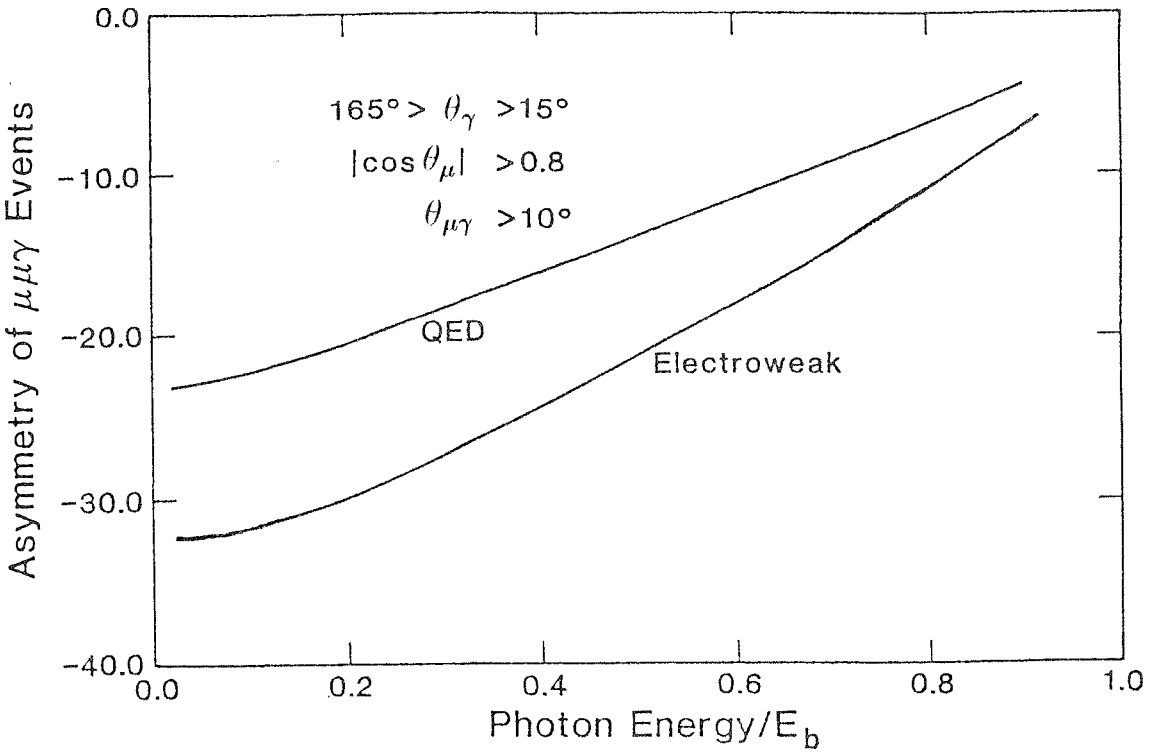

Figure 2.7 The muon charge asymmetry as a function of photon energy with the cuts explained in the text.

$$\beta = \beta_i + \beta_f + \beta_{int}, \tag{2.26}$$

$$\beta_{int} = \frac{8\alpha}{\pi} \ln(\tan\frac{\theta}{2}), \tag{2.27}$$

where δ_{AR}, II, β_i and β_f are independent of the photon energy and β_i, β_f are independent of θ (see Appendix A for details). The asymmetry contributed by the events with photon energy between k to $k + \Delta$k can be approximated as,

$$\Delta A \propto \ln(\tan\frac{\theta}{2})\frac{\Delta k}{k}, \quad \theta \leq 90°. \tag{2.28}$$

The contribution is negative, and decreases in magnitude as the photon energy gets larger.

The asymmetry will be enhanced if a kinematic region where the interference term is large is selected. For example, Fig 2.7 shows the asymmetry vs photon energy when the opening angle between the photon and the muons are required to be larger than 10 degrees in addition to the the requirements of Eq (2.22) and

Eq (2.23). In this region the peaks of the cross sections of initial and final state radiation are avoided, and the interference term is comparable in magnitude to the initial and final state radiation term.

Another purpose of studying $\mu^+\mu^-\gamma$ events is to search for the excited states of muons which might be produced in e^+e^- annihilation. Details are given in Chapter 6.

Chapter 3

The Experiment

3.1 PETRA

The e^+e^- storage ring PETRA (Positron Electron Tandem Ringbeschleuniger Anlage) [37] at DESY (Deutsches Electronen Sychrontron) in Hamburg, Federal Republic of Germany and its injection apparatus are shown in Fig 3.1. It was the highest energy electron-positron colliding beam machine in the world from 1979 to 1986. The storage ring is housed in a 2.3 kilometer tunnel with eight straight sections and eight identical curved sections, and it consists of quadrupole magnets, sextupole magnets and 5.5 meter bending magnets with a bending radius of 192 meters.

Four of the eight straight sections are long sections for RF accelerating cavities, and the other four are short sections for experiments.

Electrons are injected at 50 MeV from Linac I into DESY, accelerated to 7 GeV, and injected into the PETRA ring to form two bunches of 2-6 mA each. Positrons are accumulated in PIA (Positron Intensity Accumulator), after acceleration in LINAC II to 400 MeV. Twenty successive LINAC bunches are injected into PIA, compressed in phase space, and further accelerated in DESY and injected into PETRA at 7 GeV. The two pairs of counter-circulating bunches are then further accelerated and focused to collide inside the four experiments.

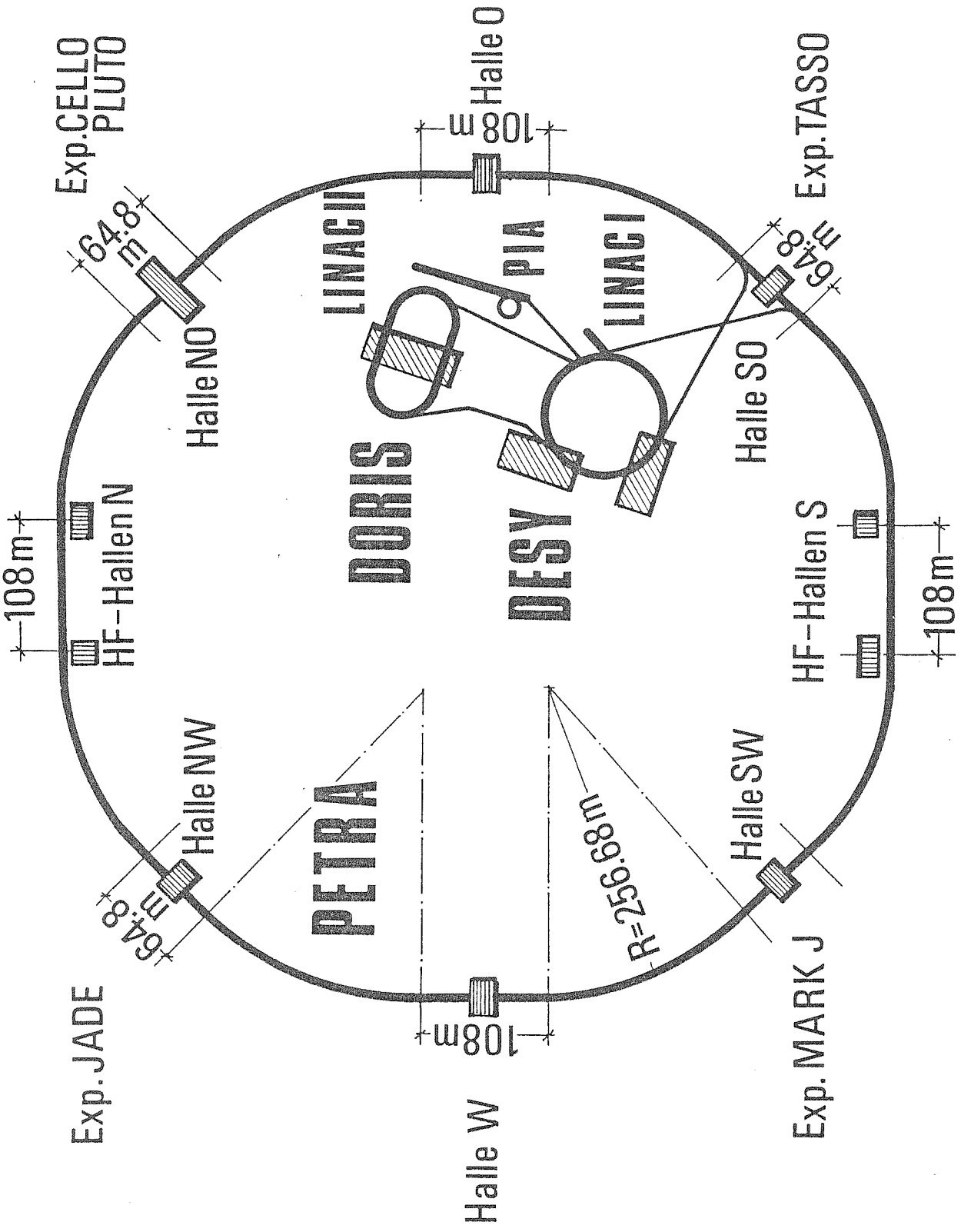

Figure 3.1 PETRA.

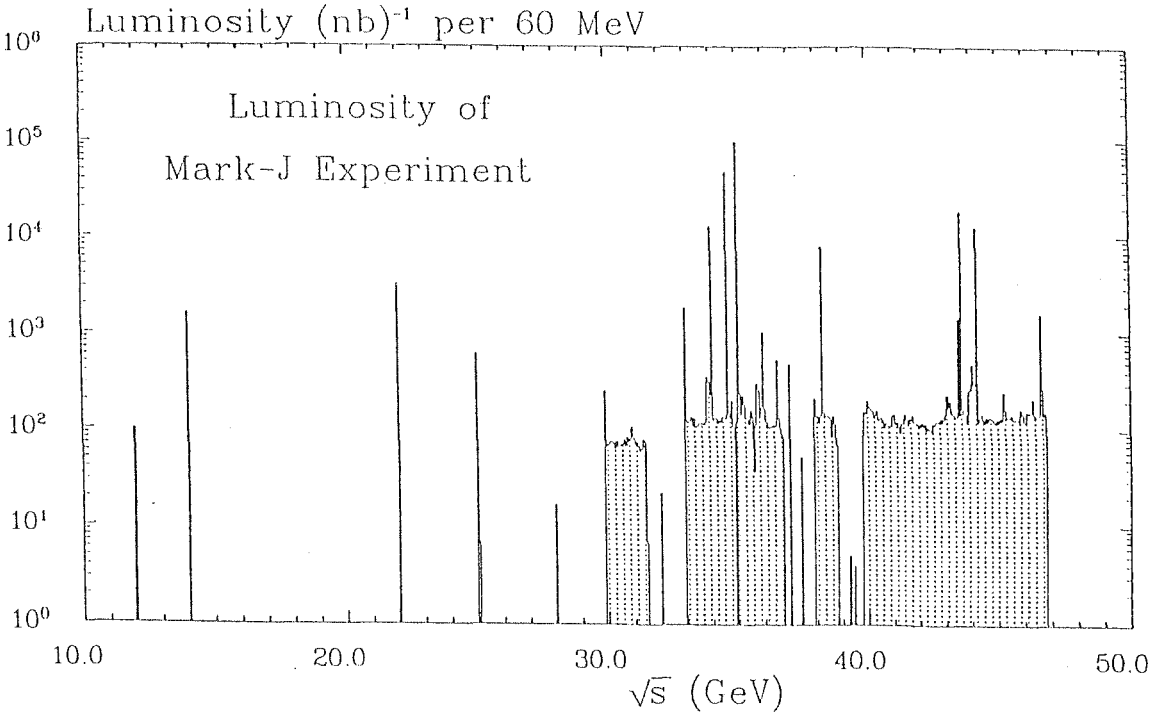

Figure 3.2 The luminosity collected by the Mark J detector.

Since the first physics runs for experiments in November 1978, the ring elements have been modified to provide higher luminosities and higher beam energies. One of the most important improvement is the mini-beta scheme installed in March 1981, which increased the luminosity by a factor of 2.5 to 3. The peak instantaneous luminosity obtained with the MARK J detector was $1.6 \cdot 10^{31}/\mathrm{cm}^2/\mathrm{sec}$, with up to 650 nb^{-1} collected in one day. The integrated luminosity collected with the MARK J detector over the resulting large range of center of mass energy, $\sqrt{s}$, from 12 GeV up to the highest energy of 46.78 GeV, is shown in Fig 3.2. As is evident in the plot, particularly large data samples were collected at energies around 35 and 44 GeV.

3.2 The MARK J detector

The MARK J detector [38,39], located in SW Hall of the PETRA ring, shown in Fig 3.3 and Fig 3.4, was designed to distinguish charged and neutral hadrons as

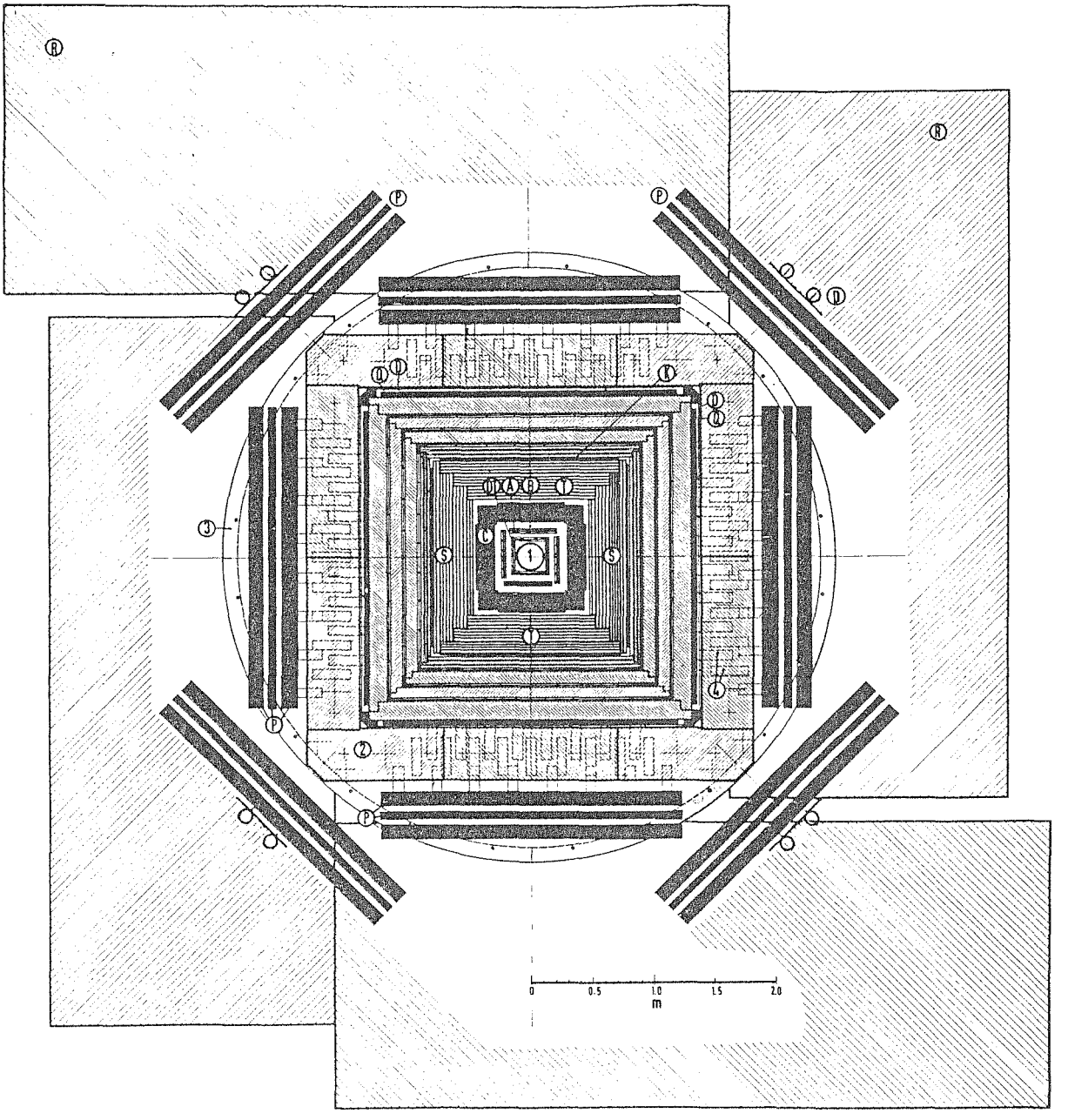

(A)(B)(C) SHOWER COUNTERS
(D) TRIGGER COUNTERS
(M) DRIFT TUBES
(Q) DRIFT CHAMBERS, MEDIAN
(P)(R) DRIFT CHAMBERS, OUTER
(S)(T) DRIFT CHAMBERS, INNER

① BEAM PIPE
② MAGNET IRON
③ Al-RING
④ MULTIPLIERS

PARTICIPANTS:
RWTH - Aachen
DESY - Hamburg
MIT - Cambridge
NIKHEF - Amsterdam
HEPI - Peking
JEN - Madrid
CALTECH - Pasadena

WEIGHT (total) : ~ 400 t
MAGNETIC FIELD: 1.8 T

Figure 3.3 The Mark J detector, end view.

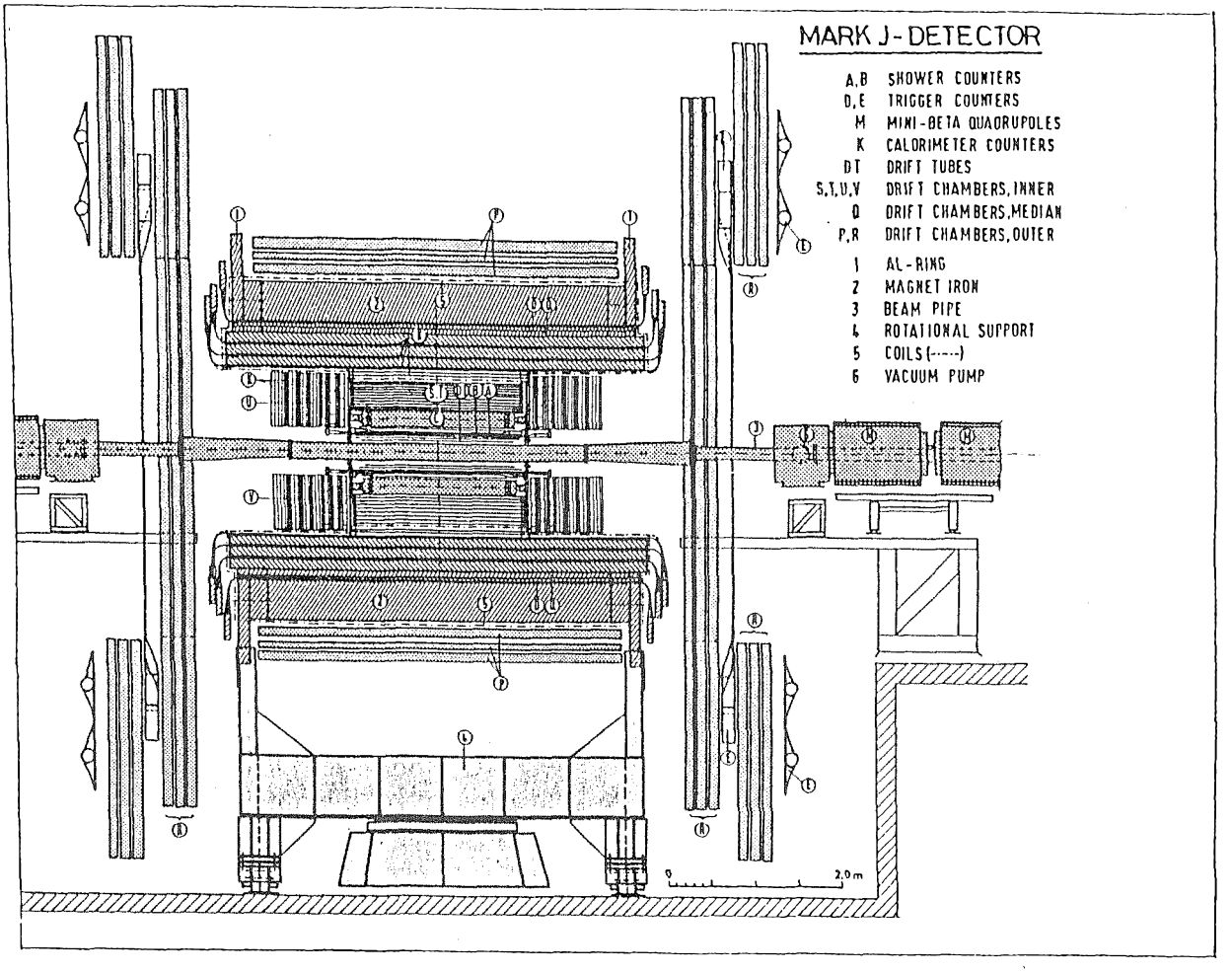

Figure 3.4 The Mark J detector, side view.

well as electrons, photons and muons, and to measure their direction and energy. It consists of two main parts; a calorimeter and a muon analyzer. The first part, the electromagnetic and the hadronic shower calorimeter, covers from 12° to 168° in polar angle θ and the whole azimuthal angle ϕ. The second part consists of five magnetized iron toroids which also serve as an absorber, supplemented by large planar drift chambers, both inside and outside the magnets, to analyze the muons.

Particles leaving the e^+e^- interaction region traverse the detector layers shown schematically in Fig 3.5. Outside of the beampipe is the vertex detector labeled

DT (drift tubes) in Fig 3.3 and Fig 3.5. The next layer is the electromagnetic calorimeter (A, B, C). Surrounding this calorimeter are the inner drift chambers of the muon spectrometer (S,T). Proceeding radially outward the magnet toroids of the spectrometer form the absorber for the hadronic or outer calorimeter (K). The outermost part of the detector completes the muon spectrometer with trigger counters (D), more magnetized iron, and drift chambers (P,R).

3.3 Calorimetry

Leaving the vertex detector, the particles then pass through the electromagnetic calorimeter made of 18 radiation lengths (measured normal to the surface of the counters) of lead scintillator sandwich shower counters, which are subdivided into three azimuthally segmented layers of shower counters (A, B, C in Fig 3.5). Each counter is made up of 0.5 cm thick pieces of scintillator alternated with 0.5 cm thick lead plates. At normal incidence this yields 3, 3 and 12 radiation lengths or a total of 1 absorption length. The 20 A counters are arrayed parallel to the beamline outside of an iron box which surrounds the vertex detector. They cover the polar angle θ from 12° to 168° with no azimuthal holes. The 24 B and 16 C counters are arranged similarly to the A counters, but are offset in ϕ and shorter, covering θ from 16° to 164°. Each of these sixty counters is instrumented with one phototube at each end. The time and magnitude of both phototube pulses are digitized with TDCs (Time to Digital Converter) and ADCs (Analog to Digital Converter) and are recorded. The position of the track along the direction of the counters can thus be determined by the use of the ADC ratio or TDC differences measured by phototubes at the ends of the counter:

$$Z_{TDC} = \frac{v}{2}(TDC_1 - TDC_2), \tag{3.1}$$

$$Z_{ADC} = \frac{\lambda}{2}\ln(\frac{g_2 ADC_2}{g_1 ADC_1}), \tag{3.2}$$

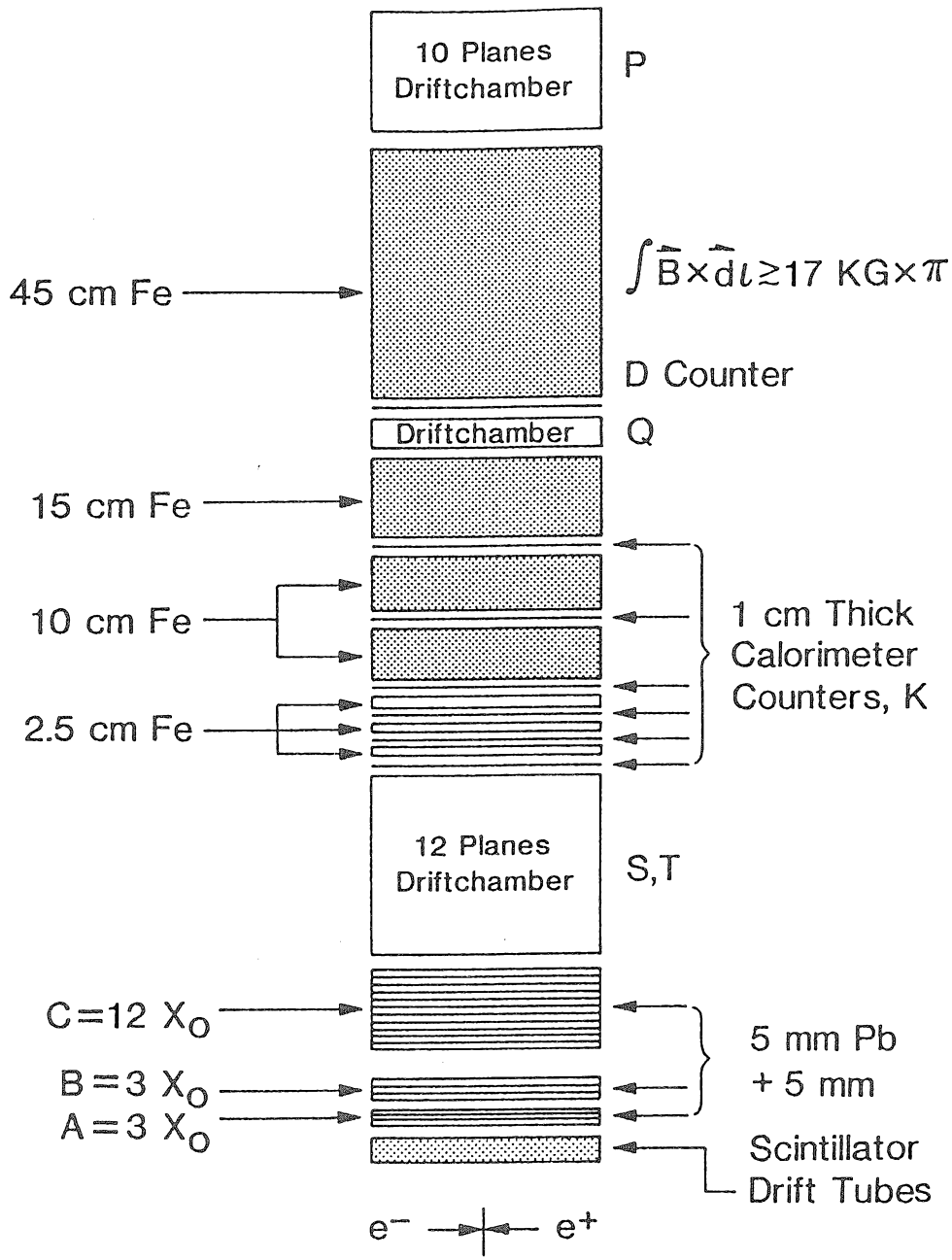

Figure 3.5 Layer structure of the Mark J detector.

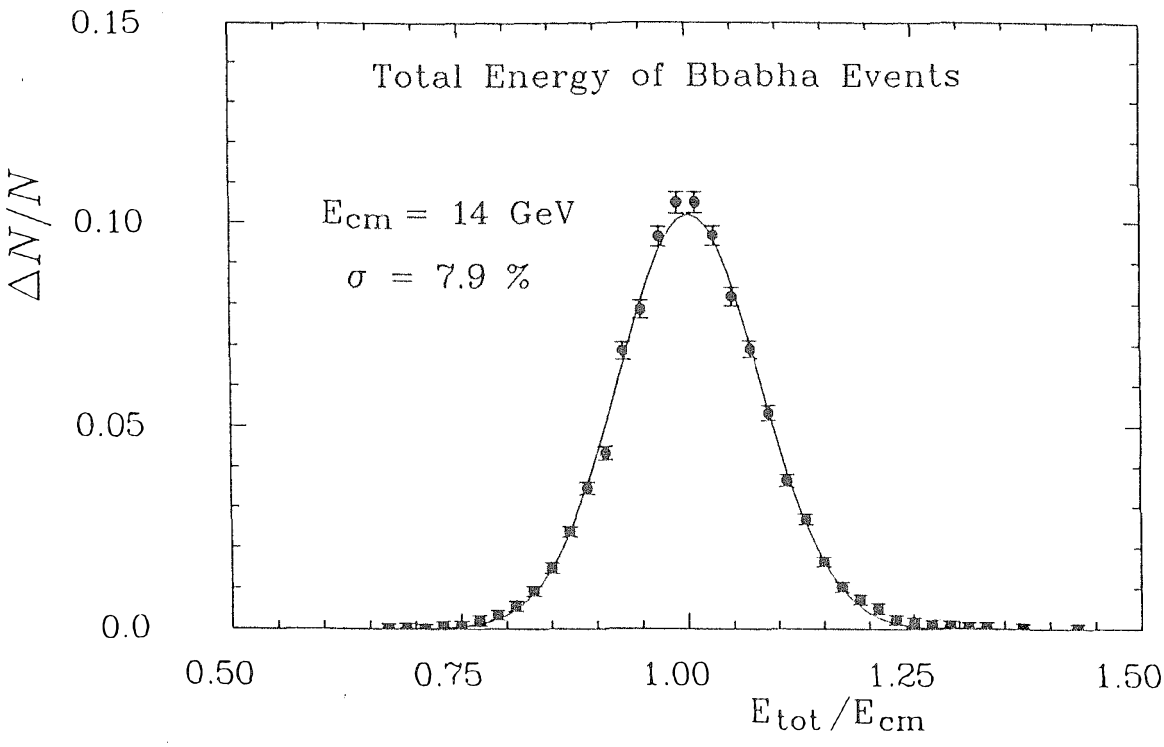

Figure 3.6 The energy resolution of the EM calorimeter.

where,

λ is the light attenuation length of the counter,

v is the velocity of the light in the scintillators,

g_i is the conversion factor from ADC to energy deposit in the counters.

A weighted average gives a z-position resolution of 2.5cm. Comparing to the the positions extrapolated from track fitting in the vertex detector this method yields a resolution for single hits of $\Delta\theta = 5^\circ$ per counter. The azimuthal segmentation combined with shower sharing between counters yields a resolution of $\Delta\phi = 7^\circ$.

The energy deposited in each counter is determined from the two pulse heights corrected for attenuation:

$$E = G(g_1 ADC_1 exp(-\frac{z + l/2}{\lambda}) + g_2 ADC_2 exp(-\frac{l/2 - z}{\lambda})), \qquad (3.3)$$

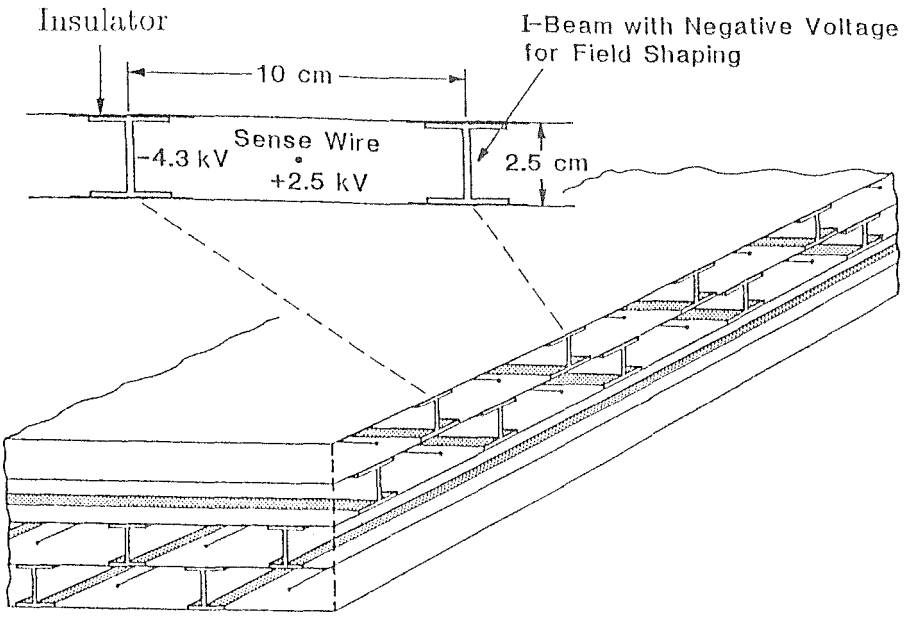

Figure 3.7 Mechanical assembly of large drift chambers for muon detection.

where l is the length of the counter and G is the ratio of the total energy deposited in a counter to the energy observed in the scintillator. The leakage of electromagnetic showers from electrons and photons into the outer calorimeter is less than 4%.

On the average, a hadronic event deposits 75% of its energy in the A, B, C counters. The remaining 25% of the energy is absorbed in the outer calorimeter. 192 scintillation counters are arranged in four layers interleaved with 2.5 to 10 cm of iron for a total of 2 absorption lengths at normal incidence. In this calorimeter the ϕ resolution is better than that in the inner calorimeter because of the finer segmentation. The longitudinal resolution is worse because only one end of each counter is viewed by a phototube.

3.4 Muon spectrometer

The tracking devices of the charged particles consist of two parts in the detector, the vertex detector and the muon chambers.

The vertex detector measures the tracks of charged particles and the production vertex along the beamline. It consists of 2616 cylindrical drift tubes arrayed perpendicular to the beams in four rectangular layers. Each tube is 1 cm in diameter and 30 cm long. The array actively covers the polar angle from $\theta = 10^{\circ}$ to 170° and the entire azimuth except 7° in each corner. The resolution per tube is 270μm. Tracks are fitted to hits in each layer. The best overall fit for an event is determined by constraining the tracks to a common vertex along the beam direction, z, and minimizing the χ^2 per track. The number of tracks pointing to this common vertex yields a measure of the charged multiplicity. The r.m.s. width of the best fit vertices for hadronic events is just that expected from the beam bunch length, $\triangle z = 1.3$ cm.

A muon is identified by its ability to penetrate the iron. The total thickness of the iron is 87cm at normal incidence. Together with the electromagnetic calorimeter, there are 5.4 hadronic interaction lengths to filter out hadrons. The magnetic field in the iron has an integrated field strength of 17 kG-meter. At normal incidence, the low momentum cutoff is about 1.3 GeV/c. The initial muon direction is measured in the inner drift chambers labeled as S,T,U and V in Fig 3.5. The track in the bending plane is measured by the two plane Q chambers after the muon has traversed 42 cm of iron, then the P and R chambers measure the bending angle and position of muon exiting the iron.

All drift chambers (S,T,U,V,P,R) consist of 10 cm cells formed by two field-shaping I-beams (which provide the structral strength) glued with insulators between two aluminum ground plates(see Fig 3.7). A coordinate is measured by a double layer of such cells, with the second layer displaced by half a cell width from

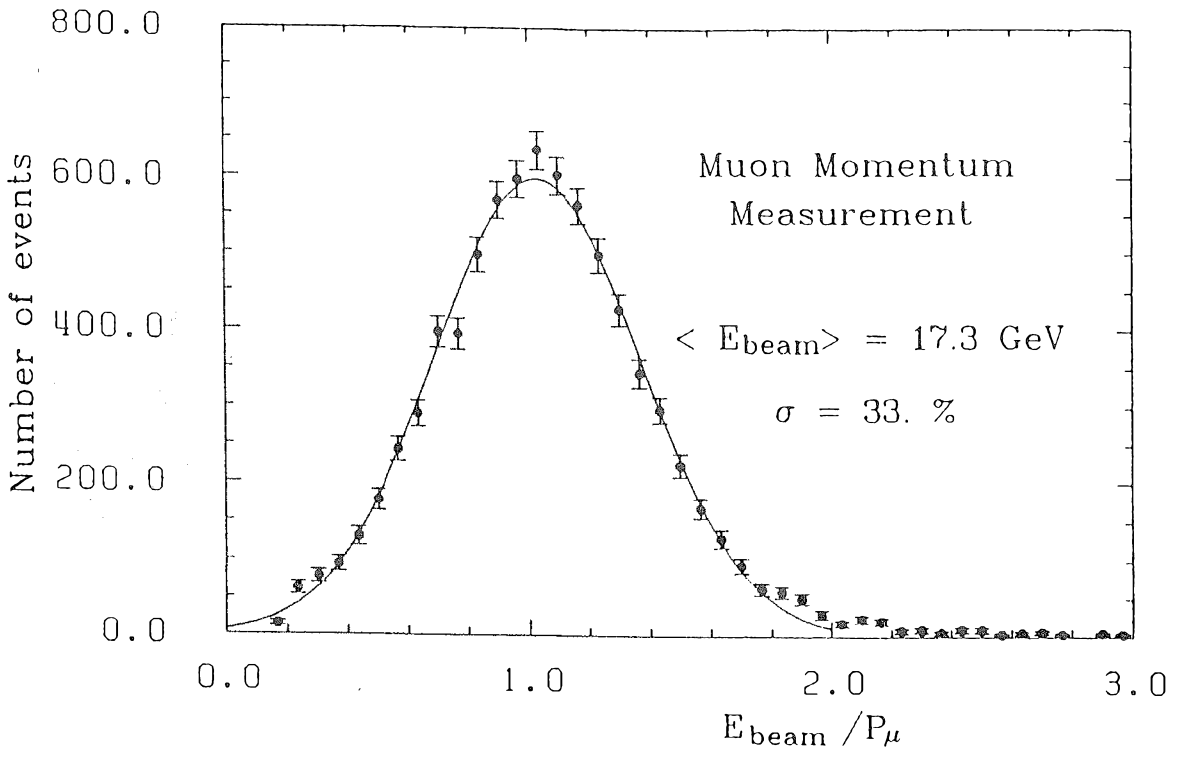

Figure 3.8 The muon spectrometer resolution.

the first to resolve the left-right ambiguity. Individual cells have been tested to give a resolution of 0.4mm for perpendicular tracks in our system of 5000 wires with individually calibrated TDC's. This is much smaller then the spread resulting from the multiple scattering in the iron. The average angular deviation due to multiple scattering is proportional to 1/p to the first order, where p is the muon momentum, and is given by,

$$\begin{aligned} \Delta\theta_{m.s.} &= \frac{20 Z_{inc}}{\sqrt{2} p\beta}\sqrt{\frac{L}{L_0}}\left[1+\frac{1}{9}\log_{10}\left(\frac{L}{L_0}\right)\right] \\ &\simeq \frac{0.12}{p[GeV]}, \end{aligned} \tag{3.4}$$

where L is the muon path length in the magnetic field, and L_0 is the radiation length of the traversed material. For iron, L_0 = 1.76 cm.

The bending angle due to the magnetic field is also proportional to 1/p,

$$\Delta\theta_{magnet} = \frac{0.3BL}{p} \simeq \frac{0.51}{p[GeV]}. \tag{3.5}$$

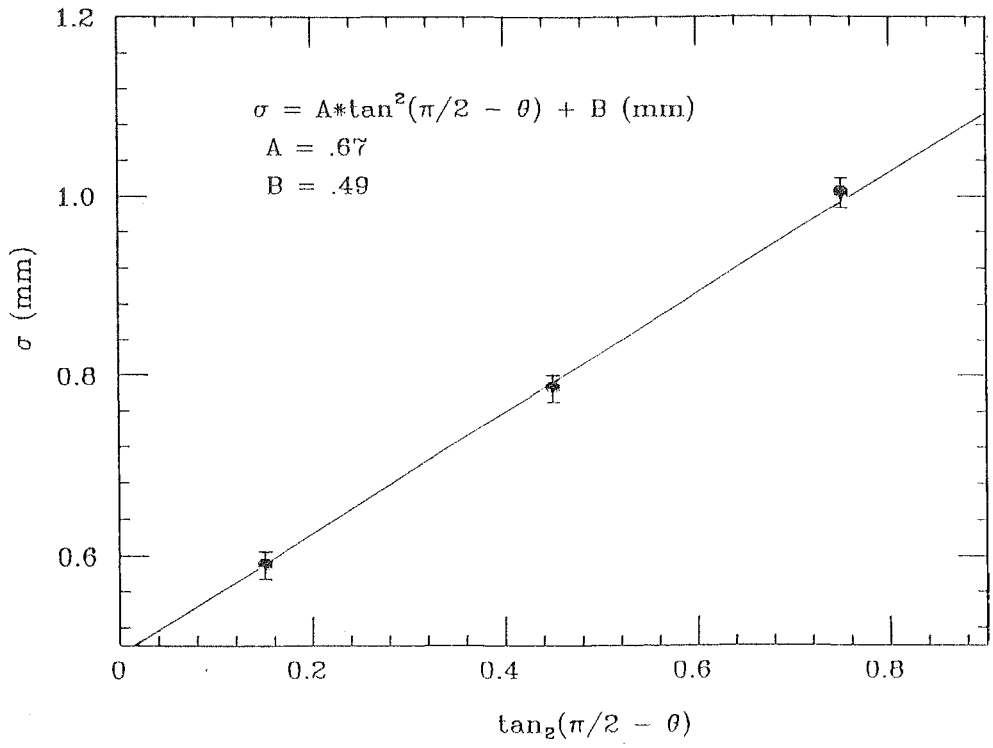

Figure 3.9 The muon chamber resolution as a function of θ angle with respect to the chamber plane.

Thus, in the absence of other sources of error, $(\sigma_{(1/p)}/(1/p))$ would be $\simeq$ 24 % and independent of momentum.

The muon chamber resolution as a function of θ angle is shown in Fig 3.9. It can be parametrized as,

$$\sigma = .49 + .67 \tan^2(\frac{\pi}{2} - \theta) \quad (mm). \tag{3.6}$$

This dependence of the resolution is properly simulated in the Monte Carlo detector simulation.

The total angular uncertainty is a quadratic sum of contributions multiple scattering and angular resolution of the ST and P chambers:

$$\Delta\theta_{total} = \sqrt{\Delta\theta^2_{m.s.} + \Delta\theta^2_{st} + \Delta\theta^2_{p}}, \tag{3.7}$$

where $\Delta\theta_{st}$ and $\Delta\theta_p$ correspond to the angular resolution of the ST and P chambers.

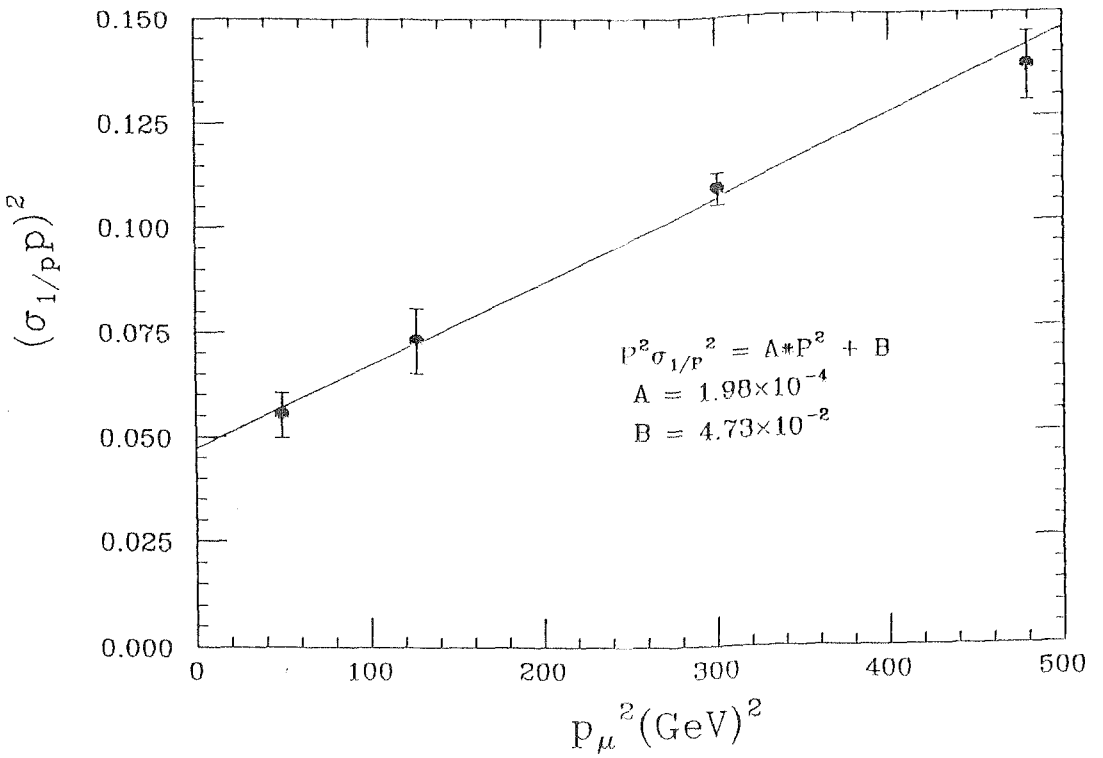

Figure 3.10 The muon momentum resolution as a function of the momentum in the MARK J detector.

The resolution of the inverse momentum, $1/p$, can be parametrized as,

$$\frac{\sigma_{1/p}}{1/p} = \frac{\Delta\theta_{total}}{\Delta\theta_{magnet}}, \tag{3.8}$$

$$\left(\frac{\sigma_{1/p}}{1/p}\right)^2 = A * p^2 + B, \tag{3.9}$$

where A and B are constants.

An estimated total fractional inverse momentum error is 30 % at p $\sim$ 17 GeV. Fig 3.8 shows the measured distribution of E_{beam}/p_μ for p_μ = 17.5 GeV/c. The resolution obtained with a gaussian fit, $\sigma = 33\%$, agrees with the estimation above. The deviation may have come from the background hits which would deteriorate the momentum resolution. To reduce the radiative muon pairs in the sample, an additional cut on the acollinearity, $\xi = cos^{-1}(-\vec{p}_-, \vec{p}_+) \leq 4^\circ$, is applied. A study of the Monte Carlo events shows that 95% of the muons in the sample have the actual

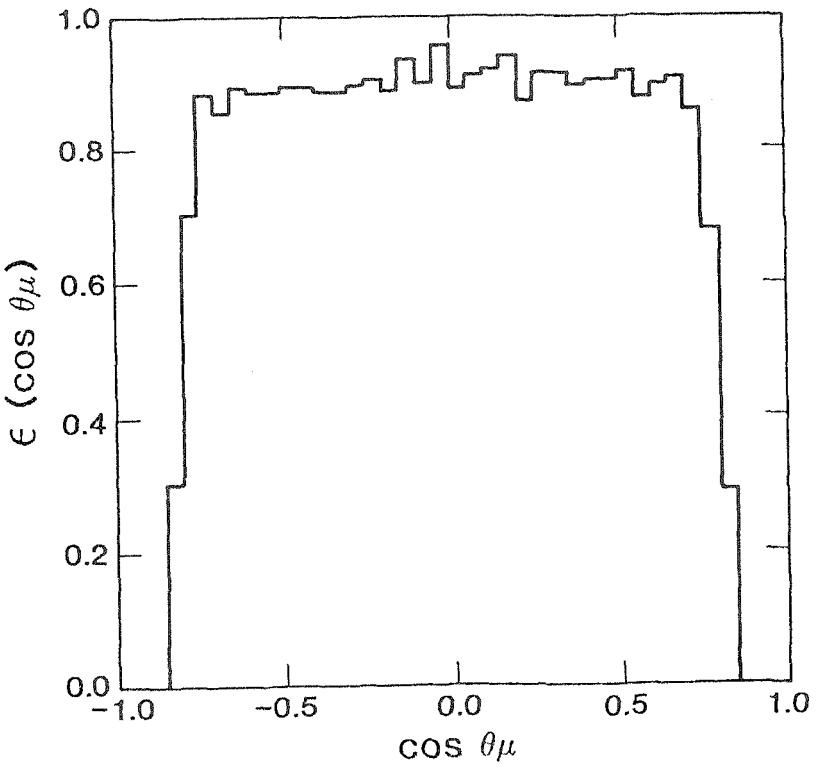

Figure 3.11 The muon acceptance (simulated).

muon momenta greater than 94% of the beam energy. The radiative effect in this resolution estimation is then negligible. Fig 3.10 shows the square of the measured inverse momentum resolution as a function of the square of the momentum. A straight line fits the data well.

The acceptance of muons in the detector is shown in Fig 3.11. It is flat in the region where $|\cos\theta| \leq 0.8$.

32 trigger counters (D) are situated 1.3 meters away from the interaction region, and another 8 (DP) are situated outside the corner P chambers to measure the time of flight of charged particles. They therefore completely cover 2π in the azimuthal angle. The good timing resolution of the counters is used by the on-line trigger and is also used to reject cosmic ray muons in off-line analyses. Fig 3.12 shows the time difference distribution of both muon pairs and cosmic ray muons. The resolution of individual counters is about .6 ns.

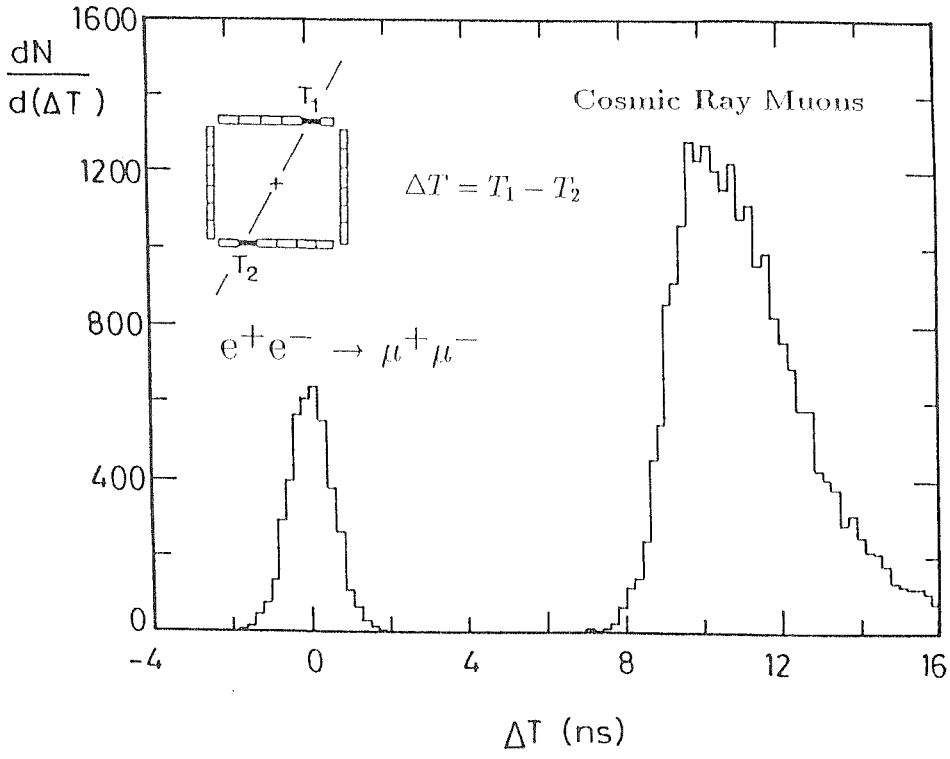

Figure 3.12 The time difference distribution of muon trigger counters for muon pairs and cosmic ray muons.

3.5 Calibration

The components of the detector were calibrated by the test beams before they were assembled together. After the installation of the detector, many components were subject to changes due to radiation damages of the scintillators, variations of the photomultiplier gains and gas composition, drifts of the electronics and so on. Constant calibration enabled one to monitor the changes of the detector parameters and to keep the high sensitivity and resolution of the detector.

In the MARK J experiment, the NIM and CAMAC electronics was checked every few months. The relative timing of the counters, which determines the fast trigger coincidence, was calibrated during shut-downs by using cosmic ray events with a special counter setup. The pedestals of the counter ADC's were checked online and recorded on tapes.

The cosmic ray events were recorded during and between data taking periods. The gain factors g_i's of the A,B,C counters are calibrated by cosmic ray muons passing through the counters. The position and the energy of a hit were determined from the orientation of the track measured by other components of the detector, and from the fact that high energy muons are minimum ionizing particles with a nearly constant dE/dx.

The attenuation length and the light propagation speed in the A, B, C counters have initially been determined from test beam data. The drift tube packages in front of the A, B, C counters enable us to calculate the values for these parameters for each individual counter and check them regularly. The large angle back-to-back Bhabha events with clean drift tube tracks are selected. The electron tracks are fitted in the drift tubes, are extrapolated to the counters, and are then compared to the positions of the hits determined from the counter ADC's and TDC's. The attenuation lengths and the TDC time zeros are then calibrated. Constant monitoring of the parameters results in the good resolution for an electromagnetic shower. $\triangle E/E = 6\%$ at $E = 22$ GeV (see Fig 3.6) and Z-position resolution of approximately $2 \sim 3$ cm for A and B counters, and approximately ~ 5 cm for C counters.

To calibrate the TDC's of the drift chambers and tubes, a sequence of signals simulating the pulses from the wires and the trigger are generated and fed to the system. This is repeated with a series of different time delays. The TDC channel to time conversion, as well as the offset, is thus obtained. This calibration is done every eight hours or so.

3.6 Data taking procedure

There are two main CAMAC branches for the Mark J detector to read in experimental data. Branch A includes scalars which monitor 300 single rates from counters, 100 coincidence rates and various other counts of the experiment. The

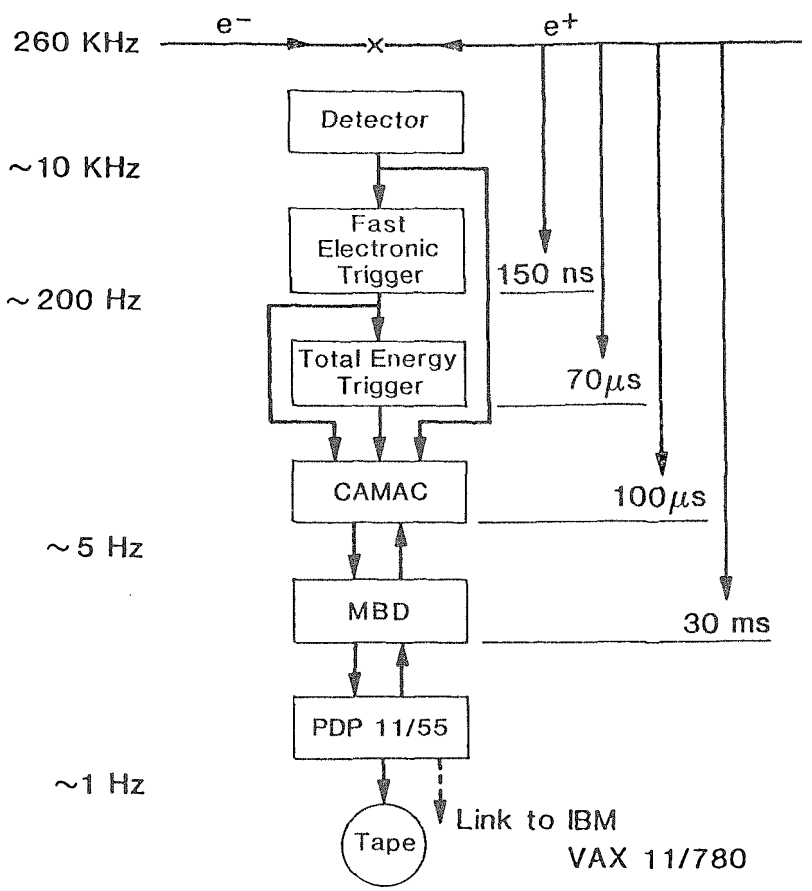

Figure 3.13 The flow chart of Mark J data taking procedure.

main experiment branch, B, is driven by the trigger. The MARK J data taking system including the timing of each part is shown in Fig 3.13 [40].

The data taking procedure is arranged in three stages.

The first stage is a fast, loose trigger generated from the hit information of the A, B, C, D, K and E counters. By combining this information in different ways as described below, various trigger signals are produced which correspond roughly to different final states from the e^+e^- collisions. All of the analog and time to digital conversions are initiated by this first stage trigger.

The second stage is a total energy trigger. When the first stage trigger initiates the ADC's and TDC's, it starts the total energy trigger circuit at the same time. Analog sum signals from A, B and C counters are fed into a linear fan-in after proper attenuation adjusted so as to allow different weights for different counter arrays. The output is then sent to an integrator to find the total charge in the analog sum. The output from the integrator, which is proportional to the total energy detected, goes to discriminators. The setting of the discriminators depends on the beam energy and is different for various trigger types. If the energy trigger condition corresponding to a given trigger type is satisfied, the CAMAC modules continue to convert all of the signals from the detector into digital signals. Otherwise, a clear signal is sent to the CAMAC crates. For muon events the total energy trigger is not applied.

The third stage is an on-line selection which is performed by the Microprogrammable Branch Driver (MBD). The MBD is the interface between the on-line computer and CAMAC. As an on-line filter, the MBD first reads an input register to see which trigger has occurred. Then it does different tests depending on the type of the trigger. If the trigger is a hadron or Bhabha trigger, the energies deposited in the A, B and C counters are added and checked. If the sum is less than 1/12 of the total center of mass energy of the beams, the event is rejected. For events passing the first test, the K counter energy is added to the total energy, which is then required to be at least 1/6 of the center of mass energy. After this cut, drift chamber and drift tube data are read in. If the muon trigger bits are on, three pairs of adjacent wires of inner drift chambers are required. The idea is that a real track in chambers involves at least two staggered, and hence adjacent drift cells, one in each layer of a double plane. This effectively rejects accidental triggers due to signals in muon trigger counters. For an accepted event, the MBD reads in all of the information of the chambers and counters from the corresponding CAMAC modules and decides which data words are useful, *i.e.*, whether their values are greater than the pedestal

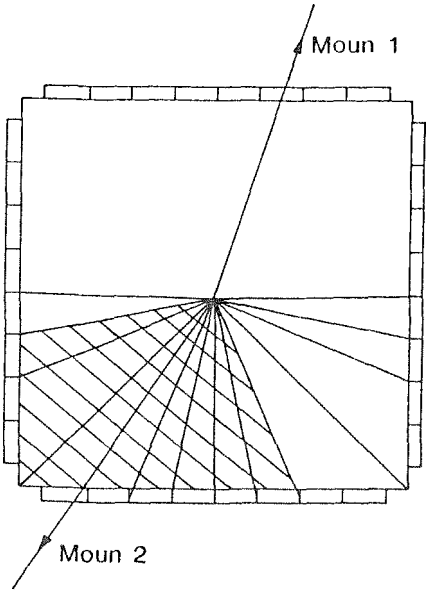

Figure 3.14 The geometry corresponding to the DX logic.

suppression values in the case of the ADC's, or less than the overflow values in the case of the TDC's. Only valid data are transferred to the on-line computer and then written onto tapes. For the triggers that are accepted, the deadtime is about 30ms, for a rejected trigger it takes typically 3ms.

The trigger patterns of the MARK J detector are Bhabha, hadron, large angle Bhabha, single electromagnetic shower, muon pair, single muon, cosmic ray muon and beam gate.

The cosmic ray trigger is a special trigger designed to accept cosmic ray muons between beam crossings. These cosmic ray muons are used for counter calibration as discussed previously.

A 'beam gate' event is taken every 100 accepted events, in which a trigger is generated when the bunches cross without further requirement. This allows us to monitor the background conditions.

D counters are the main detector components to define a muon track at the trigger level. They are well shielded against the background from the circulating beams. The main potential background, however, comes from cosmic rays. Because the D counters are long (4.5m), meantimers, which are designed to equalize the light propagation time, are used to provide an output at a fixed time independent of the location of the traversing particle.

The single muon trigger is designed as the coincidence of D, DA2, DB2 and DC2, while the dimuon trigger as that of D, DX, DA2 and DB2, where,

D: at least one D counter has been hit during the bunch crossing (the meantimer output (width=20ns) in coincidence with the beam gate (3ns)). The gate is effectively open for 23 ns, or equivalently, .6% of the time as the bunch crossing rate is 260kHz. This reduces the cosmic ray background significantly.

DA2: at least 2 A counters have been hit.

DB2: at least 2 B counter phototubes have fired.

DC2: at least 2 C counter phototubes have fired.

DX: a special logic module which has 24 inputs, 8 of which are for the 16 corner counters ORed two by two, and other 16 for the remaining 16 counter elements. When a signal arrives at any of the inputs, the circuit logic requires there must be at least one signal within the opposite 7 sections, as shown in Fig 3.14 to generate a signal. This then only accepts coplanar dimuon within 50° on average.

The physics processes associated with the single muon trigger are τ lepton production with one of the τ's decaying into μ and the other into e or hadrons, inclusive muon events in which the muon is from the decay of a heavy quark, hard radiative

muon pairs, etc.. The common characteristics of the processes is a muon accompanied by some energies in the calorimeters.

The double muon trigger selects events in which two muons come out of the interaction region back to back and both are in coincidence with the beam crossing. This trigger has practically no beam associated background. The majority of the events accepted are cosmic ray muons coming to the detector during the beam crossing. The trigger rate is constantly 0.35 Hz all the time. These cosmic ray muons can be easily rejected in the offline analysis.

The Bhabha events deposit most of their energies in the A, B and C counters. The Bhabha event trigger comes from the fast analog sum of the pulses of the A, B and C counters with linear fan-in circuits. For small angle Bhabha events, the showers are fully developed in the inner two layers of the calorimeter. The criterion for such an event is that any two of the quadrants have energies deposited in A and B counters of at least 220 MeV. Acoplanar events near the corners are also accepted by this trigger design since the coincidence of the opposite quadrants are not required. This is necessary because the radiative Bhabha events are included in the analysis. For large angle Bhabha events, it is possible that the showers are not fully developed in the A and B counters. The above criterion may cause loss of these events. As a complement, a C counter energy trigger is designed to accept such events. The sum of all the C counter pulses is fed to a discriminator whose threshold is set equivalently at 1.2 GeV. Since C counters are well shielded from the beam background, the trigger rate is very low.

The hadron trigger is generated based on three criteria, the number of counter elements that have been hit, total energies deposited in the A, B and C counters, and energy balance. At least three A and B array elements are required to have been hit. The threshold for the sum of the energies in A, B or C counters of each quadrant is set to be higher than the energy left by one minimum ionizing particle.

It is required that there are at least two pairs of coincidences between opposite quadrants of A, B or C counter arrays above this threshold to assure that the event is balanced.

At the second trigger stage, the total energy threshold for hadron and Bhabha events is 12% of the center of mass energy. This effectively reduces the trigger rate down to 5 Hz.

To ensure high trigger efficiency requires careful online monitoring and frequent feedback from offline analysis. By checking the single and coincidence rates from the counters and counts from the chamber wires, any inefficient or dead components could be detected during the data taking. Offline analyses can give the threshold energy, angular distributions of the events, meantime distributions, etc.. These help to keep the detector running properly. Since the triggers overlap for certain kinds of events, such as Bhabha and hadron triggers, double and single muon triggers, the trigger efficiencies are checked by events accepted independently by various triggers.

In this analysis, data taken in periods with inefficient counters and chambers are excluded, which are about 6% of the total luminosity. The trigger efficiencies for $\mu^+\mu^-$ and $\mu^+\mu^-\gamma$ events are determined to be greater than 99.5%.

3.7 Luminosity

Luminosity is one of the fundamental quantities that has to be measured as accurately as possible. Any absolute measurement of the cross section of a process is affected by the accuracy of the luminosity measurement. We use Bhabha scattering to measure the luminosity because it has the highest statistics among all the data samples and the rate is dominated by low Q^2 events (scattering at small angle), where QED is well understood. The Monte Carlo simulation program from Berends and Kleiss [41] is used to generate the events and evaluate the cross section to the order α^3.

Because of the t-channel photon exchange, the Bhabha event rate increases rapidly towards the small polar angle θ. It is crucial to understand the detector behavior at small angles for calculating the acceptance of Bhabha events. In fact, this limits the reduction of the systematic error of the luminosity measurement. In the Mark J detector, the small polar angle region in the central detector is covered by A counters. The uncertainty in simulating the electromagnetic shower at the ends of the A counters would bring in a systematic shift of the expected rate. In order to check the luminosity independent of central detector, there are 48 lead-glass counters installed in both forward and backward regions close to the beampipe as luminosity monitor over long running periods. By comparing the luminosity measured by the central detector and that measured by the luminosity monitor, we conclude that the systematic error is about 3%. It is reasonable to assume that this systematic shift is independent of the center of mass energy and has been the same throughout the running of the experiment.

Chapter 4

Results on muon pair production

4.1 Event selection

The muon pair events are selected in MARK J as two minimum ionizing tracks from the interaction point penetrating the magnetized iron and reaching the outer drift chambers. We only retain events with $|\cos\theta| \leq 0.8$ because the acceptance in this angular region is flat and about 90% (Fig 3.11).

In order to separate the events from cosmic ray muons we use the following criteria:

1. both particles emerge from within a cylindrical region of 20 cm length and 5 cm radius centered at the beam crossing point;

2. the time coincidence of the muon trigger counters with the beam gate is better than 5 nsec;

3. the time difference between the muon trigger counter hit by each track must be smaller than 4 ns.

Two other physics processes also could give $\mu^+\mu^-$ final states in the detector. They are :

1. Two photon process, $e^+e^- \rightarrow e^+e^-\ \mu^+\mu^-$, with two electrons escaping from the detector along the beamline;

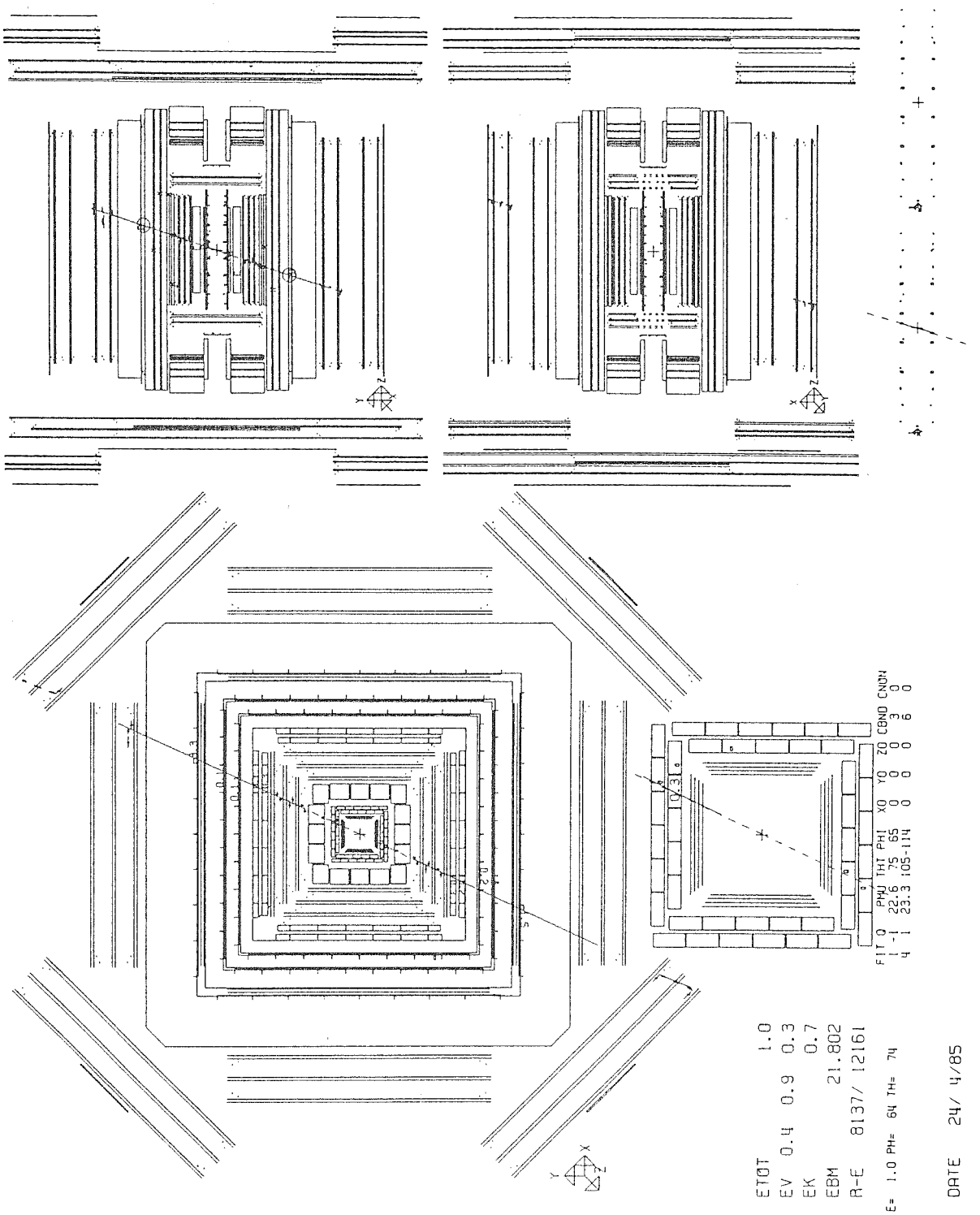

Figure 4.1 The graphic display of a muon pair event in Mark J detector.

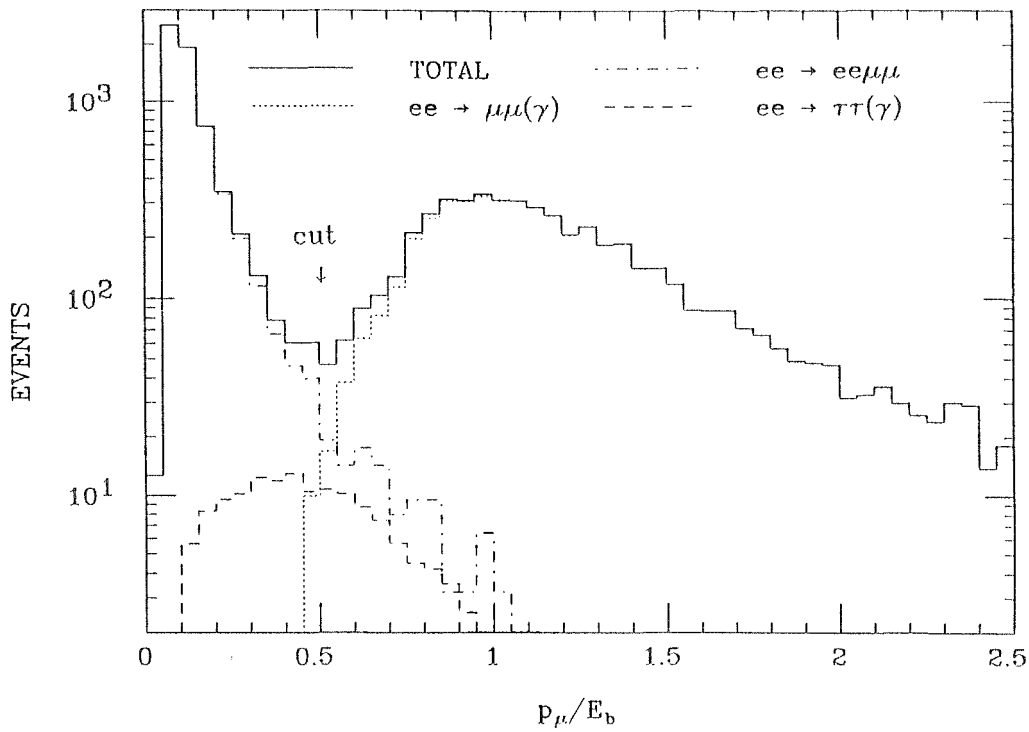

Figure 4.2 Momentum distributions of the more energetic muon of the processes $e^+e^- \rightarrow \mu^+\mu^-$, $e^+e^- \rightarrow e^+e^-\ \mu^+\mu^-$ and $e^+e^- \rightarrow \tau^+\tau^- \rightarrow \mu^+\mu^-\ \bar{\nu}_\tau\nu_\tau\bar{\nu}_\mu\nu_\mu$.

2. τ pair production, with both τ's decaying into muons and neutrinos, $e^+e^- \rightarrow \tau^+\tau^- \rightarrow \mu^+\mu^-\ \bar{\nu}_\tau\nu_\tau\bar{\nu}_\mu\nu_\mu$.

The characteristics of these events are quite different from those of muon pairs. Fig 4.2 is the momentum distribution of the muon with larger momentum. The detector acceptance and resolution are taken into account. The two photon process, $e^+e^- \rightarrow e^+e^-\ \mu^+\mu^-$, has its muon momentum peak at low value, thus can be easily rejected. τ pair production has its muon momenta at around one third of the beam energy because of the three body decay, but is suppressed by a factor of 0.03 for the branching ratio of τ leptonic decay is about 17.7%. Fig 4.3 shows the acollinearity distribution after requiring the larger momentum $p_{\mu_{max}} \geq E_{beam}/2$. The muons from τ decay or two photon process tend to be more acollinear. Because of the radiative correction, the muon pairs from one photon exchange can also be acollinear. By an

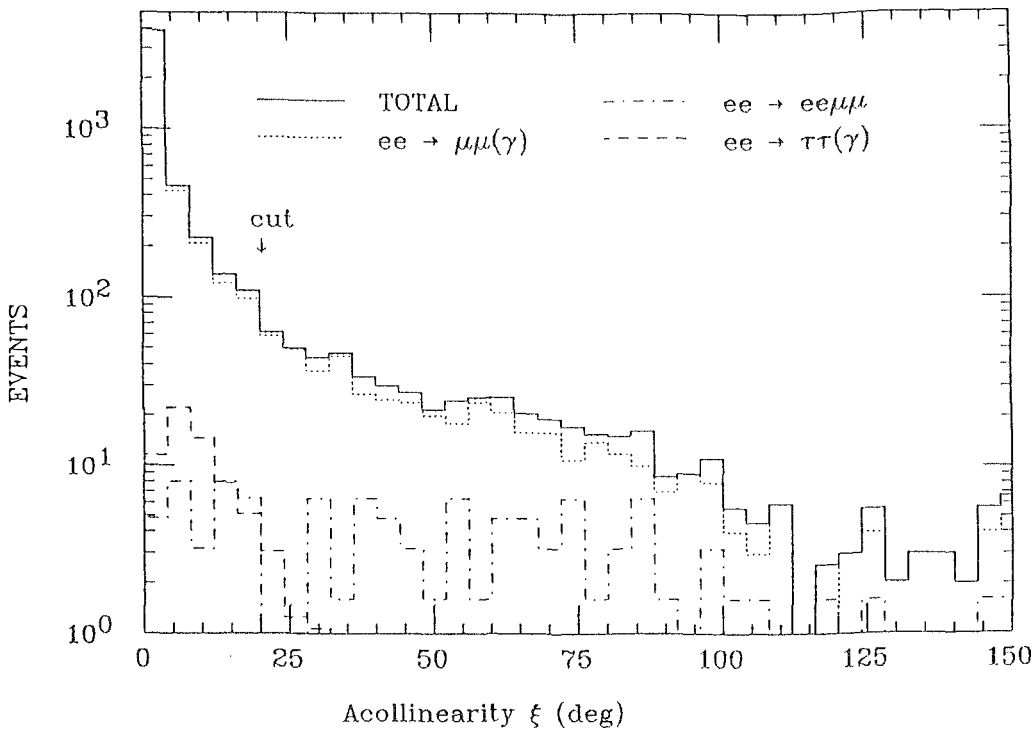

Figure 4.3 Acollinearity distributions of the muon pairs from the processes $e^+e^- \rightarrow \mu^+\mu^-$, $e^+e^- \rightarrow e^+e^-\ \mu^+\mu^-$ and $e^+e^- \rightarrow \tau^+\tau^- \rightarrow \mu^+\mu^-\ \bar{\nu}_\tau\nu_\tau\bar{\nu}_\mu\nu_\mu$ after the momentum cut $(p_\mu)_{max} \geq E_{beam}/2$.

acollinearity cut of $\xi \leq 20°$, the background from $e^+e^- \rightarrow e^+e^-\ \mu^+\mu^-$ and $e^+e^- \rightarrow \tau^+\tau^-$ is finally reduced to .5% and 1.% respectively at 35 GeV.

Fig 4.1 is a graphic display of the projections of a typical muon pair event. The muon tracks in both the inner and outer drift chambers are clearly drawn according to the fits to the hits. The tracks are slightly bent in the projection containing the beamline because of the toroid magnet. The position of the D-counter hits coincide with the tracks. The energies in the calorimeters are insignificant and are consistent with the two tracks being minimum ionizing tracks.

The systematic errors of the muon acceptance and charge asymmetry have been thoroughly studied. A large number of cosmic ray muon events (over 20000) are used in the checking the detector acceptance and charge asymmetry. The systematic errors of the R–value measurement, which is defined as the ratio of the observed cross

error source	ΔR (systematic)
detector acceptance	0.01
cosmic ray muon	0.001
luminosity error	0.03
two photon and τ pair	0.001
trigger inefficiency	< 0.005
total	0.032

Table 4.1 The systematic errors of R–value measurement.

error source	ΔA (%)(systematic)
charge misidentification	0.1
detector acceptance	1.0
trigger inefficiency	< 0.1
cosmic ray muons	negligible
two photon and τ pair	negligible
total	1.0

Table 4.2 The systematic errors of asymmetry measurement.

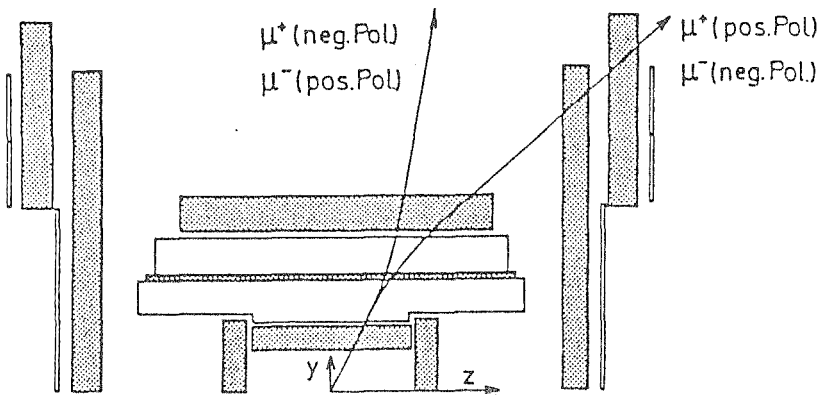

Figure 4.4 A schematic diagram of detector acceptance to positive and negative muons with different magnet polarities.

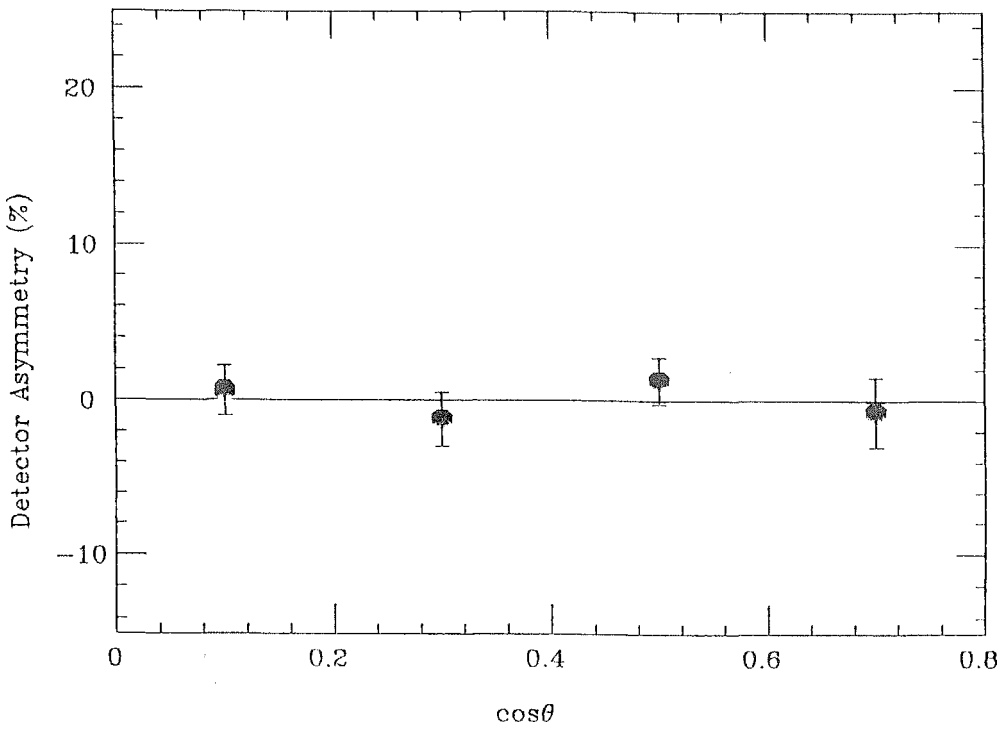

Figure 4.5 Detector asymmetry as a function of polar angle θ.

section to the QED cross section, are summarized in Table 4.1. When a cosmic ray muon penetrates the detector, the meantime difference of the hits in the D counters is at least 8.5ns. As the observed cosmic ray muon trigger rate is about .35 Hz, the rate of accepting a cosmic ray with meantime difference less than 4 ns is much less than 10^{-7}/sec. With the luminosity of $10^{31}/\text{cm}^2/\text{sec}$ at 35 GeV, the muon pair event rate is about 5×10^{-4}/sec. The background from the cosmic ray is then expected to be much less than 0.1%. It is confirmed by the absence of events between the muon pairs with meantime difference centered at zero and the cosmic ray muons rising at meantime difference of about 8 ns in Fig 3.12. The total detector acceptance with the kinematic cuts on the muons is estimated by the Monte Carlo simulation. The total systematic error is dominated by the luminosity uncertainty.

Table 4.2 summarizes the systematic errors of the muon charge asymmetry. In the muon pair sample, there are about 2% events at 35 GeV with both muon mea-

sured to have the same sign of charge. These events are not used in the asymmetry calculation. This implies that the probability of wrong charge assignment for both muons (which can not be separated from the sample) is less than 0.1%. The detector asymmetry may cause the acceptance in a given solid angle for positive muons to be different than for negative muons. This systematic error can be significantly decreased by alternating the polarity of the detector magnetic field. Fig 4.4 is a schematic picture of detector acceptance to positive and negative muons under different magnet polarities. Any acceptance asymmetry will produce effects which cancel for positive and negative magnetic polarity to the first order. Using cosmic ray muons with momenta greater than 10 GeV collected in equal amount with both magnet polarity, which should be equivalent to collinear muon pairs of the same energy, we obtain the detector asymmetry as a function of polar angle θ (Fig 4.5). From this it can be concluded that the systematic error of the asymmetry due to the detector acceptance is less than 1%, which actually dominates the total systematic error.

4.2 Cross section measurement

More than 7,000 muon pair events have been collected by the Mark J detector. To compare the measured cross section with the theory, Monte Carlo event generators including all radiative corrections, and a detector simulation are used. The acceptance at different energies is then calculated. Fig 4.6 shows the measured cross section after radiative correction compared to the expectation.

The R value is defined as

$$R_{\mu\mu} = \frac{\sigma_{\mu\mu}^{Exp}}{\sigma_{\mu\mu}^{QED}} = \frac{N_{\mu\mu}}{L\,\varepsilon\,\sigma_{\mu\mu}^{QED}}, \tag{4.1}$$

where L is the integrated luminosity, and $\sigma_{\mu\mu}^{QED}$ is the total cross section including radiative correction, and ϵ is the acceptance. The R values are given in Table 4.3

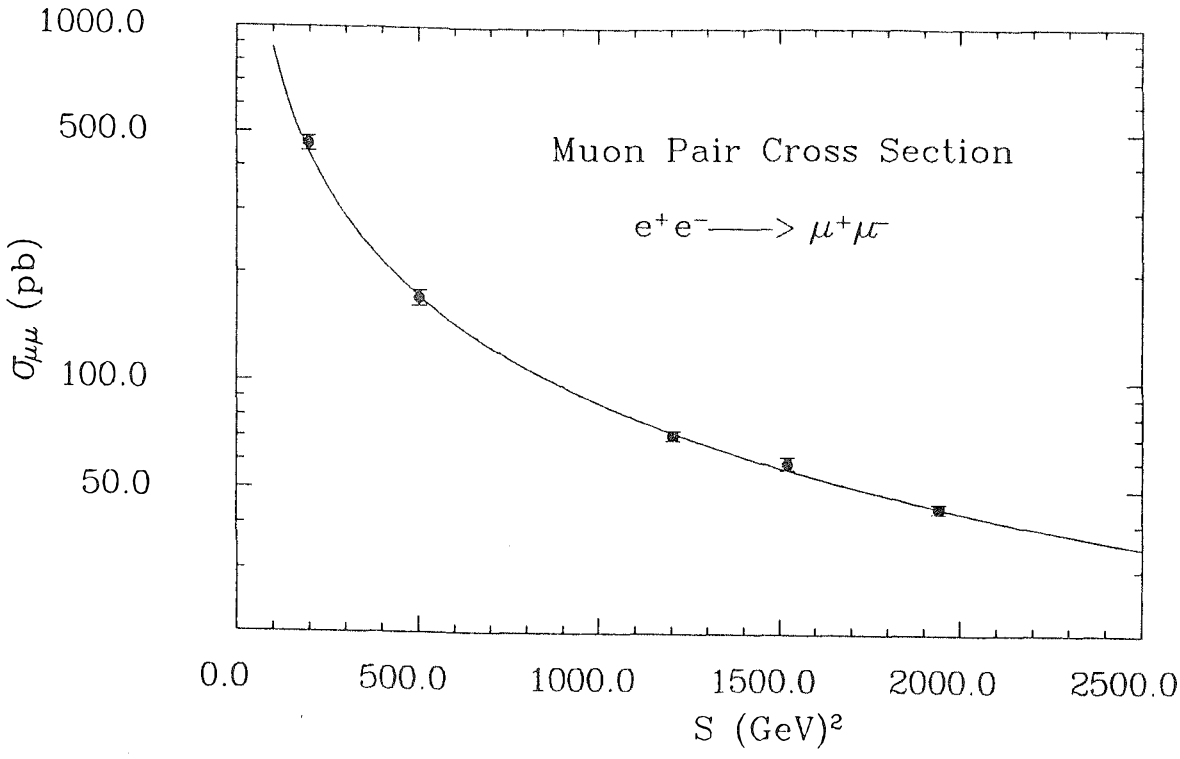

Figure 4.6 Cross section of muon pair production compared to electroweak expectation after radiative correction.

with $\sqrt{s}$ covered from 14 GeV to 46.8 GeV. The acceptance ϵ is defined as the fraction of $\mu^+\mu^-(\gamma)$ Monte Carlo events that pass the muon pair selection cuts. It takes into account not only the detector acceptance to the muons (as shown in Fig 3.11), but also the selection efficiency due to the kinematic cuts. Events with hard radiative photons, which have a large fraction of the total $\mu^+\mu^-(\gamma)$ cross section, can not be accepted due to the acollinearity and the muon momentum requirements.

The error in the table is statistical. The systematic error is estimated to be 3% and is dominated by the luminosity error.

4.3 Muon pair charge asymmetry

The standard model predicts a large muon pair charge asymmetry due to electroweak interference. In order to extract the Born term asymmetry, the data should be corrected by higher order contributions. Monte Carlo events are used to deter-

$\sqrt{s}\,(GeV)$	$L\,(pb^{-1})$	$N_{\mu\mu}$	ϵ	$\sigma^{QED}\,(nb)$	$R_{\mu\mu}$
14.0	1.6	469	0.422	0.660	1.05 $\pm$ .05
22.4	3.1	338	0.406	0.271	1.02 $\pm$ .05
34.7	105.8	4959	0.404	0.118	0.98 $\pm$ .014
39.0	14.5	544	0.379	0.094	1.05 $\pm$ .04
44.1	45.7	1297	0.380	0.075	1.00 $\pm$ .03

Table 4.3 Muon pair cross section measurement.

$\sqrt{s}\,(GeV)$	$A_{\mu\mu}(\lvert\cos\theta\rvert\leq 1.)(\%)$	$A_{\mu\mu}^{GWS}(\lvert\cos\theta\rvert\leq 1.)(\%)$
14.0	$+5.3 \pm 5.0$	-1.3
22.4	-4.3 ± 6.1	-3.4
34.7	-10.2 ± 1.5	-8.8
39.0	-11.9 ± 4.7	-11.6
44.1	-14.3 ± 3.1	-15.6

Table 4.4 Muon pair charge asymmetry of MARK J data.

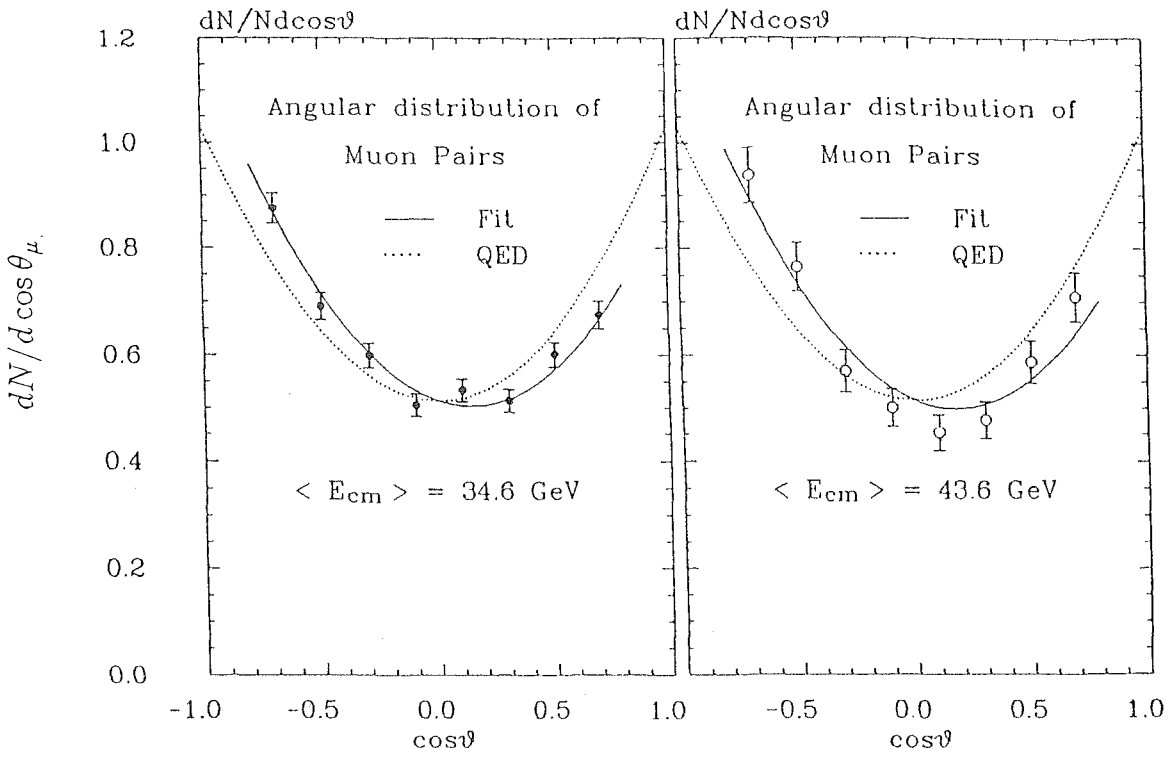

Figure 4.7 Angular distribution of the muon pair events at $\sqrt{s}$ =34.6 and 43.5 GeV.

mine the angular distribution after the cuts which is the same as those applied to data. It is parametrized as

$$\frac{d\sigma}{d\Omega} = F\{C[1+\cos^2\theta][1+\delta(\theta)] + A^{Born}\cos\theta\}, \tag{4.2}$$

where F and C are constants, δ is estimated as a polynomial. Because of the radiative photon the two muons are not always collinear. The polar angle of an event is therefore defined as a weighted average of both muons,

$$\cos\theta = \frac{(\vec{P}_{\mu^-} - \vec{P}_{\mu^+})_z}{|\vec{P}_{\mu^-} - \vec{P}_{\mu^+}|}. \tag{4.3}$$

The maximum likelihood method is then applied to fit the data to the distribution with A^{Born} as a free parameter to be determined. In this way, A^{Born} is considered as a parameter of a distribution rather than the forward-backward asymmetry. The detector acceptance doesn't effect the value as long as the the acceptance is symmetric (see Appendix D).

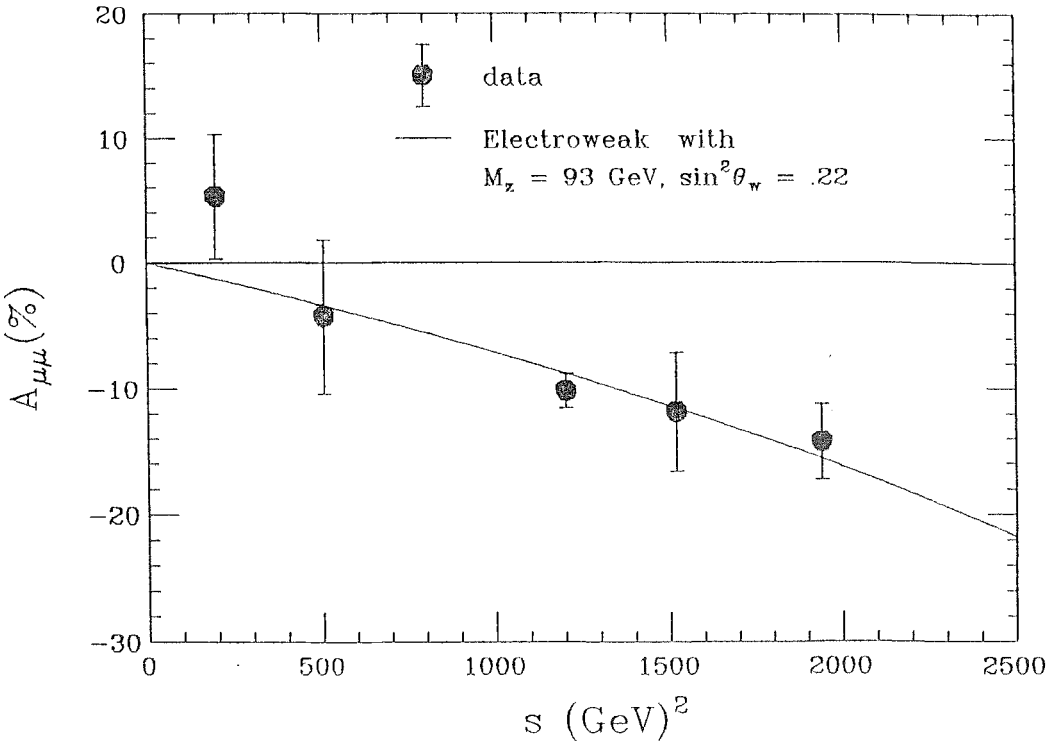

Figure 4.8 Charge asymmetry of muon pairs.

The asymmetry of all the data measured with the Mark J detector is given in Table 4.4. Fig 4.7 is the angular distribution of the muon pair events at $\sqrt{s}$ =34.6 and 43.5 GeV. Fig 4.8 shows the asymmetry in comparison with the standard model with M_Z=93 GeV and $\sin^2\theta_w$ =0.22 . The error given in the table is statistical. The systematic error is estimated to be less than 1%.

As pointed out in Chapter 2, radiative corrections to the asymmetry come from various diagrams with different sign, and cancellation may play an important role. By separating events with different acollinearity, we are able to see the contributions from different processes. Events from the interference of one and two photon exchange processes consist of two collinear muons while events with radiative photons tend to be acollinear. Fig 4.9 shows the asymmetry as a function of acollinearity. Our data are in good agreement with the standard model prediction. This can be considered as a test of the corrections to the asymmetry we used in obtaining the

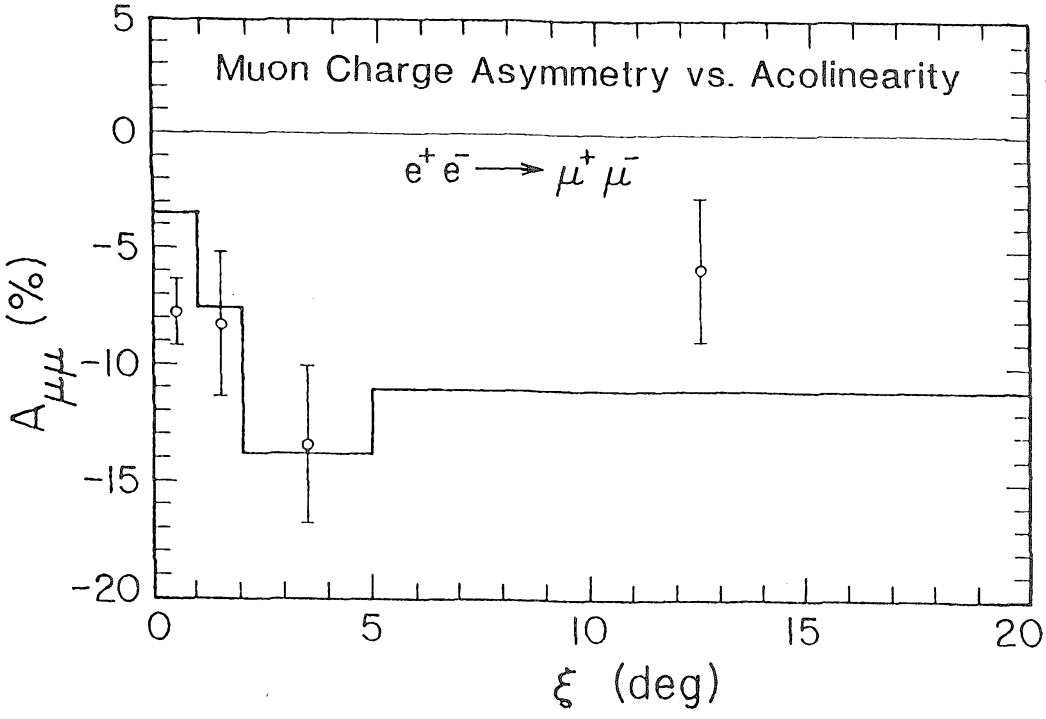

Figure 4.9 Charge asymmetry of muon pairs as a function of acollinearity.

Born term asymmetry.

4.4 Determination of electroweak parameters

The charge asymmetry and cross section measurements of muon pairs with high statistics gives a strong constraint on the electroweak parameters. To determine mass of the Z^o and $\sin^2\theta_w$, the χ^2 function is minimized,

$$\chi^2 = \left(\frac{F-1}{\sigma_L}\right)^2 + \sum_i \left(\frac{F\,R^i_{\mu\mu} - R^{th}_{\mu\mu}}{\sigma^i_{R_{\mu\mu}}}\right)^2 + \sum_i \left(\frac{A^i_{\mu\mu} - A^{th}_{\mu\mu}}{\sigma^i_{A_{\mu\mu}}}\right)^2. \qquad (4.4)$$

The theoretical expressions given in Chapter 1 are used. The systematic error of the luminosity is taken into account by introducing a normalization factor F. In this way, the luminosity error is considered as an overall shift independent of the beam energy. If there is a point-to-point systematic uncertainty of R-value, the total error of the R-value should be the quadratic sum of the systematic and statistical errors.

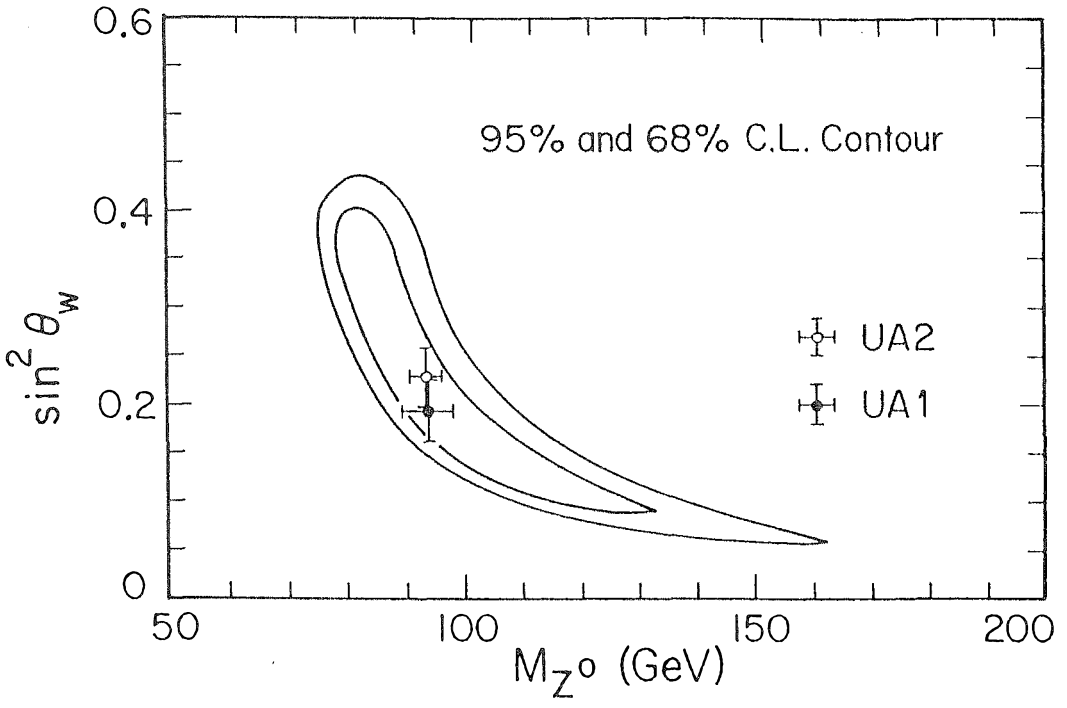

Figure 4.10 Determination of $\sin^2\theta_w$ and M_Z from the cross section and the asymmetry of muon pairs.

The 68% C.L. allowed region of $\sin^2\theta_w$ with M_Z fixed at 93 GeV would be increased by less than 0.001 if this systematic error is 1%. The effect is small because the statistical error is still dominating and $\sin^2\theta_w$ is less sensitive to the R-value than to the asymmetry. The 68% and 95% confidence level contours are drawn in Fig4.10 with the values given by UA1 [16] and UA2 [42] experiment plotted. If $\sin^2\theta_w = .22$, one obtains

$$M_{Z^0} = 91.0^{+4.0}_{-3.5}\text{GeV}, \tag{4.5}$$

and likewise, if M_{Z^0}=93 GeV,

$$\sin^2\theta_w = 0.20^{+0.04}_{-0.025}. \tag{4.6}$$

The values obtained are consistent within statistics with other experiments.

Assuming lepton universality ($g^e_A = g^\mu_A$, $g^e_V = g^\mu_V$) and the Z^0 mass as measured in $\bar{p}p$ collider, we can determine the vector and axial coupling constants of the

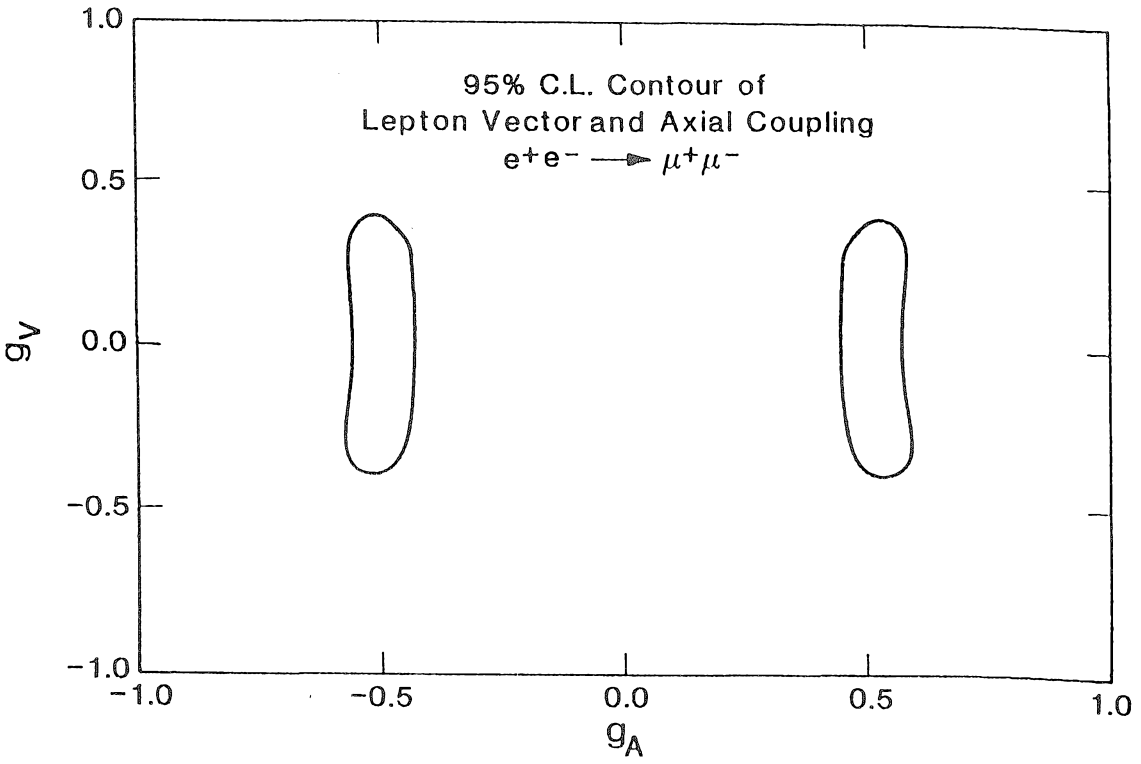

Figure 4.11 Determination of axial and vector coupling from the cross section and the asymmetry of muon pairs.

neutral current using the muon pair data. χ^2 of Eq 4.4 is minimized by varying g_A and g_V. The result of the fitting leads to two solutions for g_A and g_V, as shown in Fig 4.11 on the g_V–g_A plane. The ambiguity is resolved by using the neutrino electron scattering data. We obtain,

$$g_A^2 = 0.265 \pm 0.032, \quad g_V^2 = 0.038 \pm 0.043 \ . \tag{4.7}$$

These values are in good agreement with the standard model as shown in Table 2.1. The constraint on g_A is mainly from the asymmetry while that on g_V is mainly from the R–values.

The significance of the measurement of the Z^0 mass from muon pair production should not be underestimated in comparison with other experiments such as the observation of W and Z in $\bar{p}p$ collisions for the following reasons,

1. This is a test of the neutral current with only leptons involved. All the cor-

rections are well understood and the systematic errors are under control (Sec 4.1).

2. It measures the overall strength of the neutral currents with all the possible neutral bosons taken into account. Possible non-standard interactions may contribute to the same final state via virtual processes. Any significant deviation from observed physical Z^0 mass would signal the existence of additional neutral currents, which are predicted by some unified models.

4.5 Experimental limits on the extended electroweak models and composite structure

As the standard model is consistent with all the existing experimental phenomena, it is still possible that a model with a richer gauge boson structure governs the interaction at higher energy, or, as widely believed, higher level unification of all the interactions may eventually be found. The leptons and quarks can also be composite. All these extensions of the standard model would result in the deviation in the muon pair production from e^+e^- collision if the energy scale is not much higher than the center of mass energy explored in the experiments.

The deviation of lepton pair production from the standard model can be characterized by the traditional cutoff parameters $\Lambda_\pm$, which is a measure of the mass of an exchanged object which couples like the photon, or equivalently which is a measure of the radius of the leptons. The form factor is usually written as,

$$F(q^2) = 1 \mp \frac{q^2}{q^2 - \Lambda_\pm^2}. \tag{4.8}$$

where q^2 is the square of the momentum transfer. The incoherent scattering from the constituents takes place when the momentum transfer $Q^2 \gg 1/L^2$, where L is the size of the fermion, or in other words, the spacing between the constituents. In muon pair production, only s-channel contributes. The cross section is modified as

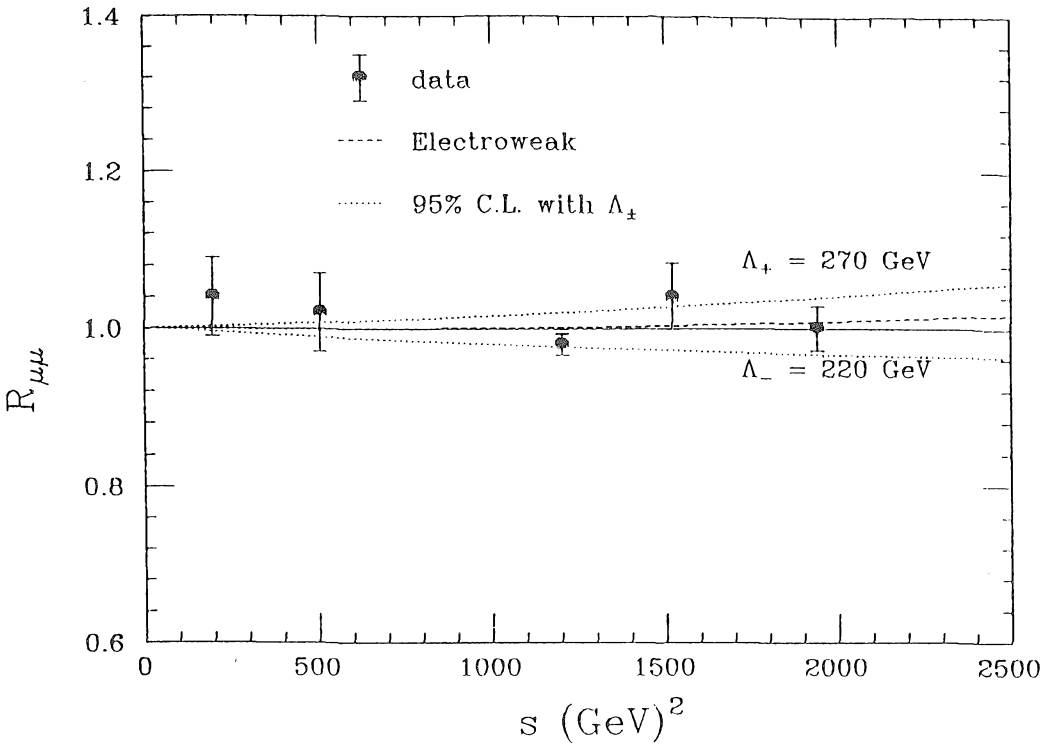

Figure 4.12 R–value and cutoff parameters of muon form factor.

$$\sigma_{\mu\mu} = \sigma_{\mu\mu}^{QED} F^2(s). \tag{4.9}$$

The limits on the cutoff parameters are obtained by fitting the measured R–values with

$$R_{\mu\mu} F^2(s). \tag{4.10}$$

At 95% confidence level, our data give,

$$\Lambda_+ \geq 270\text{GeV} \ , \quad \Lambda_- \geq 220\text{GeV}. \tag{4.11}$$

This can be translated into the limit on the size of the muon,

$$r_\mu \leq hc/\Lambda = 0.8 \times 10^{-3} fm. \tag{4.12}$$

Fig 4.12 shows the measured R values with the electroweak expectation and the 95% confidence level deviation.

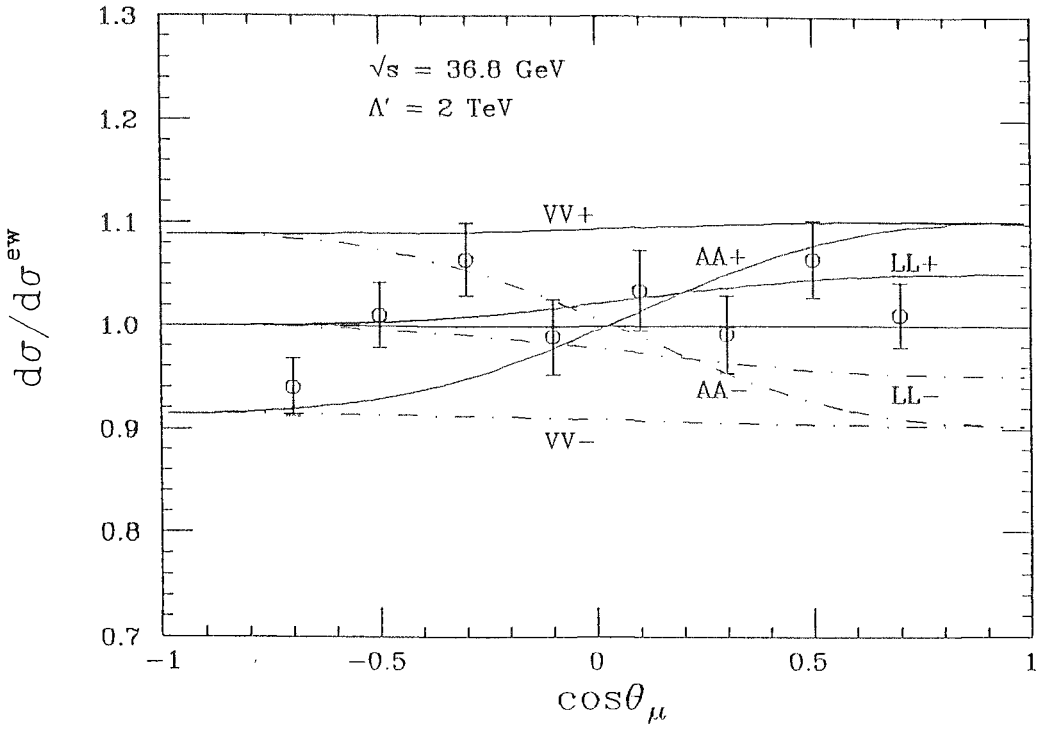

Figure 4.13 The ratio of the differential cross section of the composite model to that of the standard model prediction.

Another test for possible substructure is based on an effective Lagrangian of helicity-conserving contact interactions of the form [43],

$$\begin{aligned} L_{eff} &= \pm\frac{g^2}{2\Lambda'^2_{\pm}}[\eta_{LL}\bar{\psi}^e_L\gamma_\alpha\psi^e_L\bar{\psi}^\mu_L\gamma^\alpha\psi^\mu_L + \eta_{RR}\bar{\psi}^e_R\gamma_\alpha\psi^e_R\bar{\psi}^\mu_R\gamma^\alpha\psi^\mu_R \\ &\quad + \eta_{LR}(\bar{\psi}^e_L\gamma_\alpha\psi^e_L\bar{\psi}^\mu_R\gamma^\alpha\psi^\mu_R + \bar{\psi}^e_R\gamma_\alpha\psi^e_R\bar{\psi}^\mu_L\gamma^\alpha\psi^\mu_L)], \end{aligned} \tag{4.13}$$

where $\eta's$ are either 0 or ± 1, and ψ_L and ψ_R are left and right-handed components of the fermion field. $\Lambda'_{\pm}$ is defined such that $g^2/4\pi = 1$.

The cross section of muon pair production due to this effective Lagrangian and its interference with the standard model process is given in Appendix C. Also given in Appendix C is a plot of the effect of the contact interaction on Bhabha scattering. Although the lower limits of Λ's obtained from the study of Bhabha scattering is somewhat lower than what can be derived from muon pair data, the results are more general because of the identical initial and final states. It is necessary for e and μ to

have some common constituents in order that there could be a contact interaction at low energy.

In units of the standard model cross section, the interference term is of the order of $s/\alpha\Lambda'^2_{\pm}$ ($\simeq 0.04$ for $\Lambda' = 2$TeV, and $\sqrt{s}$=35 GeV).

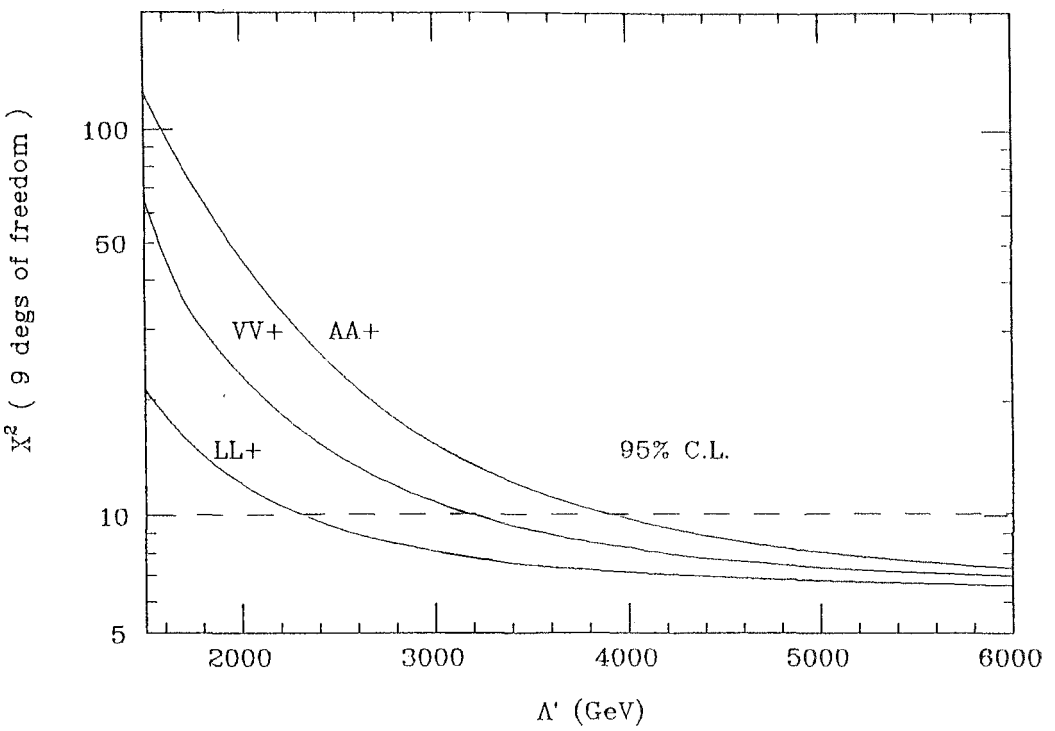

Figure 4.14 $\mathcal{X}^2$ as a function of Λ' for AA, VV and LL coupling.

Fig 4.13 shows the muon angular distribution divided by the standard model expectation with $\Lambda'_{\pm} = 2$TeV for various couplings of the contact interactions. It significantly changes the production rate as well as the charge asymmetry. The same $\mathcal{X}^2$ function of Eq 4.4 is minimized with respect to Λ', with $\sin^2\theta_w$ =.22 and M_Z =93 GeV. $\mathcal{X}^2$ as a function of Λ' is plotted in Fig 4.14.

Table 4.5 contains the 95% confidence level lower limits on $\Lambda'_{\pm}$ with various couplings using the muon pair R-value and asymmetry. The LL and RR couplings are indistinguishable at present energy with our data.

Some extended gauge theory models of the electroweak interaction, such as

coupling	η_{LL}	η_{RR}	η_{RL}	Λ_+(TeV)	Λ_-(TeV)
LL	1	0	0	2.3	1.6
RR	0	1	0	2.3	1.6
VV	1	1	1	3.2	2.4
AA	1	1	-1	3.9	3.1

Table 4.5 95% C.L. lower limit on $\Lambda'_{\pm}$ parameters in composite models.

SU(2)⊗U(1)⊗SU(2) or SU(2)⊗U(1)⊗U(1), have predicted the existence of a second neutral boson. Even more neutral bosons can be incorporated into the theory. Recent development of the superstring theory suggests that the low energy gauge groups are subgroups of E_6. This would also give rise to extra neutral currents because two other possible U(1)'s in E_6 may exist.

At the center of mass energy much lower than the mass of the additional neutral boson(s), an effective Lagrangian can be added to the standard model Lagrangian [44,45,46],

$$L^{NC}_{extended} = L^{NC}_{ST} + \frac{g^2}{2M_W^2} C j^{\mu}_{em} j^{em}_{\mu}. \tag{4.14}$$

From our data, we infer that $C < 2. \times 10^{-2}$ with 95% confidence level. This gives a tight constraint on extended gauge models of electroweak interaction.

Chapter 5

Results on radiative muon pair production

The good resolution of the electromagnetic calorimeter of the Mark J detector, together with the excellent muon spectrometer can be exploited to study the $\mu^+\mu^-\gamma$ events with large acceptance. The advantage of studying $\mu^+\mu^-\gamma$ events over other radiative lepton production is that the separation and the identification of the final state particles are unambiguous in our detector, even if the photon is collinear with the muon. The allowed phase space region is much larger than $e^+e^-\gamma$ or $\tau^+\tau^-\gamma$ processes.

5.1 Event selection

The $\mu^+\mu^-\gamma$ events are selected according to the following criteria,

- Two muon tracks with the same criteria as the in $\mu^+\mu^-$ event selection, i.e., two coincident muon trigger counter hits and two chamber tracks coming from the interaction point. Both muons are in good acceptance region of the detector, $\cos\theta_\mu < 0.8$.

- An electromagnetic shower with energy larger than $3\%\sqrt{s}$. The sum of the energy in the A, B and C counters is taken as the photon track energy since the leakage of the shower is negligible. The direction of the shower is computed

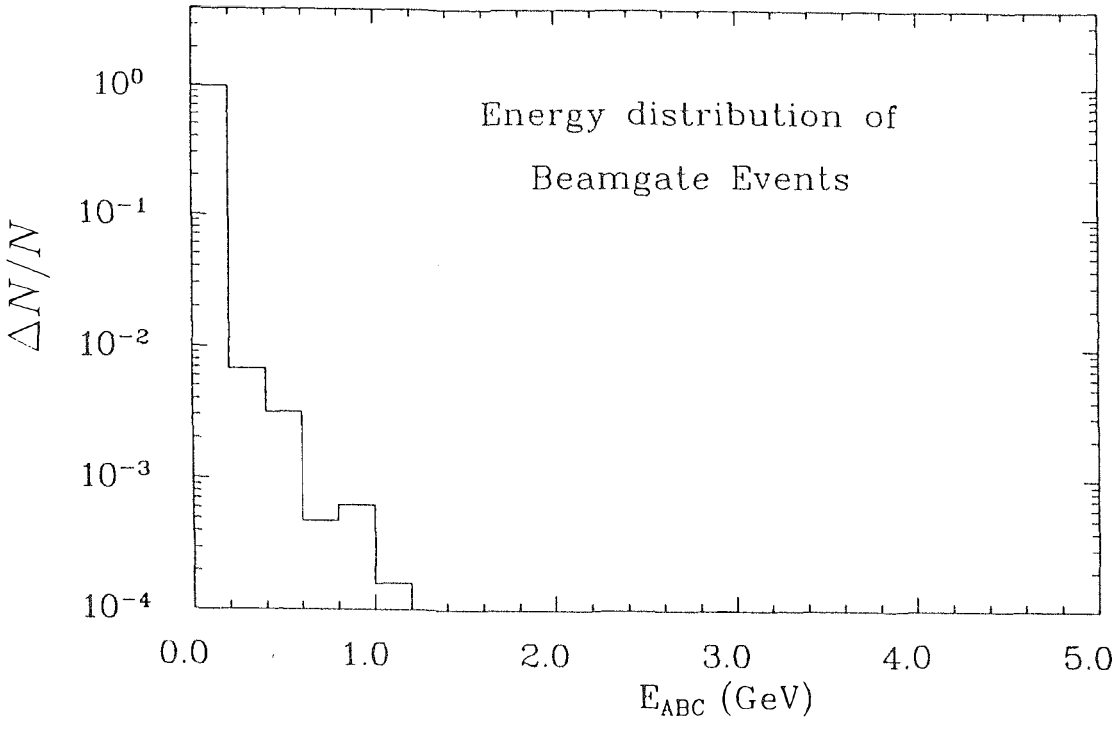

Figure 5.1 Energy in A+B+C counters of beamgate events

with the assumption that the particle is from the vertex point. The background energy from beam-gas interaction is estimated by the beamgate events in which the trigger gate is opened randomly at the e^+e^- crossing time. Fig 5.1 shows the energy in the ABC counters of these events. The probability of having ABC counter energy larger than 1 GeV from random background is less than .1% . The energy of a shower collinear with one of the muons ($\theta_{\mu\gamma} \leq 5^\circ$) is required to be larger than $6\%\sqrt{s}$ to reduce the effect of the minimum ionizing energy left by the muon in the same direction as the photon.

- No drift tube track matched with the electromagnetic shower if the shower is not collinear with the muon tracks ($\theta_{\mu\gamma} \geq 10^\circ$). The drift tubes actively cover the polar angle down to 12°. The probability of photon conversion is approximately 6% at normal incidence. Due to the large conversion probability of the photon before the vertex detector at small polar angles, the acceptance of the

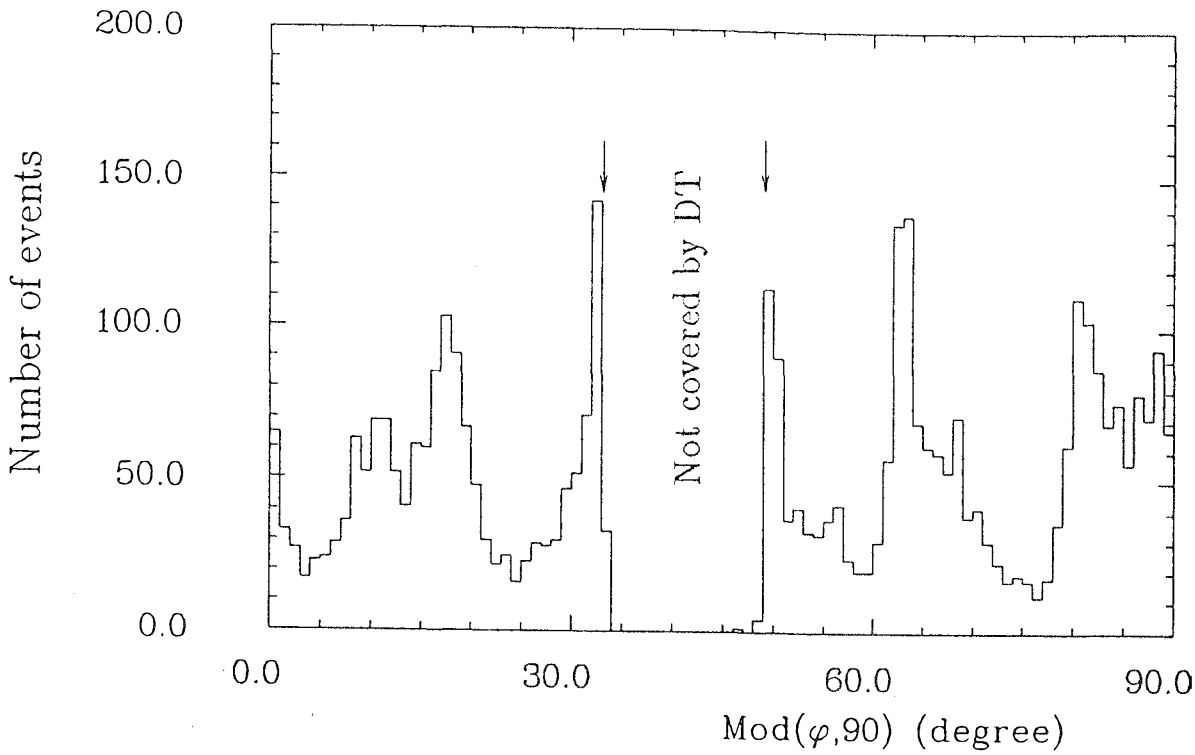

Figure 5.2 Azimuthal angular distribution of the accepted Bhabha events

shower is restricted to $|\cos\theta_\gamma| \leq 0.9$. The photon conversion probability has been checked by using two photon events. Its contribution to the uncertainty of the total cross section measurement should be less than0.5%.

- The shower not in the corner of the detector. The efficiency of the drift tube track fitting can be clearly seen in Fig 5.2, where the azimuthal angular distribution of the Bhabha events with two matched drift tube tracks is presented. Events with

$$|MOD(\phi, 90) - 41^\circ)| \leq 7^\circ \tag{5.1}$$

are rejected.

- Coplanarity. The accepted tracks are tested for coplanarity by requiring the sum of the three opening angles between the particles to be greater than 355°,

$$\delta\theta_{cop} = 360^\circ - (\theta_{\gamma\mu^-} + \theta_{\gamma\mu^+} + \theta_{\mu\mu}) \leq 5^\circ. \tag{5.2}$$

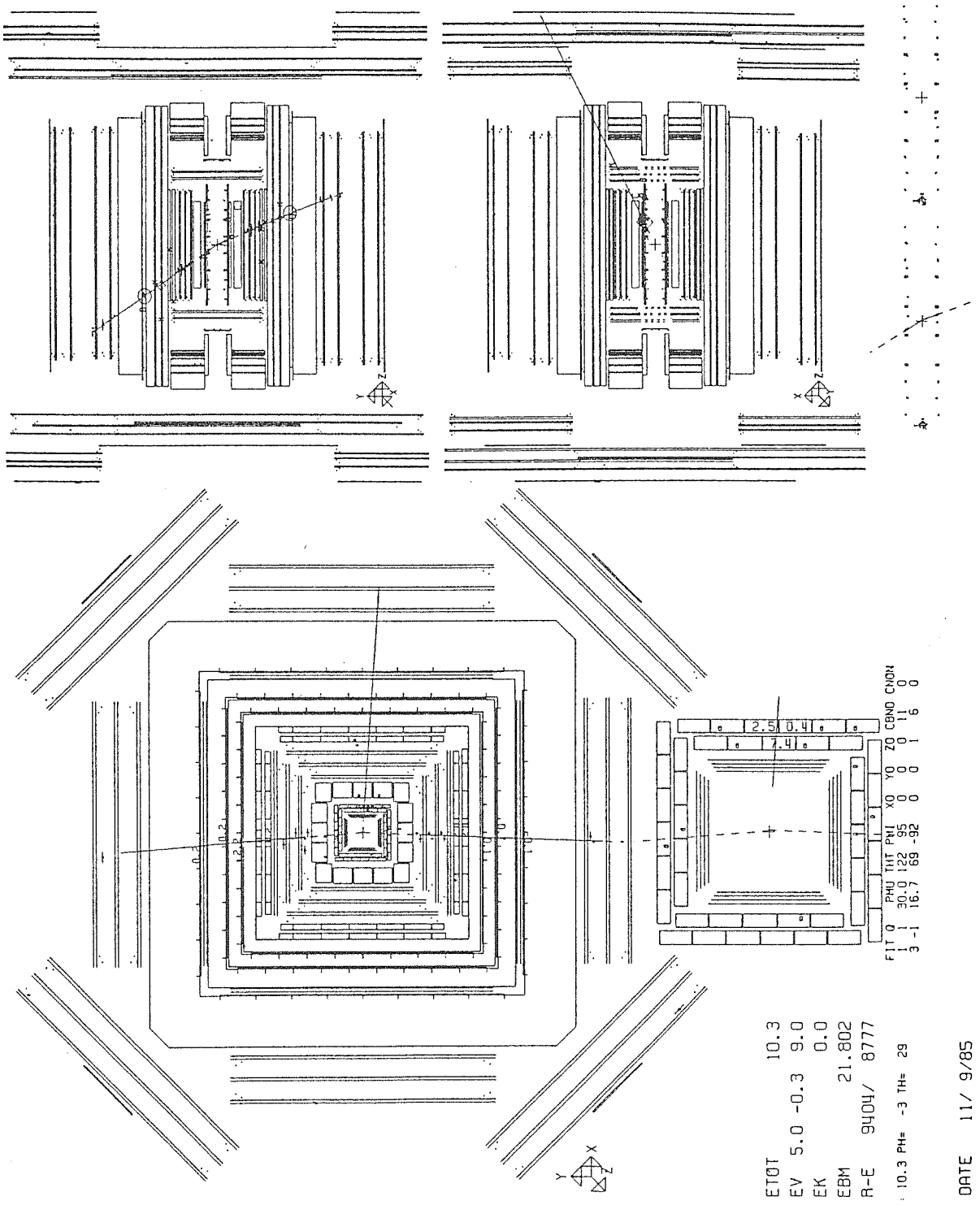

Figure 5.3 The graphic display of a $\mu^+\mu^-\gamma$ event in the Mark J detector.

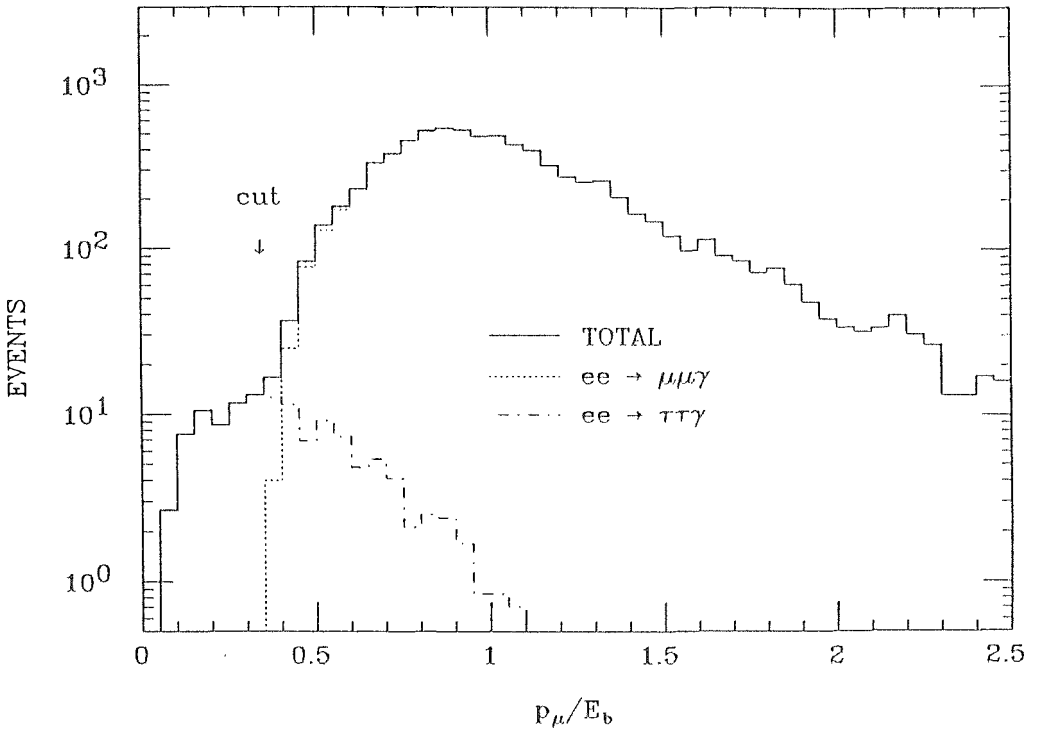

Figure 5.4 Muon momentum distribution of radiative τ and μ pair productions.

- At least one muon with momentum larger than one third of the beam energy to reduce the background from two photon process and τ pair production.

All accepted events are visually scanned on the graphic display. Fig 5.3 is a graphic display of a typical $\mu^+\mu^-\gamma$ event with both the side views and the end view. A shower in the electromagnetic calorimeter with no drift tube track matched is shown in the picture together with two clear muon tracks.

Except the $\mu^+\mu^-\gamma$ final state, other final states of e^+e^- annihilation may also satisfy the above criteria. The major background from the other physics processes are

1. Two photon process $e^+e^- \rightarrow e^+e^-\mu^+\mu^-$ with one electron detected and the drift tube track fit being inefficient.

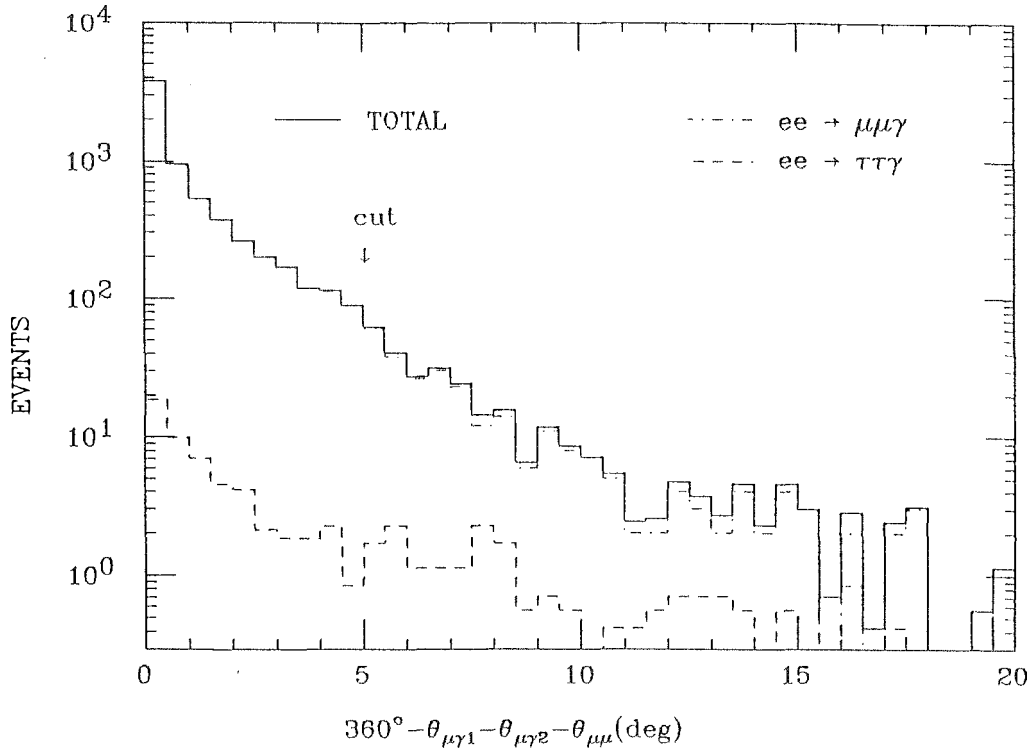

Figure 5.5 $\delta\theta_{cop}$ **distribution of radiative** τ **and** μ **pair productions.**

2. τ pair production with one τ decaying into a muon and the other into a hadron with a punchthrough to the D counters.

3. Radiative two photon process $e^+e^- \to e^+e^-\mu^+\mu^-\gamma$ with both electrons undetected.

4. $\tau^+\tau^-\gamma$ events with the $\tau's$ decaying into muons.

The first two processes mentioned above are basically rejected by visual scanning. Although the fitting of an electron track in drift tube may fail, the hits in front of the electromagnetic shower still indicate that it is a charged track. The contribution from this process is negligible after scanning. τ hadronic decay gives hadronic shower in the calorimeters. Most of those events with punchthrough can be recognized on the graphic display of the events. By scanning the Monte Carlo τ pair events, we have estimated that the background from this process is less than 0.5%.

Theoretical calculations of radiative two photon process has been studied [47]. The radiative corrections to the cross section of two photon muon pairs is shown to be fairly small under ordinary experimental cuts($\delta\sigma = 1pb$). The acceptance of $\mu^+\mu^-\gamma$ final state from radiative two photon process under our cuts described above will be very small because the muon pairs in these events tend to be low energy and more acoplanar and the photon tends to be collinear with one of the muons. These events therefore tend to fail the momentum and coplanarity criteria. This background is expected to be negligible.

The radiative τ pair production with both τ's decaying into muons is another background source. As in the muon pair analysis, the muon momentum distributions help to separate radiative τ pair events from radiative muon pair events(Fig 5.4). Because of the undetected neutrinos, the three particles in the final state of radiative τ pair event tend to be more acoplanar. Fig 5.5 gives the $\delta\theta_{cop}$ distributions of radiative τ and muon pair events. The Monte Carlo simulation shows that the background from radiative τ pair production is about 0.5%.

5.2 Event reconstruction

A complete measurement of the directions and momenta of the particles in the $\mu^+\mu^-\gamma$ final state is overconstrained. Taking the advantage of the the good muon angular resolution of the Mark J detector, the momenta of the particles can be more precisely reconstructed from the orientation of the tracks using the energy-momentum conservation. This yields,

$$E_\gamma = \frac{2E_{beam}(1-\cos\xi)}{1-(\cos\theta_{\gamma\mu^+}+\cos\theta_{\gamma\mu^-}+\cos\xi)}, \tag{5.3}$$

$$P_{\mu^+} = \frac{2E_{beam}-E_\gamma(1-\cos\theta_{\gamma\mu^-})}{1+\cos\xi}, \tag{5.4}$$

$$P_{\mu^-} = \frac{2E_{beam}-E_\gamma(1-\cos\theta_{\gamma\mu^+})}{1+\cos\xi}, \tag{5.5}$$

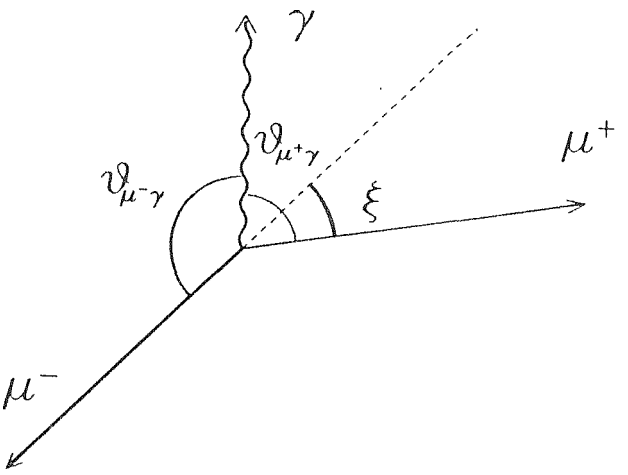

Figure 5.6 Schematic diagram of $\mu^+\mu^-\gamma$ event topology.

where ξ is the acollinearity of muon pair. The uncertainty is mainly from the photon angular measurement, which is much worse than that of the muons. In case of the sum of the opening angles differing from 360°, the direction of the photon is projected to make the event coplanar. However, Eq 5.3 is only used to calculated the photon energy if the photon is not collinear with one of the muons ($\theta_{\mu\gamma} \geq 10°$), because E_γ is not well determined if all the particles are along the same line. Otherwise the measured the photon energy is taken. Muon momenta are always calculated by (4.4) and (4.5), with E_γ being the the calculated photon energy or the measured photon energy depending on the topology of the event.

The invariant masses of the different particle pairs are computed. From the Monte Carlo events, the resolution of the $\mu\gamma$ invariant mass is expected to be $\sigma_{M_{\mu\gamma}}$=3% at 35 GeV.

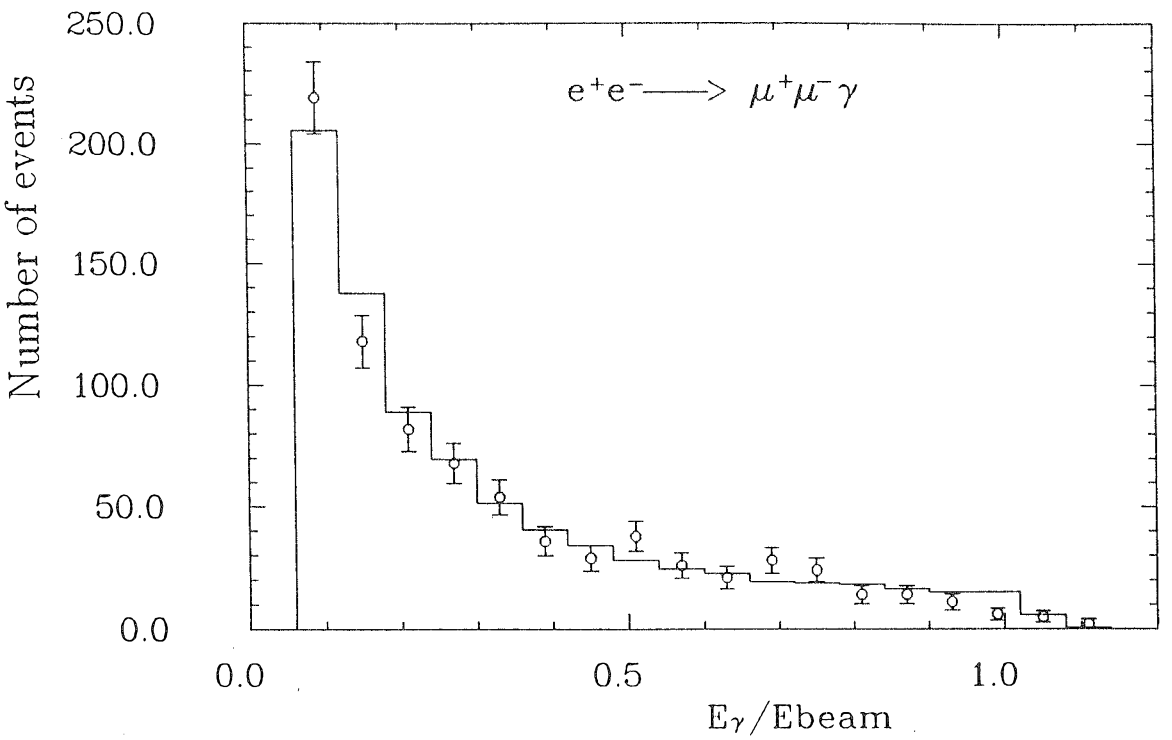

Figure 5.7 Photon energy distribution of $\mu^+\mu^-\gamma$ events.

5.3 Comparison with the standard model

Table 5.1 shows the comparison of number of observed events with that expected from the standard model. Various distributions of the selected events are shown in Fig 5.7 – Fig 5.13 in comparison with the Monte Carlo prediction of the electroweak theory. The data are in good agreement with the standard model to order α^3.

It should be noted that the acceptance of QED events are practically the same,

$\sqrt{s}$ GeV	N_{obs}	N_{MC}
34.7	568	580
42.8	227	231

Table 5.1 Number of observed $\mu^+\mu^-\gamma$ events compared to Monte Carlo.

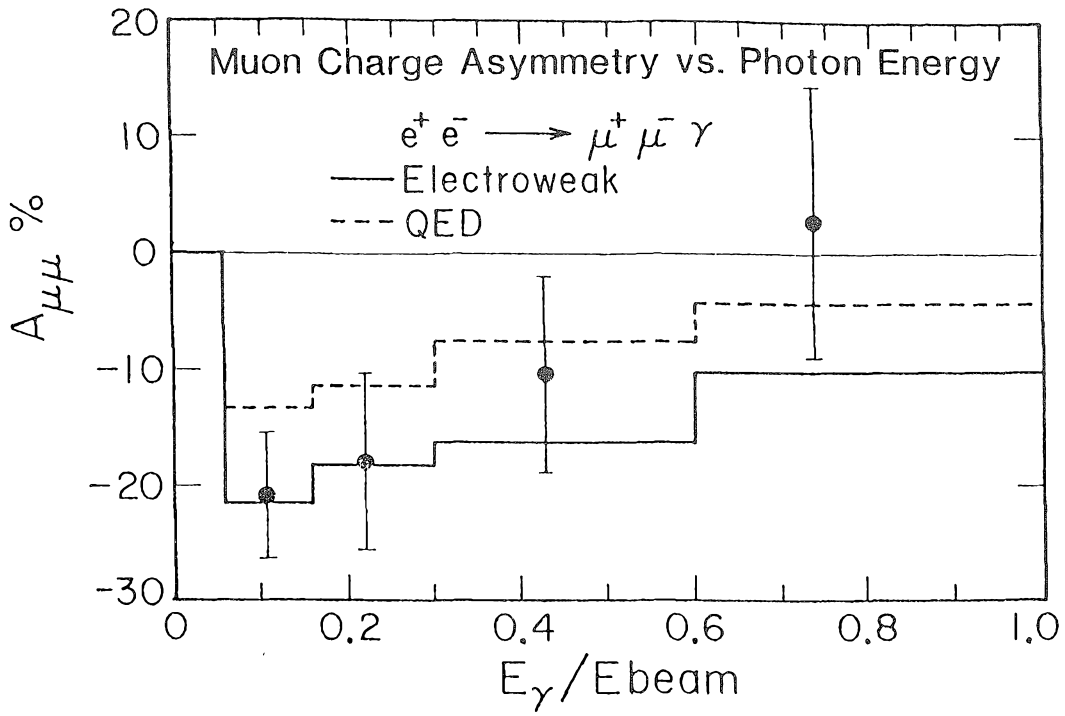

Figure 5.8 Muon angular distribution of $\mu^+\mu^-\gamma$ events.

whether QED or the electroweak theory is used. The only significant difference lies in the charge asymmetry.

The energy and invariant mass in the plots are scaled by the beam energy or the center of mass energy. Luminosity at different energies is taken into account in Monte Carlo simulation. Since the cuts are scaled by the center of mass energy, the QED expectation of all the distributions are nearly independent of $\sqrt{s}$. Higher order corrections, such as vacuum polarization in the photon propagator, would give a logarithmic increase in cross section.

The photon energy distribution (Fig 5.7) peaks at low energy as expected due to the nature of radiation. The high peak of the photon energy distribution at $E_\gamma \rightarrow E_{beam}$ is suppressed by the fact that the detector can not resolve a very close muon pair. The acceptance of events with muon acollinearity greater than 160° is practically zero.

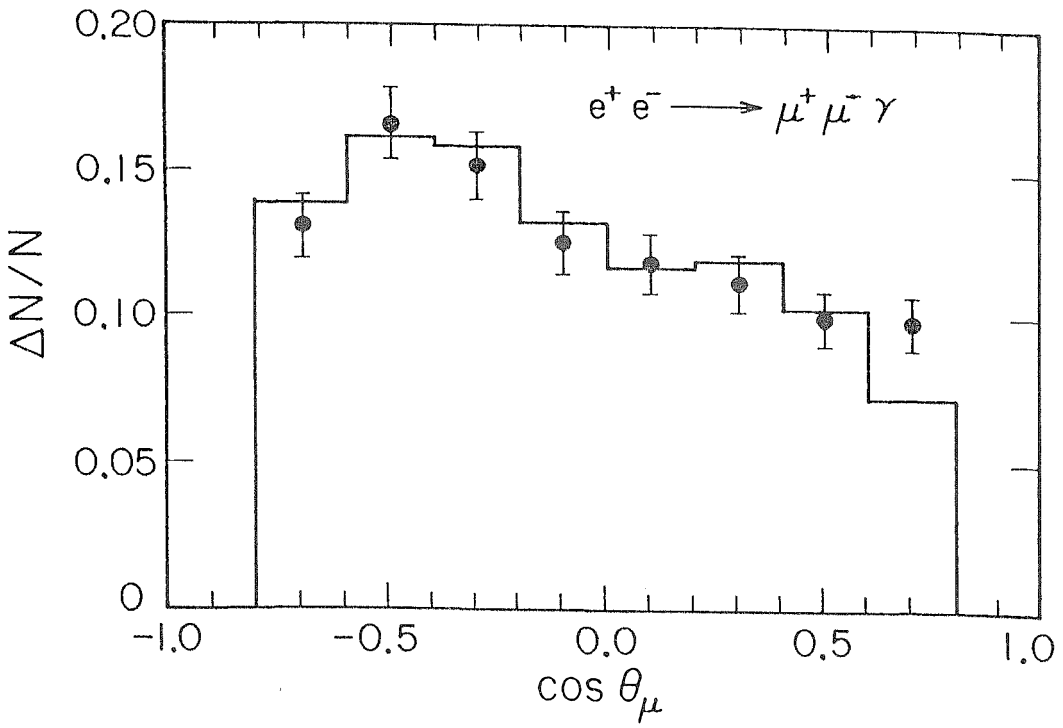

Figure 5.9 Muon charge asymmetry as a function of photon energy.

As discussed in Chapter 2, the interference between the initial and the final state radiation of one photon exchange process gives a large forward-backward charge asymmetry. The electroweak interference enhances the asymmetry in magnitude. The angular distribution of the muon production is shown in Fig 5.8. The observed asymmetry is compared with the electroweak theory and QED in Table 4.2 Although statistics does not allow to differentiate electroweak theory from QED, the interference of two different C parity state is evident.

The dependence of the asymmetry on the photon energy is shown in Fig 5.9. The

A^{obs}	A^{EW}	A^{QED}
-14.7 ± 3.8	$-18. \pm 1.3$	$-12. \pm 1.3$

Table 5.2 Observed muon Charge asymmetry compared to the electroweak theory and QED.

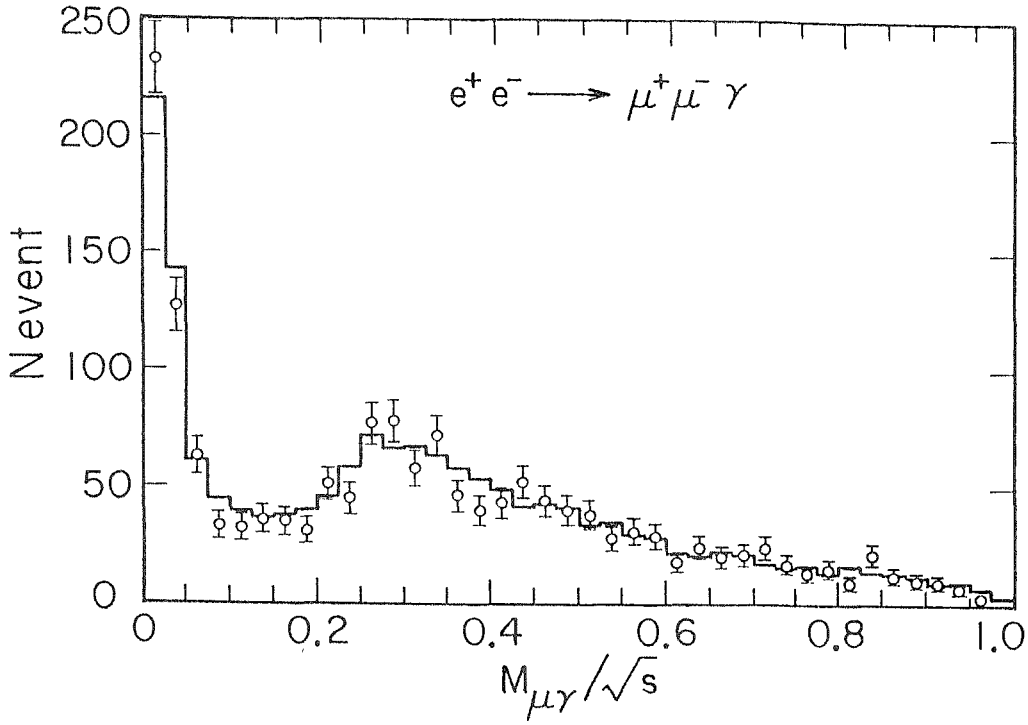

Figure 5.10 $\mu\gamma$ **invariant mass distribution of** $\mu^+\mu^-\gamma$ **events.**

data show clearly the tendency towards larger asymmetry at lower photon energies. The soft photon radiation is part of the correction to the dimuon sample, so is the two photon and one photon exchange interference. The negative asymmetry of soft photon radiative events tends to cancel the positive asymmetry of the events from the interference of one and two photon exchange process. Although the radiative corrections to the asymmetry of individual diagrams are relatively large, the total correction is not significant under our kinematic cuts. The good agreement between the data and the expectation, as shown in Fig 5.9 and Fig 4.9, confirms the validity of the radiative corrections to the dimuon charge asymmetry.

Fig 5.10 shows the $\mu\gamma$ invariant mass distribution. Since the radiative photon tends to be in the low energy region and collinear with one of the muons (hence antiparallel with the other), the $\mu\gamma$ invariant mass distribution shows peaks at zero and at $.25\sqrt{s}$. Good agreement between data and expectation indicates no production

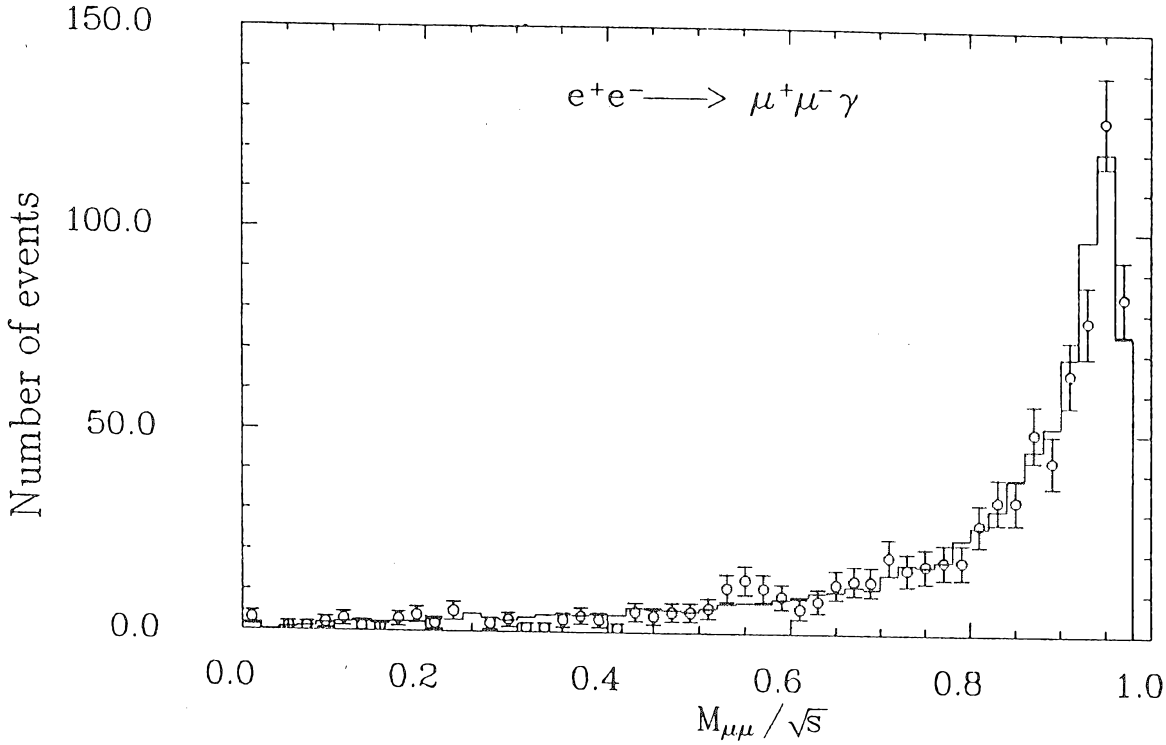

Figure 5.11 Muon pair invariant mass of $\mu^+\mu^-\gamma$ events.

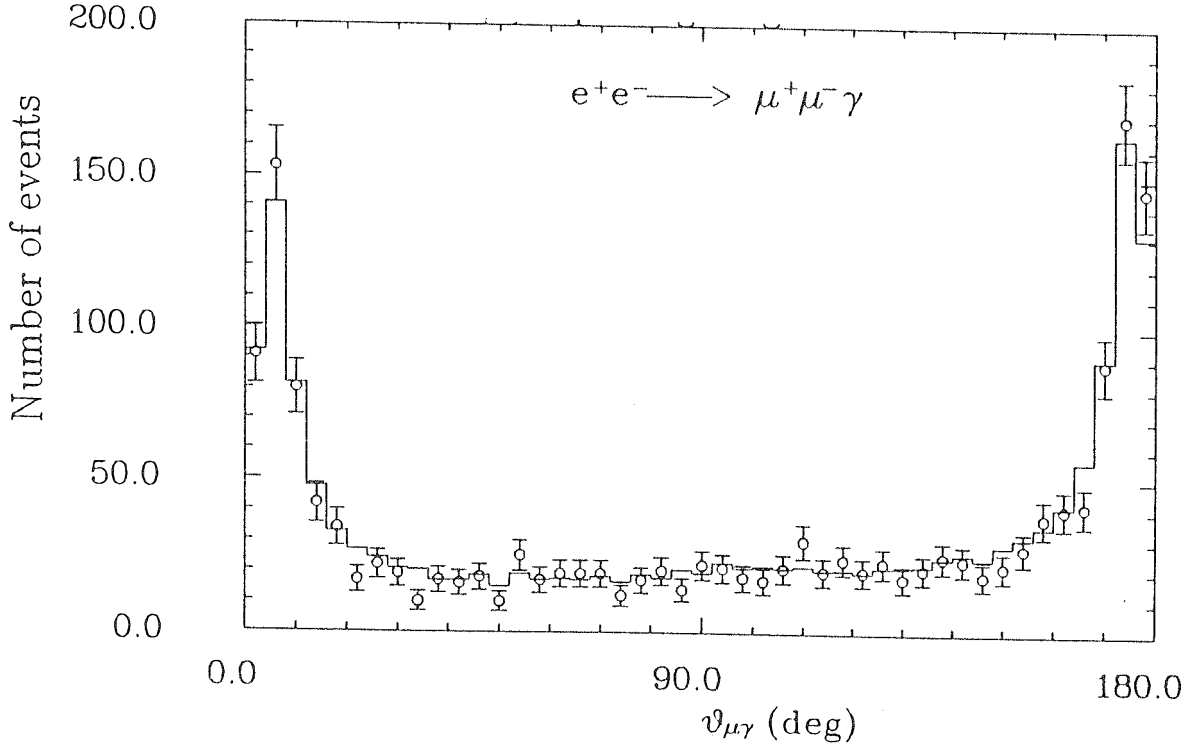

Figure 5.12 $\mu\gamma$ opening angle distribution of $\mu^+\mu^-\gamma$ events.

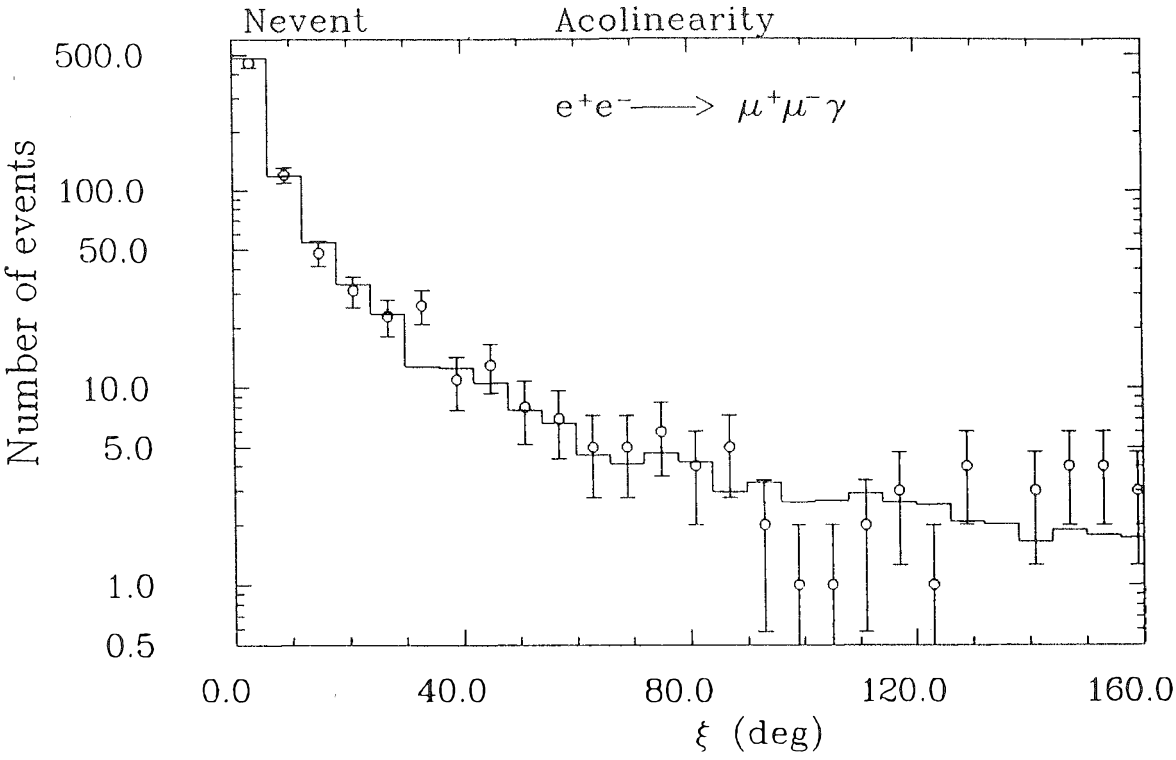

Figure 5.13 Muon acollinearity distribution of $\mu^+\mu^-\gamma$ events.

of excited muons, as discussed in the next chapter.

To give a complete comparison between the electroweak theory and the observation, higher order diagrams have to be taken into account. An estimate of the QED corrections of all orders to $\mu^+\mu^-\gamma$ events is made in Appendix B, though the complete calculation of order of α^4 is not available. According to our selection cuts the high order correction to the cross section is expected to be $\pm 3\%$, while the correction to the charge asymmetry is less than $+1.5\%$. Therefore the higher order correction is of the same order of magnitude as that of the statistical error in our observation.

Although it has been shown in the previous section that the total background is expected to be about 1%, it is necessary to study how they contribute in the various distributions, especially for the $\mu\gamma$ invariant mass distribution because it will be used in searching for excited muon production. Any significant excess of

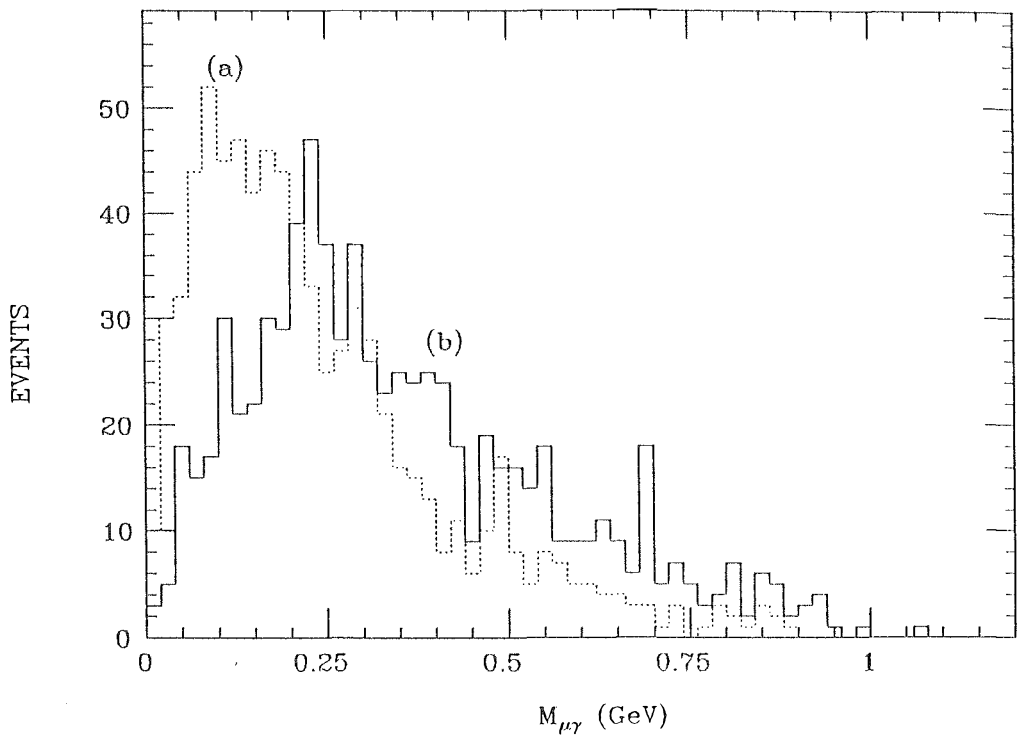

Figure 5.14 $\mu\gamma$ invariant mass distribution of radiative τ pair production using a) measured muon momentum and photon energy, b) calculated muon momentum and photon energy with kinematic constraints.

events in a particular invariant mass region due to background would give a false signal or deviation from the standard model prediction. Because the muons from τ decays have lower momenta, τ background would give low $\mu\gamma$ invariant mass. However, when the kinematic constraints based on angles are imposed onto the three particles in the final states, the $\mu\gamma$ invariant mass distribution shifts to the higher value and becomes flatter(Fig 5.14). Because the particles in the final state tend to be more separated, the events in the low mass region are absent. In the high mass region, the distribution resembles that of $\mu^+\mu^-\gamma$ events and does not contribute to a particular region significantly. The contribution to anywhere in the $\mu\gamma$ distribution is less than 1%.

In summary, the observed $\mu^+\mu^-\gamma$ events are in good agreement with the electroweak theory of the order of α^3.

Chapter 6

Search for excited muons

If leptons are composite, excited states are expected. A spin one half excited muon, μ^* , may be pair produced or it may be coupled to a muon and a photon due to radiative transition coupling between normal and excited muon. The production of these particles will show significant excess in $\mu^+\mu^-\gamma$ or $\mu^+\mu^-\gamma\gamma$ events because of the decay of μ^* after its production. Stringent limits can be obtained by comparing the $\mu^+\mu^-\gamma$ and $\mu^+\mu^-\gamma\gamma$ events with the standard model.

6.1 Search for μ^* pair productions

The lowest order cross section of heavy spin half pointlike lepton production is,

$$\frac{d\sigma}{d\Omega} = \frac{\alpha^2}{4s}\beta(1+\cos^2\theta+(1-\beta^2)\sin^2\theta), \tag{6.1}$$

$$\text{where} \quad \beta = \sqrt{1-(\frac{m_{\mu^*}}{E_b})^2}. \tag{6.2}$$

If the lepton is composite, a form factor must be introduced, giving the total cross section,

$$\sigma = \frac{4\pi\alpha}{3s}(\frac{3\beta-\beta^3}{2}) \mid F(s) \mid^2 . \tag{6.3}$$

The excited muon will subsequently decay into $\mu\gamma$ after its production. The experimental signature of this process is the production of $\mu^+\mu^-\gamma\gamma$ events.

The $\mu^+\mu^-\gamma\gamma$ events from e^+e^- annihilation are selected by requiring two muon tracks and two separated photon tracks, each with energy greater than 3% of the

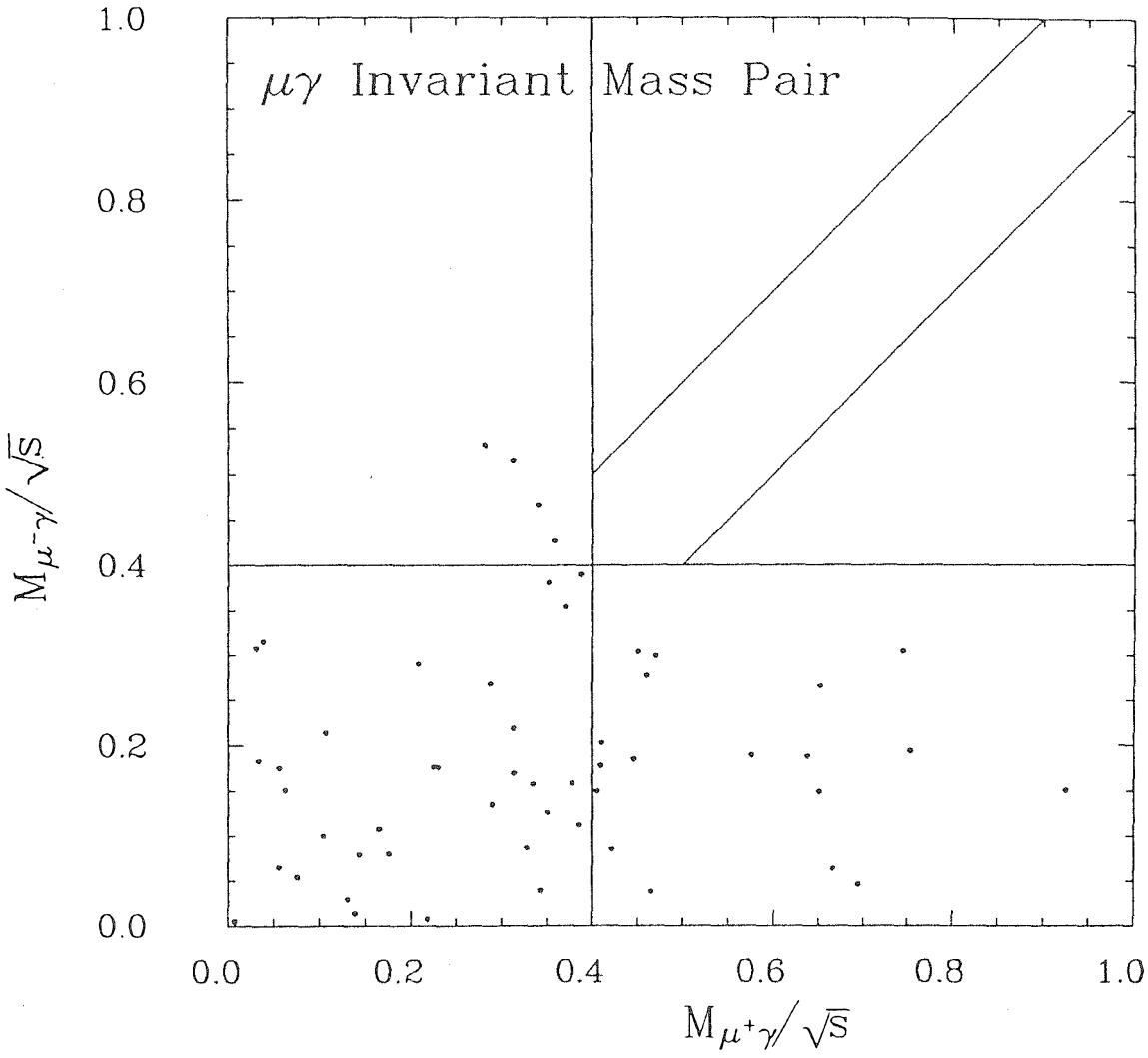

Figure 6.1 Invariant mass pairs of $\mu^+\mu^-\gamma\gamma$ events.

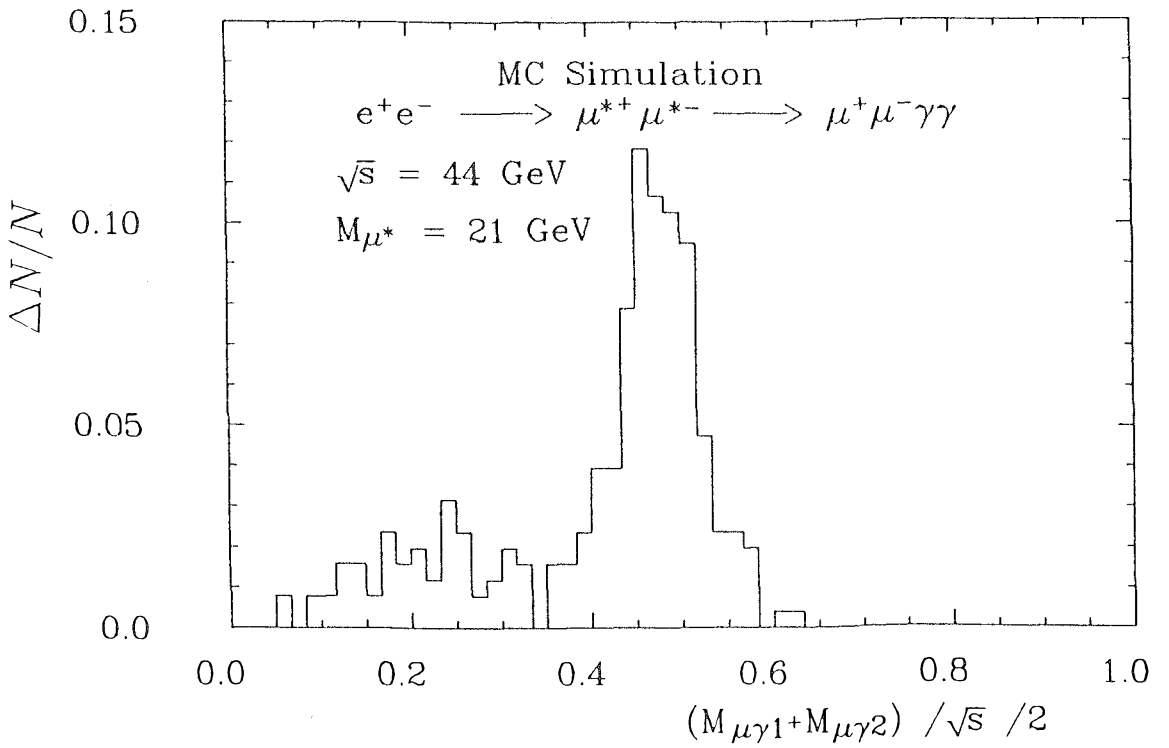

Figure 6.2 MC simulation of detector response to the μ^* pair production

center of mass energy. The opening angles between the photon and muons are required to be larger than 10°.

If a μ^* pair is produced, one of the two combinations of $\mu\gamma$ mass pairs would have $M_{\mu^+\gamma 1} = M_{\mu^-\gamma 2}$. Therefore a region near the diagonal in a $\mu\gamma$ invariant mass scattered plot is used to search for excited muon. Fig 6.1 is the plot of the selected $\mu^+\mu^-\gamma\gamma$ events. To avoid possible QED background in the low mass region, only the high mass region ($M_{\mu\gamma} \geq 0.4\sqrt{s}$) is used. No events are observed above this limit.

Monte Carlo events of $e^+e^- \rightarrow \mu^{*+}\mu^{*-} \rightarrow \mu^+\mu^-\gamma\gamma$ are generated including the radiative corrections and photon vacuum polarization. The generated events are passed through the detector simulation. The data selection cuts are applied to the events of the Monte Carlo simulation exactly as for real data. The acceptance is computed. Fig 6.2 shows the detector response to the μ^* production, where only

the events with $\mid M_{\mu^+\gamma 1} - M_{\mu^-\gamma 2} \mid \leq 0.1\sqrt{s}$ are used.

The 95% confidence level lower limit on the mass of the μ^* is then obtained with the assumption that the form factor of the μ^* is 1. For instance, by using the 3pb^{-1} data at 46.3 GeV, the mass region from 20 to 23 GeV can be excluded at the 95% C.L..

If the μ^* has a very low mass, the μ^* pair production with subsequent decay will increase the muon pair cross section. The acceptance is also estimated by the Monte Carlo method. Using data at 44 GeV, the 95% C.L. lower limit on the mass can be obtained: $M_{\mu^*} \geq 19\text{GeV}$.

Combining the limits from two methods with all the data, the 95% C.L. lower limit on the mass of μ^* is

$$M_{\mu^*} \geq 23\text{GeV}. \tag{6.4}$$

6.2 Single production of excited muons

It has been postulated that the coupling of μ^* to $\mu\gamma$ is governed by the effective Lagrangian [48],

$$L_{eff} = e\lambda \left(\overline{\Psi}_{l^*} \sigma^{\mu\nu} \Psi_l F_{\mu\nu} + h.c. \right), \tag{6.5}$$

where $F_{\mu\nu}$ is the electromagnetic field tensor, and λ is the coupling. The differential cross section of this process is

$$\frac{d\sigma}{d\Omega} = \alpha^2\lambda^2 \frac{(s - M_{\mu^*}^2)^2}{s^3} \left((s + M_{\mu^*}^2) - (s - M_{\mu^*}^2)\cos^2\theta \right). \tag{6.6}$$

Taking into account two charge states, the total cross section of the production is

$$\sigma_T \left(e^+e^- \rightarrow \mu^{*+}\mu^- / \mu^+\mu^{*-} \right) = \frac{16\,\pi\,\alpha^2\,\lambda^2}{3} \frac{(s - M^2)^2 (s + 2M^2)}{s^3}. \tag{6.7}$$

The experimental signature for the single μ^* production, and its subsequent decay into $\mu\gamma$, is an excess of events at μ^* mass in $\mu\gamma$ invariant mass distribution of the $\mu^+\mu^-\gamma$ sample. Fig 6.3 shows the Monte Carlo simulation of the detector

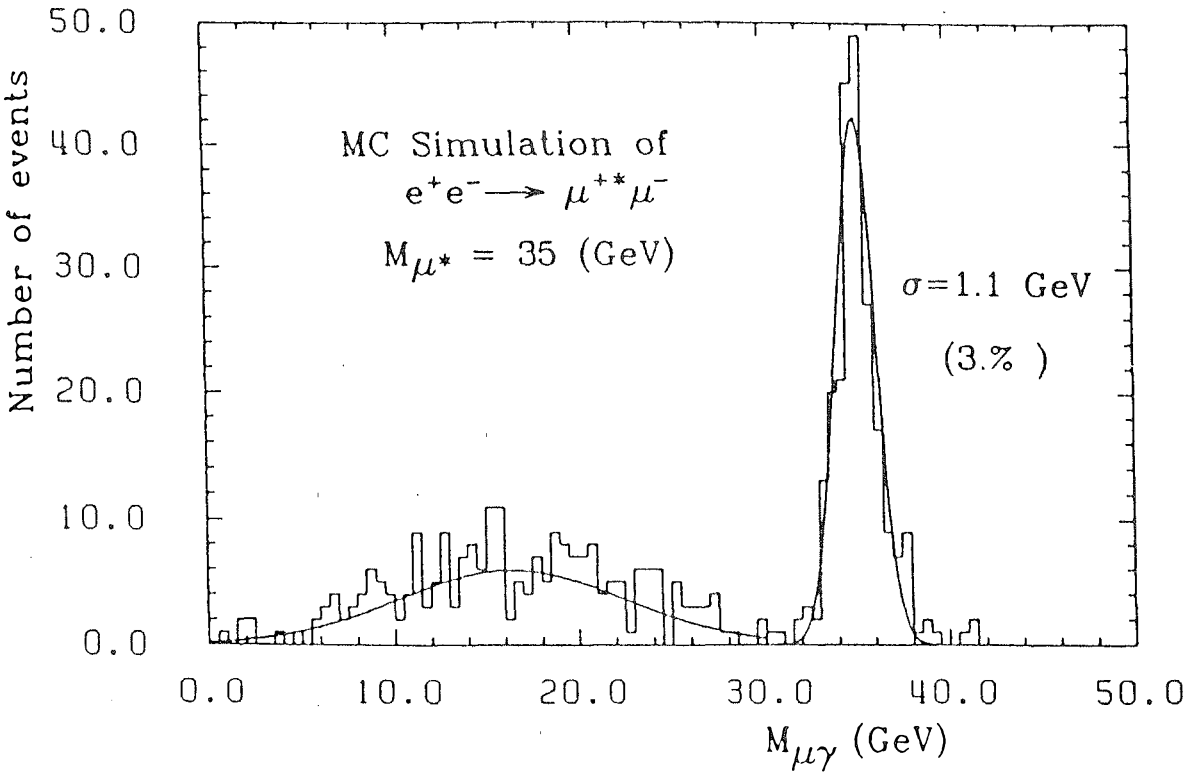

Figure 6.3 MC simulation of detector response to $\mu\mu^*$ production

response to the production of single μ^*'s. A search for such an excess can be made in $\mu^+\mu^-\gamma$ events after the subtraction of the standard process.

In order to reduce the background from the standard process while keeping a large acceptance for the process to be searched, a $\mu\gamma$ opening angle cut is applied to the data and Monte Carlo,

$$\theta_{\mu\gamma} \geq 10.^\circ. \tag{6.8}$$

With the above cut, the τ background is estimated again and found to increase to about 1.5%. The $\mu\gamma$ invariant mass distribution of the data is first compared to that of the Monte Carlo prediction of the electroweak theory (Fig 6.4) with only the high energy data. They agree well within statistics.

The invariant mass distribution of the single μ^* production is superimposed on the Monte Carlo prediction of the electroweak theory, and the 95% confidence level

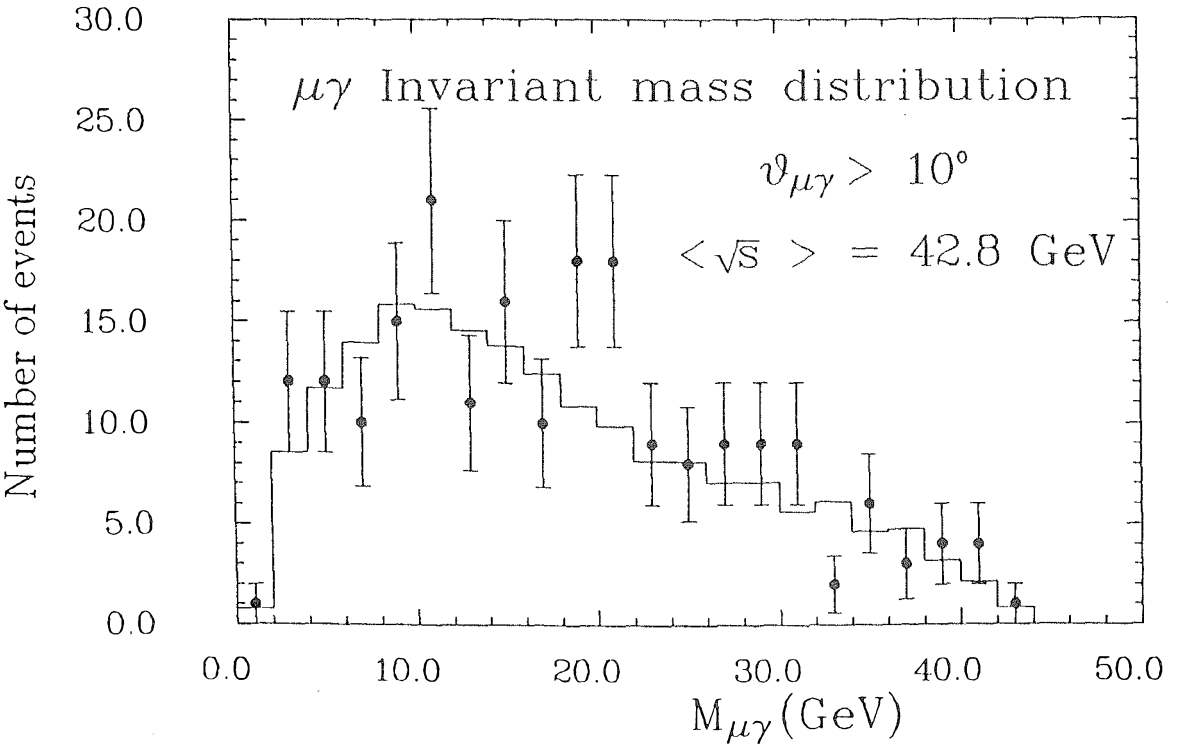

Figure 6.4 $\mu\gamma$ **invariant mass distribution of** $\mu^+\mu^-\gamma$ **events**

upper limit on the production cross section is obtained by applying the χ^2 test,

$$\chi^2 = \left(\frac{F-1}{\sigma_L}\right)^2 + \sum_i \left(\frac{N^i_{data} - N^i_{EW} - N^i_{\mu\mu^*}}{\sigma^i}\right)^2. \qquad (6.9)$$

where F and σ_L are the luminosity normalization factor and the luminosity error respectively.

Only the high energy data are used in the search for μ^* in the mass region of 30 – 42 GeV, while the 35 GeV data are also used in search for μ^* in the mass region of 23 – 30 GeV. The limits on the production cross section are converted to the limits on the coupling λ^2 at different masses. Fig 6.5 shows the limits obtained with our data.

It has been reported [49] that there might be an excess of events in the high $\mu\gamma$ invariant mass region, which may be seen in the $\mu^+\mu^-\gamma$ Dalitz plot (scatter plot of $(M^2_{\mu\gamma})_{low}$ *vs.* $(M^2_{\mu\gamma})_{high}$). Our data do not show any significant deviation from the electroweak expectation. Table 6.1 shows the Dalitz plot population in three

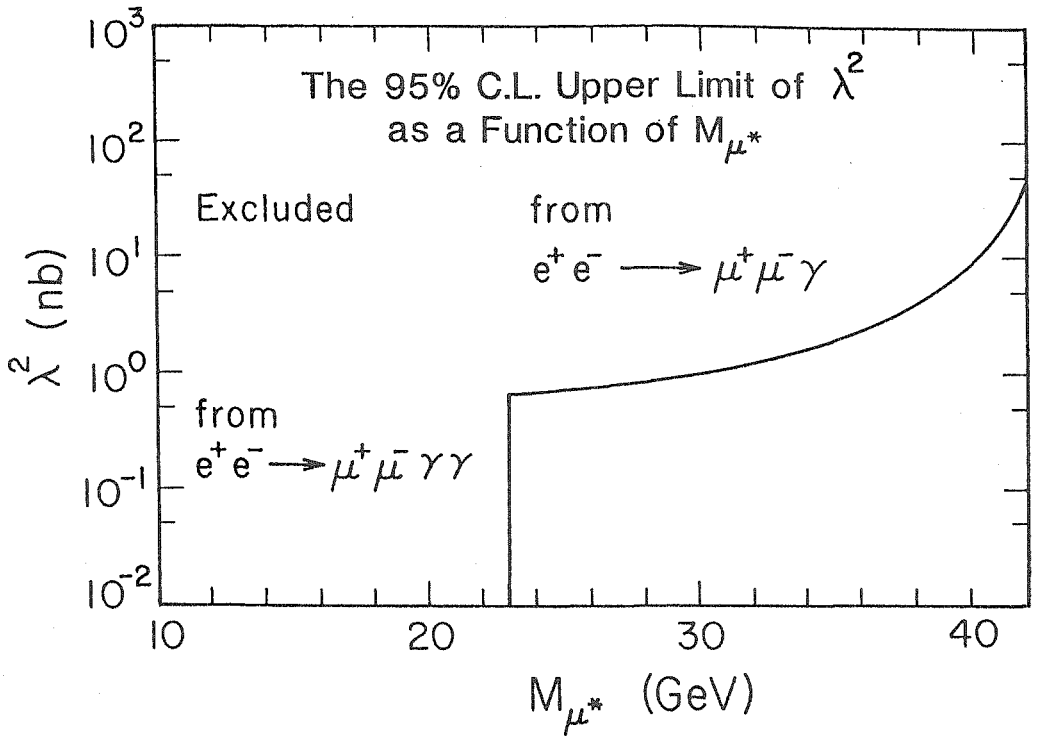

Figure 6.5 95% C.L. lower limit on μ^* mass and coupling.

regions, and Fig 6.6 is the Dalitz plot of all $\mu^+\mu^-\gamma$ events.

No experimental evidence for μ^* productions has been observed, and improved limits on the excited muon mass and coupling have been obtained.

6.3 Comparison with limits from g-2 experiments

According to QED, quantum fluctuations in the field associated with the emission and absorption of virtual photons and the polarizaton of the vacuum by these photons into virtual particle-antiparticle pairs give rise to the deviation of the gyromagnetic ratio (g-factor) of spin half particles from 2. In order to compete with the experimental accuracy of (g-2), the QED corrections up to 8th order as well as hadronic and weak contributions have to be taken into account. The (g-2) experiments not only give a strict test of QED to a high order, but also constrain many

$\sqrt{s}$ (GeV)	Region I	Region II	Region III
34.7 DATA	113	131	9
MC	136.5	104	15.3
42.8 DATA	50	44	10
MC	47.7	40.0	6.4

Region I: $(M^2_{\mu\gamma})_{high} + (M^2_{\mu\gamma})_{low} \leq .4s$
Region III: $(M^2_{\mu\gamma})_{high} \geq .8s$
Region II: the rest.

Table 6.1 Dalitz plot populations of $\mu^+\mu^-\gamma$ events.

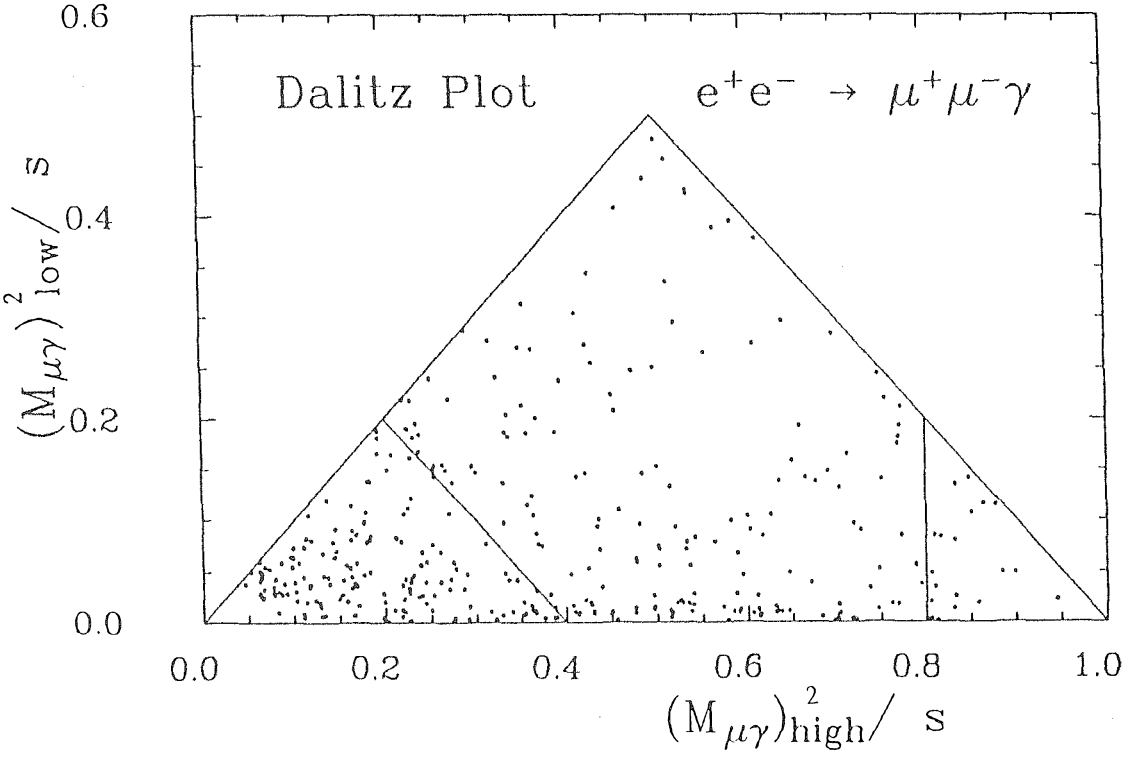

Figure 6.6 Dalitz plot of $\mu^+\mu^-\gamma$ events.

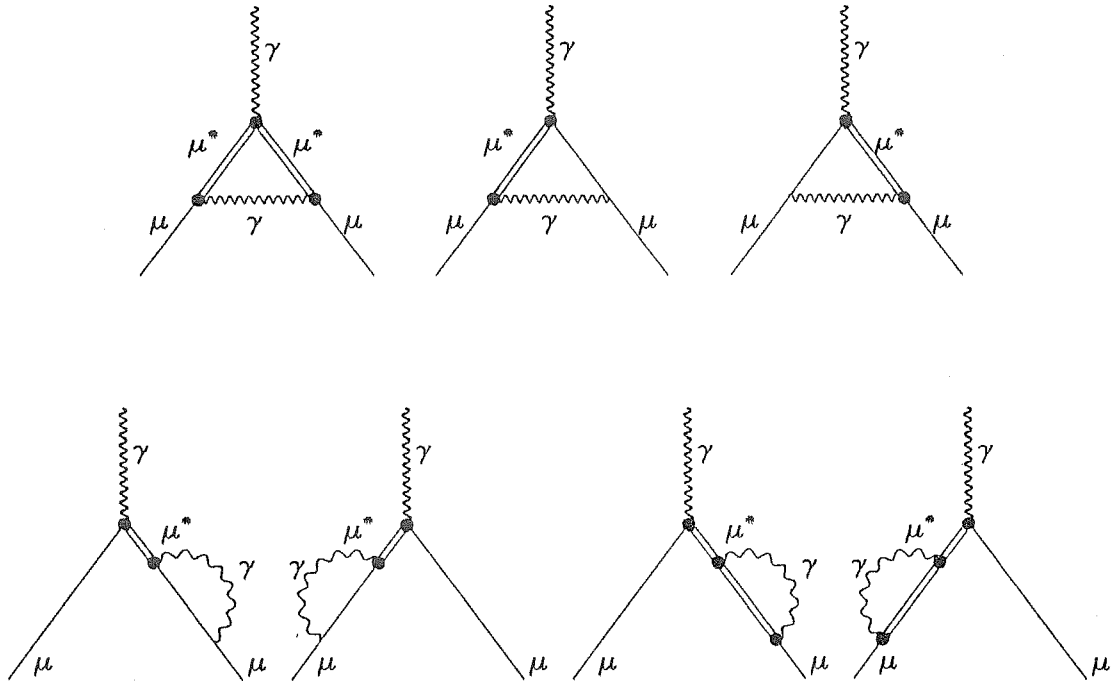

Figure 6.7 μ^* contribution to muon anomalous magnetic moment.

postulated processes that might contribute to the anomalous moment.

The excited lepton contribution to the anomalous magnetic moment has been studied and limits on the masses and couplings are obtained. Fig 6.7 contains the diagrams of μ^* corrections to the $\gamma\mu\mu$ vertex in the lowest order.

A more general Lagrangian is used in literature [50] for calculating the contributions,

$$L_{eff} = \frac{e}{2M_{\mu^*}} \left(\overline{\Psi}_{l^*} \sigma^{\mu\nu} (a - ib\gamma^5) \Psi_l F_{\mu\nu} + h.c. \right). \tag{6.10}$$

C invariance would require a and b to be real, CP invariance would require a to be real and b to be imaginary. a and b are dimensionless because of the factor $1/M_{\mu^*}$. In the limit of $M_{\mu^*} \gg m_\mu$, the anomalous magnetic moment due to μ^* can written as,

$$\chi = \frac{4\alpha}{\pi}(\mid a \mid^2 - \mid b \mid^2)\frac{m_\mu}{M_{\mu^*}} + \frac{9\alpha}{2\pi}(\mid a \mid^2 + \mid b \mid^2)\frac{m_\mu^2}{M_{\mu^*}^2}. \tag{6.11}$$

The CERN (g-2) experiments [51] gave the experimental value of the muon anomalous magnetic moment to an accuracy of 8.5×10^{-9}. The accuracy of the theoretical calculation is of the same order [52].

$$a_\mu^{exp} = (1165924.0 \pm 8.5) \times 10^{-9} \tag{6.12}$$

$$a_\mu^{th} = (1165920.2 \pm 2.0) \times 10^{-9} \tag{6.13}$$

At 95% confidence level, the difference between the theoretical prediction and the experimental measurement, δa_μ, is expected to be less than 21×10^{-9}.

If $\mid a \mid$ and $\mid b \mid$ are not equal or close to each other, the first term in Eq 6.11 dominates, hence,

$$\frac{(\mid a \mid^2 - \mid b \mid^2)}{(2M_{\mu^*})^2} \leq \frac{5.4 \times 10^{-6}}{M_{\mu^*}} (GeV)^{-1}. \tag{6.14}$$

If $\mid a \mid$ and $\mid b \mid$ are equal, the first term in Eq 6.11 vanishes and the second term becomes non-negligible,

$$\frac{(\mid a \mid^2 + \mid b \mid^2)}{(2M_{\mu^*})^2} \leq 4.5 \times 10^{-5} (GeV)^{-2}. \tag{6.15}$$

Our definition of the coupling constant λ in Eq 6.10 is approximately equivalent to

$$\lambda^2 \simeq \frac{(\mid a \mid^2 + \mid b \mid^2)}{(2M_{\mu^*})^2}. \tag{6.16}$$

At $M_{\mu^*} = 35$GeV, $\lambda^2 \geq 0.060nb$ is excluded by the (g-2) measurement at order m_μ/M_{μ^*}, and $\lambda^2 \geq 17.5nb$ is excluded at order $(m_\mu/M_{\mu^*})^2$.

The (g-2) measurements have given stringent limits on the excited muon mass and its coupling only when $\mid a \mid$ and $\mid b \mid$ are quite different from each other. The $\mu^*\mu$ production from e^+e^- , however, is almost independent of the choice of the couplings of the effective Lagrangian. $\mid a \mid$ and $\mid b \mid$ contribute to the total production of μ^* equally. Only the angular distribution of the μ^* decay is modified slightly. Similar limits would be obtained with different $\mid a \mid$ and $\mid b \mid$ values in our analysis, because the acceptance of the events is not affected dramatically.

Chapter 7

Conclusions and comparisons with other experiments

7.1 Measurements of the electroweak parameters

Electroweak effects in e^+e^- collision have been intensively studied by all the participating experiments at PETRA and PEP, as well as in ν–e, deep inelastic ν–nucleon and e–p scattering by other experiments. The most accurate measurements of electroweak effects in e^+e^- collisions are the charge asymmetry of muon pairs, which are summarized in Table 7.1 (our results have been presented already in Table 4.4) and Fig 7.1.

The measurements confirm the success of the standard model, up to momentum transfers in the interaction as high as 46 GeV. Using the measured mass of the weak neutral boson, the weak mixing angle as well as the weak neutral coupling constants are fitted with the data collected by the experiments. Table 7.2 shows the results with only the statistical errors included.

Although a satisfactory statistically combined fit of all the data may not be possible, an overall average can be estimated. Ignoring the systematic errors and averaging the asymmetric errors, the average values weighted by the statistical errors

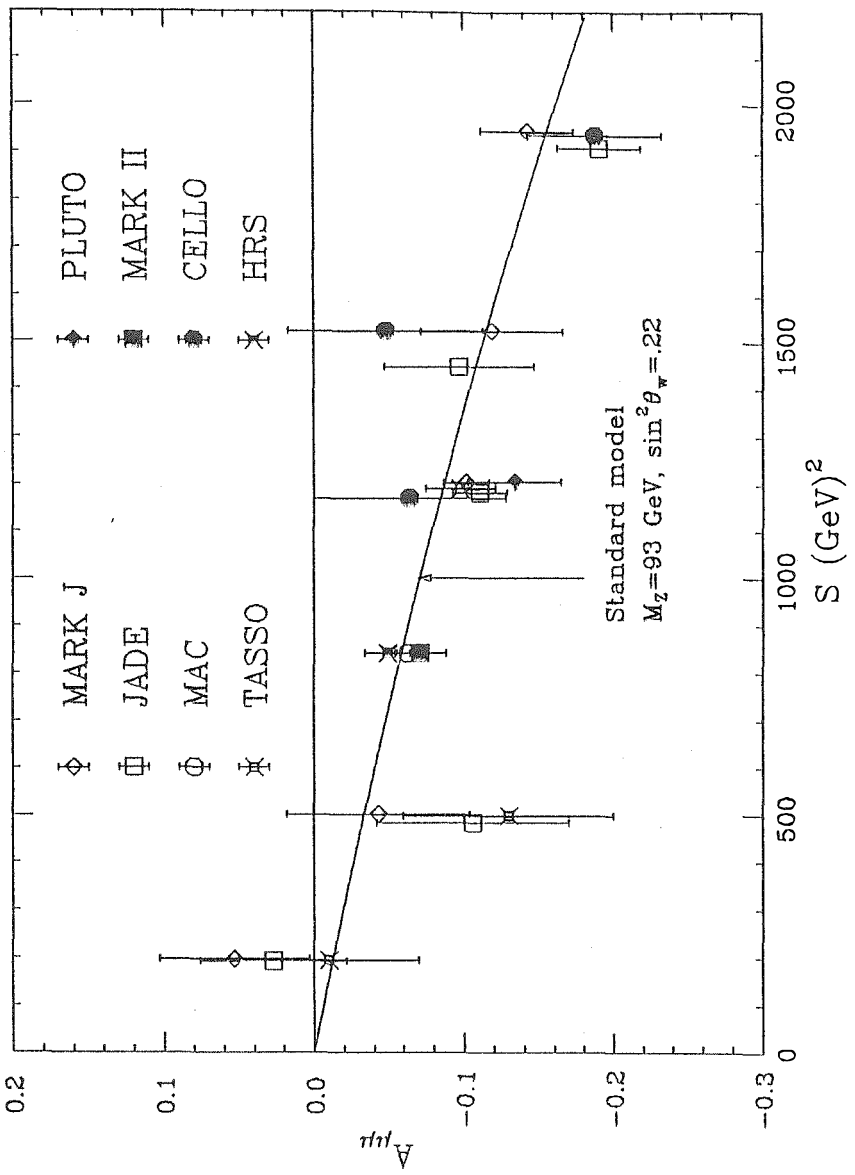

Figure 7.1 Muon charge asymmetry measured by the PETRA and PEP experiments.

Experiment	$\sqrt{s}$ (GeV)	$\int Ldt\ (pb)^{-1}$	Events	$A_{\mu\mu}^{exp}$ (%)	$A_{\mu\mu}^{th}$ (%)[1]
CELLO [53,54]	34.2	11.16	387	-6.4±6.4	-9.1
	39.0		288	-4.8±6.5 ± 1.0	-11.5
	44.0		611	-18.8±4.5 ± 1.0	-15.5
JADE [55]	13.9	1.6	458	+2.7 ±4.9	-1.2
	22.0	2.4	264	-10.6 ±6.4	-3.2
	34.4	71.2	3400	-11.1 ±1.8 ± 1.0	-8.6
	38.0	11.9	422	-9.7±5.0 ± 1.0	-11.1
	43.7	43.1	1258	-19.1±2.8 ± 1.0	-15.6
PLUTO [56]	34.7	45.95	1553	-13.4±3.1± < 1.0	-9.5
TASSO [57,58]	13.9	1.72	341	-1.0±6.0	-1.3
	22.3	3.2	268	-13.0±7.0	-3.6
	34.5	74.7	2673	-9.8±2.3 ± .5	-9.3
HRS [59]	29.0	106	5057	-4.9 ±1.5 ± .5	-5.9
MAC [60]	29.0	222	16058	-6.3±.8 ± .2	-6.3
MARK II [61]	29.0	100	5312	-7.1± 1.7	-5.7

Table 7.1 Muon charge asymmetry from other experiments.

are obtained, and the combined error is estimated by χ^2 method. The results are:

$$\sin^2\theta_w = 0.192 \pm 0.016 \tag{7.1}$$

$$g_A^2 = 0.260 \pm 0.017 \qquad g_V^2 = 0.015 \pm 0.017 \tag{7.2}$$

Another plausible way to combine these results is to fit the parameters using the asymmetry and R-value measurements from all the experiments. The normalization errors due to luminosity measurements are taken into account separately (one F

[1]These are the values quoted by the experimental collaborations and maybe not consistent among each other due to the fact that different nominal values for electroweak parameters are used.

Experiment	$\sin^2\theta_w$	g_A^2	g_V^2
CELLO [54]	0.22±0.04		
JADE [62]	$0.16^{+0.03}_{-0.02}$	0.308±0.075	0.13 ±0.18
PLUTO [56]		0.38 ±0.08	0.07 ±0.10
MARK J	$0.20^{+0.04}_{-0.025}$	0.265±0.032	0.038±0.043
TASSO [58]	0.26±0.10	0.27±0.06	-0.01±0.09
HRS [59]	$0.29^{+0.21}_{-0.09}$	0.208±0.064	0.027 ±0.051
MAC [60]	$0.22^{+0.05}_{-0.04}$	0.25±0.03	-0.02±0.03
MARK II [61][2]	0.11 ~ 0.35	0.23±0.05	0.03±0.03

Table 7.2 Measurements of electroweak parameters from e^+e^- experiments.

factor for each experiment). For $M_Z = 93$ GeV, the fit yields a measure of $\sin^2\theta_w = 0.20 \pm 0.015$.

These values are to be compared with the ones measured by the experiments in the other electroweak interactions presented in Table 7.3. It is crucial for the standard model to be acceptable, that these parameters are consistent among the experiments where interactions may involve different particles and/or with a large range of Q^2 from 10^{-12} GeV^2 in the atomic parity violation experiments to 10^4 GeV^2 in $\bar{p}p$ collision experiments. Fig 7.2 shows the allowed regions by various experiments in the $g_A - g_V$ plane. Although each individual experiment can not uniquely determine both coupling constants simultaneously, there is only one region that is allowed by all the experiments.

As the precision of the experiments improves, the measured value is sensitive to the electroweak radiative corrections that are applied to the data. It is necessary that a conventional renormalization scheme is recognized by the experimentalists

[2]This is from a fit of e^+e^- , $\mu^+\mu^-$ and $\tau^+\tau^-$ data

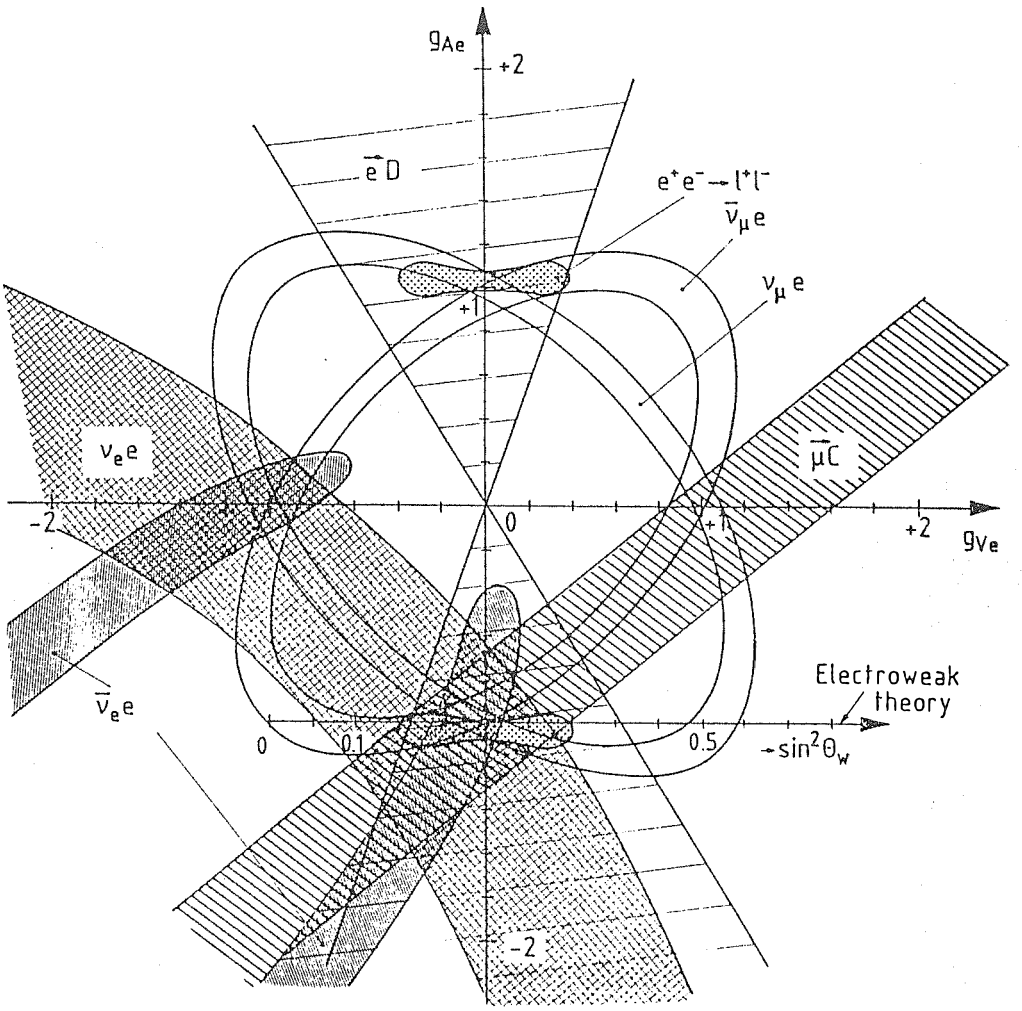

Figure 7.2 Allowed domains on the g_A–g_V plane, from νe, $e\uparrow D$, $\mu\uparrow C$, e^+e^- experiments. e–μ universality is assumed.

Interaction	Experiment	$\sin^2\theta_w$	comments
e↑D	SLAC[26]	0.224 ±0.020	
$\nu_\mu e$, $\bar{\nu}_\mu e$	BNL [21]	0.209±0.029±0.013	no rad. corr.
	CHARM[22]	0.215±0.032±0.012	
$\nu_\mu p$, $\bar{\nu}_\mu p$	BNL[63]	$0.220\pm0.016\ ^{+0.023}_{-0.031}$	no rad. corr.
$\nu_\mu N$, $\bar{\nu}_\mu N$	CCFRR[17]	0.242±0.011±0.005	
	CDHS[19]	0.227±0.005±0.003	
	CHARM[18]	0.236±0.005±0.003	
$\bar{p}p$	UA1[16]	0.214±0.006±0.015	$\frac{\pi\alpha(1-\Delta r)^{-1/2}}{(\sqrt{2}G_F M_W^2)}$
		0.194±0.032	$1-(M_W/M_Z)^2$
	UA2[42]	0.232±0.003±0.008	$\frac{\pi\alpha(1-\Delta r)^{-1/2}}{(\sqrt{2}G_F M_W^2)}$
		0.232±0.025±0.010	$1-(M_W/M_Z)^2$
atomic P.V.	[64]	0.21±0.05	combined

Table 7.3 $\sin^2\theta_w$ measured in other electroweak interactions.

before any results from different experiments can be compared to each other. The majority of the experimental groups now use the on-shell model, which has been proven to be convenient. The weak mixing angle is then defined as in Eq 1.17. When $\sin^2\theta_w$ is calculated from the W mass and Fermi constant G_F(which is usually QED radiatively corrected), or from the ratio of the neutrino charge current cross section to the neutral current cross section, electroweak radiative corrections have to be applied. From Table 7.3, one can see that the experimental data seem to imply that the radiative corrections are necessary. At least, the results after the radiative corrections lead to a more consistent comparison among all the experiments. If radiative corrections are neglected, $\sin^2\theta_w$ from ν–N scattering experiments will be increased to about .238±.007 (CDHF results, CHARM experiment quoted a radia-

diative correction of $\Delta \sin^2\theta_w = -.009$), but $\sin^2\theta_w$ from the W mass and the Fermi constant calculation will be decreased to about .212±.007 (averaged UA1 and UA2 results).

See reference [65] by U. Amaldi *et al.*, for a review of the recent measurements of the electroweak parameters. A global fit to all the available data except the e^+e^- experiments yields

$$\sin^2\theta_w \equiv 1 - \frac{M_W^2}{M_Z^2} = .230 \pm .0048 \tag{7.3}$$

Although the best fit of $\sin^2\theta_w$ and M_Z from e^+e^- experiments seems to deviate from the measurements by the other experiments, the significance is a little exaggerated by the way it is presented. The χ^2 function is distributed in such a way that it is quite flat in the region shown in Fig 4.10. More important, it is non-quadratic in terms of $\sin^2\theta_w$ near the minimum. In fact, for the combined fit, letting $\sin^2\theta_w = .23$ and $M_Z = 93$ GeV increments χ^2 by 3.8 from the minimum. This is equivalent to the 85% confidence level.

Another way of testing the consistency is to fix all the parameters and evaluate the χ^2. For the combined PETRA-PEP data, if we use $M_Z = 93$ GeV and $\sin^2\theta_w = .23$, we obtain $\chi^2 = 43.6$ with 46 degrees of freedom. It can be translated into a probability of 57.3% for the χ^2 to be equal or greater than this value. For the MARK J data, $\chi^2 = 6.3$ with ten degrees of freedom. The probability of obtaining a χ^2 equal or greater than this value is 79%. Both are well within the acceptable range.

No evidence for any deviation from the standard model has been observed. Various constraints are derived from the data, limiting the composite and extended gauge models. Most of the e^+e^- experiments have reported the 95% confidence level lower limit on the cutoff parameter of the form factor of the order of 250 GeV. TASSO and PLUTO [58,56] have also derived the limits on Λ' of the composite

models [43] comparable to ours. [3]

Experiment	$\sqrt{s}$ (GeV)	$A_{\mu\mu}^{exp}$	$A_{\mu\mu}^{QED}$	$A_{\mu\mu}^{EW}$
JADE	34.2	-0.39±0.08	-0.34±0.01	-0.400±0.006
MAC	29.0	-0.216±0.041	-0.211±0.013	

Table 7.4 The muon charge asymmetry of $\mu^+\mu^-\gamma$ events by JADE and MAC.

7.2 Radiative muon pair production

Nearly 800 $\mu^+\mu^-\gamma$ events have been selected from MARK J data. Various properties of these events have been studied and found to be consistent with the prediction of the standard model. This verifies the validity of the standard model up to order α^3, and it gives constraints on the composite scale of the muons. The muon charge asymmetry of $\mu^+\mu^-\gamma$ events and its dependence on the photon energy shows the electroweak interference as well as the QED interference.

Studies of $\mu^+\mu^-\gamma$ events have also been reported by JADE, CELLO and MAC collaborations [66,49,67,68]. While the kinematic cuts may vary from experiment to experiment, the data are in good agreement with Monte Carlo simulation. The published results of the muon charge asymmetry by JADE and MAC are given in Table 7.4. The discrepancy among the experiments is due to the strong dependence of the asymmetry on the kinematic cuts which are different for each experiment.

Limits on the production rates of hypothetical excited muons have been obtained by the study of $\mu^+\mu^-\gamma$ and $\mu^+\mu^-\gamma\gamma$ events. There is no evidence of such production. All of the above mentioned experiments have reported the search for excited muons. Limits on the hypothetical coupling strength vs the μ^* mass are derived. The μ^*

[3] See Appendix C for comments on the Lagrangian used by some other groups

pair production is constrained by the study of the $\mu^+\mu^-\gamma\gamma$ events at PETRA up to 23 GeV. The MARK J data give the most stringent limit.

Chapter 8

Precision tests of electroweak theory at LEP

In the previous chapter, the present status of precision tests of the electroweak theory has been summarized. With the new experiments at LEP (Large Electron-Positron Collider at CERN) and SLC (SLAC Linear Collider) in the near future, these values will be brought to a higher level of accuracy.

To complete the picture of the standard model, one would expect to see the Higgs particle as well as the top quark experimentally. Furthermore, the unique three gauge boson couplings such as $Z^0W^+W^-$ or γW^+W^- are of great interest. Observations of the direct production of top quarks and Higgs particles as well as other new particles are among the primary goals of the future collider experiments. However, with the advantage of high luminosity, large cross sections at the Z° pole and high precision detectors such as L3, even if the direct productions of these new particles are beyond the energy that can be reached, precision measurements of the production of the known particles such as $e^+e^- \rightarrow \mu^+\mu^-(\gamma)$ will reveal or at least constrain the new physics through its contributions to virtual processes.

The most important parameters that are going to be measured at the upcoming e^+e^- colliders around 100 GeV are the Z° mass and its width. The will be done by reconstructing the line shape of Z° resonance in the channels such as $e^+e^- \rightarrow$

$\mu^+\mu^- X$. With an average luminosity of L = $10^{31} cm^{-2} s^{-1}$ during running at LEP, two days running at each of 13 energies above and below the resonance in 2 GeV steps will give statistical errors of the mass and the width as,

$$\Delta M_Z \leq \pm 10 MeV, \tag{8.1}$$

$$\Delta \Gamma_{tot} \leq \pm 15 MeV. \tag{8.2}$$

The systematic errors will have to be understood to the same order.

When LEP II reaches the energy for W pair production, the measurement of its cross section will provide a test of the gauge cancellations expected in the standard model. Three gauge boson vertices can be studied. The W mass is expected to be determined to an accuracy of 100 MeV.

With the well determined Z° and W masses, ($\delta(M_W/M_Z) \simeq \pm 1.2 \times 10^{-3}$.), many other tests of the standard model can be performed. Using Eq 1.17, one finds that $\sin^2\theta_w$ can be determined to about 1%,

$$\delta(\sin^2 \theta_w) \simeq \pm 0.0024. \tag{8.3}$$

Eq 1.18 can be rewritten as

$$1 - \Delta r = \frac{\pi \alpha}{\sqrt{2} G_F M_W^2 (1 - M_W^2/M_Z^2)}, \tag{8.4}$$

giving

$$\delta(\Delta r) \simeq 6 \times 10^{-3}. \tag{8.5}$$

While Δr is mainly due to the QED running coupling constant, it also has the contributions from top quark and Higgs boson. Fig 8.1 shows the relation between $\sin^2\theta_w$ and M_Z with various top and Higgs masses. Therefore, a precise determination of Δr gives constraints on the masses of these particles.

It has been proposed that after measuring the line shape of the Z° resonance, a large sample of data of, for example, 200 pb^{-1} will be collected with the center

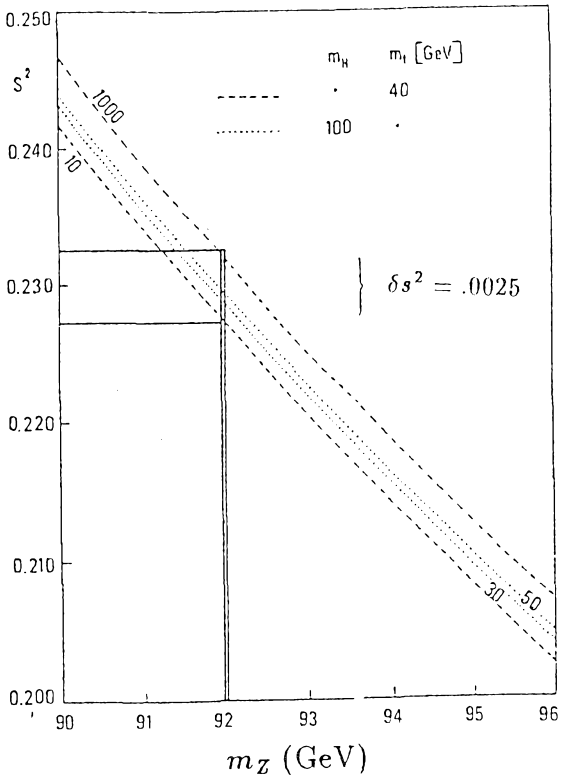

Figure 8.1 $s^2=\sin^2\theta_w$ **as a function of** M_Z **for different values of Higgs and top masses [1].**

of mass energy at the Z° resonance. Copious Z°'s will be produced, resulting in a sample of up to 2×10^5 muon pair events. Careful studies of these events will give a solid testing ground for the standard model. The forward-backward charge asymmetry, final state polarization asymmetry and left-right asymmetry are among the most sensitive quantities that can be measured. They are defined as,

$$A_{FB} = \frac{\sigma_F(f) - \sigma_F(\bar{f})}{\sigma_F(f) + \sigma_F(\bar{f})} \simeq 3\eta_f \frac{\eta_e + \frac{1}{2}P_e}{1 + 2P_e\eta_e}, \tag{8.6}$$

$$A_{LR} = \frac{\sigma(f_L) - \sigma(f_R)}{\sigma(f_L) + \sigma(f_R)} \simeq -2P_e\eta_e, \tag{8.7}$$

$$A_{pol} = \frac{\sigma_L - \sigma_R}{\sigma_L + \sigma_R} \simeq -2\eta_f, \tag{8.8}$$

where P_e is the e^- longitudinal polarization, f stands for the final state fermion, and η is defined as

$$\eta = \frac{g_V g_A}{g_V^2 + g_A^2}. \tag{8.9}$$

The sensitivity of these asymmetries to $\sin^2\theta_w$ is somewhat different. A_{FB} is the most straightforward to obtain, but the least sensitive without polarization, $\delta(\sin^2\theta_w) \simeq \mid \delta A_{FB} \mid /2$ for $\sin^2\theta_w = 0.23$. The polarization of the final state fermions can only be reconstructed for τ leptons through their decay. The most sensitive test is the polarized left-right asymmetry, which gives $\delta(\sin^2\theta_w) \simeq \mid \delta A_{LR} \mid /(8P_e)$, provided the polarized electron beam is available and the polarization is known to a better accuracy. With the polarized electron beam, the sensitivity of A_{FB} to $\sin^2\theta_w$ is greatly improved.

2×10^5 muon pair events collected at the Z° resonance will bring the statistical error of the forward-backward asymmetry down to $\delta A_{FB} \simeq 0.002$. It is therefore a challenge to reduce all possible systematic errors down to the same order.

Radiative corrections, especially due to the initial state radiation, play an important role in both the line shape of the resonance and the asymmetries. Detailed study of relevant processes, however, has shown that the corrections are understood down to a level where the Z° mass corresponding to a given $\sin^2\theta_w$ is determined to within ± 20 MeV. Achieving this theoretical precision, taking into account the experimental cuts and acceptance, will require detailed simulations and careful analysis.

Detector asymmetries, i.e., slightly different acceptance for negative and positive tracks, may result in systematic errors in the forward-backward asymmetry. The more sophisticated detectors at LEP, with their higher resolution and granularity, may do much better than the existing detectors at the present-day colliders. Furthermore, the large counting rates at the Z° peak would enable one to monitor such a bias to a high accuracy. It should be possible to control the systematic error of the charge asymmetry at LEP below the 0.2% level.

Fig 8.2 shows the forward-backward asymmetry at $\sqrt{s} = M_Z$ as a function of M_Z with its dependence on the top and Higgs masses with and without electron

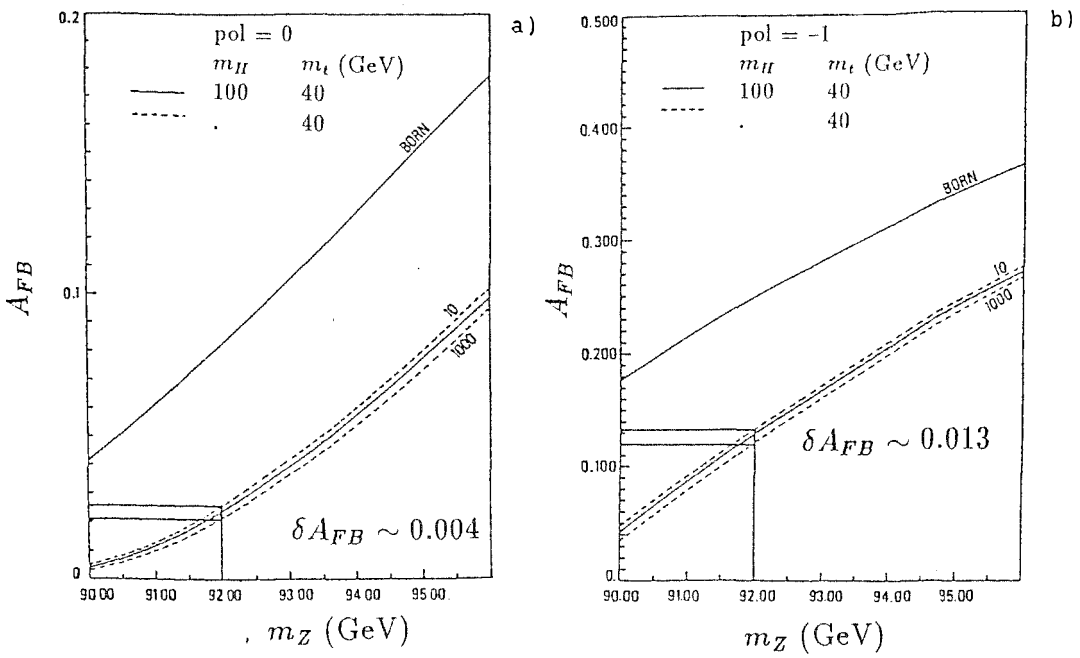

Figure 8.2 A_{FB} **as a function of** M_Z **for different values of Higgs and top masses without (a) and with (b) longitudinal polarization [1].**

beam polarization. With the error given above, this quantity will serve as a probe for what is beyond the center of mass energy available at LEP.

In conclusion, precision measurements of quantities at LEP, such as the gauge boson masses and various asymmetries, will confront the standard model with more stringent constraints and/or reveal new physics.

Appendix A

QED α^3 order corrections to muon pair production

In this appendix, explicit expressions for the radiative QED processes (Fig 2.3a,b) are given. Both the soft and hard photon contributions are considered, as well as the vertex correction and the vacuum polarization of the photon. The formulae for the processes involving Z° exchange are more complicated, and can be found in reference [30].

The cross sections can be divided into two parts: the virtual and soft part, and the hard photon part. The first part includes corrections from processes with photon energies up to k_1. The infrared divergence is avoided by summing over the diagrams in Fig 2.3a and 2.3b. The second part gives the cross section with three particles in the final state.

The soft and virtual corrections to the muon pair production can be expressed as,

$$\frac{d\sigma}{d\Omega_\mu} = \frac{d\sigma_0}{d\Omega_\mu}(1 + 2\Pi + A) \qquad (A.1)$$

where the lowest order cross section is given by Eq 2.4, and Π is the order α vacuum polarization, and A is the order α vertex and soft radiation corrections, written as,

$$\begin{aligned} A &= (\beta_i + \beta_f + \beta_{int})\ln(\frac{k_1}{E}) + \frac{2\alpha}{\pi}\left\{\frac{3}{4}(\ln\frac{s}{m_e^2} + \ln\frac{s}{m_\mu^2}) + \frac{\pi^2}{3} - 2\right. \\ &\quad -\frac{2}{1+\cos^2\theta}\left[\cos\theta(\ln^2(\sin\frac{1}{2}\theta) + \ln^2(\cos\frac{1}{2}\theta))\right. \end{aligned}$$

with

$$A_i = -\frac{m_e^2}{2s'^2}\left[\frac{t^2+u^2}{(p_-\cdot k)^2}+\frac{t'^2+u'^2}{(p_+\cdot k)^2}\right]+\frac{t^2+t'^2+u^2+u'^2}{4s(p_+\cdot k)(p_-\cdot k)}, \tag{A.10}$$

$$A_f = -\frac{m_\mu^2}{2s^2}\left[\frac{t^2+u'^2}{(q_-\cdot k)^2}+\frac{t'^2+u^2}{(q_+\cdot k)^2}\right]+\frac{t^2+t'^2+u^2+u'^2}{4s'(q_+\cdot k)(q_-\cdot k)}, \tag{A.11}$$

$$A_{if} = +\frac{t^2+t'^2+u^2+u'^2}{4ss'}\left[-\frac{t}{(p_+\cdot k)(q_+\cdot k)}-\frac{t'}{(p_-\cdot k)(q_-\cdot k)}\right.$$
$$\left.+\frac{u'}{(p_-\cdot k)(q_+\cdot k)}+\frac{u}{(p_+\cdot k)(q_-\cdot k)}\right], \tag{A.12}$$

and

$$t=(p_+-q_+)^2, \qquad u'=(p_--q_+)^2, \qquad s=(p_++p_-)^2,$$
$$t'=(p_--q_-)^2, \qquad u=(p_+-q_-)^2, \qquad s'=(q_++q_-)^2.$$

p and q are the four momenta of the electrons and muons respectively.

A_i, A_f, A_{if} represent respectively the contributions from the initial state radiation, the final state radiation and the interference between them. Under the exchange of $\mu^- \leftrightarrow \mu^+$, the interference term changes sign and thus only contributes to the asymmetry but not to the total cross section.

After the integration over the phase space, the total cross section from $\mu^+\mu^-$ and $\mu^+\mu^-\gamma$ final states, including the contributions from vacuum polarization of τ lepton and quarks, can be written as:

$$\sigma_{tot} = \sigma_0(1+\delta_T) = \sigma_0(1+\delta_e^T+\delta_\mu^T+\delta_\tau+\delta_{had}), \tag{A.13}$$

where

$$\delta_e^T = \beta_i\left(\frac{1}{2}\ln\frac{s}{\mu^2}-\frac{1}{4}\right)+\frac{2\alpha}{\pi}\left(\frac{1}{6}\pi^2-\frac{17}{36}\right), \tag{A.14}$$

$$\delta_\mu^T = \frac{2\alpha}{\pi}\left(\frac{1}{3}\ln\frac{s}{\mu^2}-\frac{13}{72}\right), \tag{A.15}$$

and δ_τ (δ_{had}) is the contributions from the τ(quark) vacuum polarization.

At $\sqrt{s}=44$ GeV, the corrections are

$$\delta_e^T = 58.9\%, \qquad \delta_\mu^T = 1.8\%, \tag{A.16}$$

$$\delta_\tau = .73\%, \qquad \delta_{had} = 5.6\%, \tag{A.17}$$

$$\sigma_{tot} = \sigma_0 \cdot 1.67, \tag{A.18}$$

where $m_\tau = 1.78$ GeV is used. δ_{had} is obtained by integrating over the total e^+e^- hadronic cross section numerically.

It is worth noting that at $\sqrt{s} = 44$ GeV, the total vacuum polarization contribution to the total cross section amounts to 11%. Since the total correction within our acceptance is about 5% (see Fig 2.4), the vertex and soft photon corrections to the total cross section under our kinematic cuts are negative and about -6%.

Appendix B

Estimation of high order corrections to $\mu^+\mu^-$ and $\mu^+\mu^-\gamma$ production

The exact calculation of the corrections to all orders to the lowest cross sections is not achievable in practice. However, renormalization group techniques may be used to give the QED estimates of the higher order QED corrections. This improves the accuracy of the theoretical accuracy.

It has been proposed [36] the corrections can be approximated by exponentiation:

$$\frac{d\sigma}{d\Omega_\mu} = \frac{d\sigma_0}{d\Omega_\mu}\left(\frac{1}{1-\Pi}\right)^{2+(A/\Pi)}, \tag{B.1}$$

where A and Π are defined in the Appendix A.

Based on the above formula, the QED asymmetry of muon pairs can be easily evaluated,

$$\begin{aligned} A_{\mu\mu}^{QED}(\theta) &= \frac{\frac{d\sigma(\theta)}{d\Omega} - \frac{d\sigma(\pi-\theta)}{d\Omega}}{\frac{d\sigma(\theta)}{d\Omega} + \frac{d\sigma(\pi-\theta)}{d\Omega}} = \frac{(1-\Pi)^{-A_a/\Pi} - (1-\Pi)^{+A_a/\Pi}}{(1-\Pi)^{-A_a/\Pi} + (1-\Pi)^{+A_a/\Pi}} \\ &\approx A_a(1+\frac{1}{2}\Pi), \end{aligned} \tag{B.2}$$

where A_a stands for the antisymmetric part of A. The higher order corrections can therefore be recognized as $A_a\Pi/2$. At the center of mass energy of 35 GeV,

$$\frac{\Pi}{2} = 0.025, \tag{B.3}$$

namely, the higher order QED correction to the asymmetry is about 2.5% of the α^3 QED correction, which is quite negligible.

Similar arguments can be given to $\mu^+\mu^-\gamma$ events. However, the correction now may depend on the cuts, such as photon energy requirement. The $\mu^+\mu^-\gamma$ cross section of (A.9) has to be modified by multiplying A_i, A_f, A_{if} by $F(s)$, $F(s')$, $|F(s)F(s')|^{1/2}$, where $F(s)$ is defined as

$$F(s) = |1 - \Pi(s)|^{-2-A(s)/\pi(s)} \tag{B.4}$$

According to our selection cuts, a conservative estimate of the correction to the cross section is about $\pm 3\%$, and that to the charge asymmetry in the acceptance is less than $+1.5\%$.

These estimations should be considered as the upper limits of what might actually contribute to the processes.

Appendix C

Extended gauge models of the electroweak interaction and the composite structure of leptons

Possible composite structure of the fermions has been explored, which gives some low energy implications. As no significant deviation from the standard model has been seen in the data, the composite energy scale Λ must be much higher than the present available momentum transfer.

One of the tests of the compositeness is proposed by E. J. Eichten *et al* [43]. In addition to the standard electroweak interaction, the composite fermions possess a new four fermion contact interaction with a coupling strength g^2/Λ'^2. For muon pair production from e^+e^- annihilation, the assumption has to be made that e and μ have some common constituents. Therefore it is less general than the tests with Bhabha scattering data. The limits obtained from muon pair production are somewhat higher than the Bhabha scattering data.

The effective Lagrangian is given in Eq 4.13. Taking into account all the interactions and their interference, the total cross section of Bhabha scattering can be written as

$$\frac{d\sigma}{d\Omega} = \frac{\alpha^2}{4s} \cdot \frac{1}{2}[C_0 + C_1(1-\cos\theta)^2 + C_2(1+\cos\theta)^2], \qquad \text{(C.1)}$$

with (C.2)

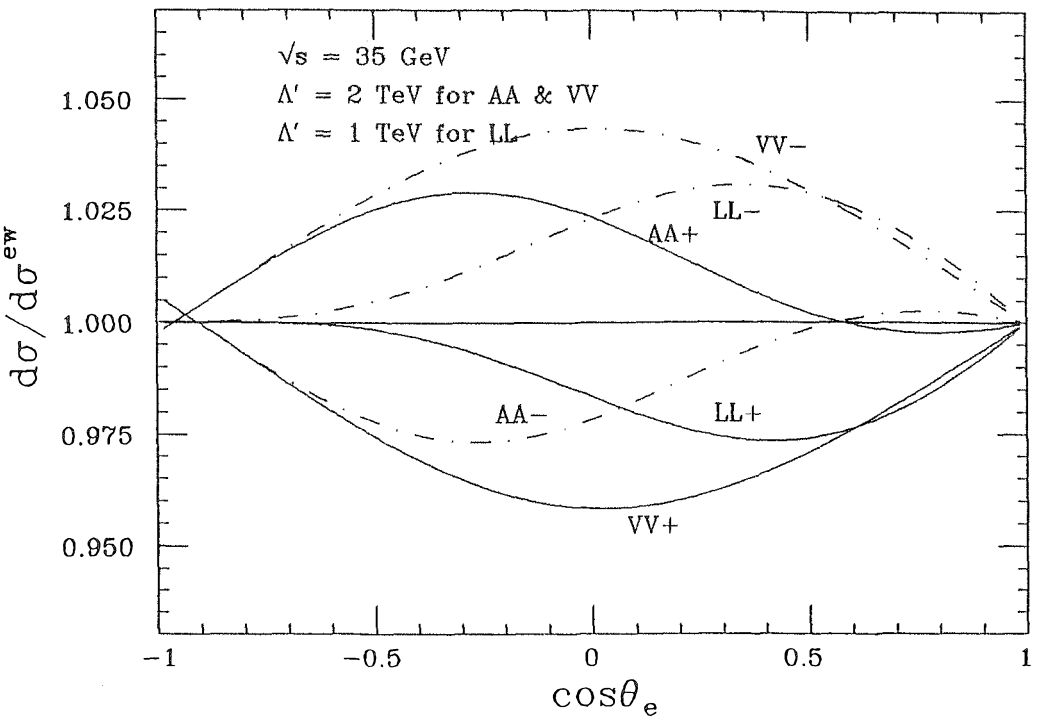

Figure C.1 The ratio of the Bhabha scattering cross section of the composite model to that of the standard model prediction.

$$C_0 = (\frac{s}{t})^2 \mid 1 + (g_V^2 - g_A^2)\frac{t}{t_z} + \frac{\eta_{RL} t}{\alpha\Lambda^2} \mid^2, \tag{C.3}$$

$$C_1 = \mid 1 + (g_V^2 - g_A^2)\frac{s}{s_z} \pm \frac{\eta_{RL} s}{\alpha\Lambda_\pm'^2} \mid^2, \tag{C.4}$$

$$\begin{aligned} C_2 = {} & \frac{1}{2} \mid 1 + \frac{s}{t} + (g_V + g_A)^2 \left(\frac{s}{s_z} + \frac{s}{t_z}\right) \pm \frac{2\eta_{RR} s}{\alpha\Lambda_\pm'^2} \mid^2 \\ & \frac{1}{2} \mid 1 + \frac{s}{t} + (g_V - g_A)^2 \left(\frac{s}{s_z} + \frac{s}{t_z}\right) \pm \frac{2\eta_{LL} s}{\alpha\Lambda_\pm'^2} \mid^2, \end{aligned} \tag{C.5}$$

$$t = -s(1 - \cos\theta)/2,$$

$$s_z = \frac{1}{4\sin^2\theta_w \cos^2\theta_w} \cdot \frac{1}{s - M_Z^2 + iM_Z\Gamma_Z},$$

$$t_z = \frac{1}{4\sin^2\theta_w \cos^2\theta_w} \cdot \frac{1}{t - M_Z^2 + iM_Z\Gamma_Z}.$$

For $\mu^+\mu^-$ final states, the cross section is obtained from the above equations by setting all the terms containing t and t_z to zero and replacing the factor of 2 in front of η_{RR} and η_{LL} by one. As it has been pointed out by B. Schrempp *et al.* [70], in

some analyses of the PETRA and PEP data, this factor of 2 has not been properly taken into account. Corrections have to be made when comparing these results with each other.

A useful way of measuring the substructure is to plot the relative deviation of the cross section from the standard model prediction,

$$\frac{d\sigma^{tot}/d\Omega}{d\sigma^{ew}/d\Omega}. \tag{C.6}$$

Fig C.1 is the angular distributions of the ratios of the cross sections at $\sqrt{s} = 35$ GeV, with $\Lambda' = 2$ TeV for AA and VV coupling and $\Lambda' = 1$ TeV for LL coupling (see Table 4.5 for the definition of the couplings). Unlike the effect of the contact interactions on the muon pair production (see Fig 4.13), the relative deviation of the Bhabha cross section in the forward and backward regions is suppressed. At $\cos\theta_e \rightarrow 1$, the QED t-channel photon exchange dominates, so that weak and contact interaction contributions can be neglected. At $\cos\theta_e \rightarrow -1$, it is the approximate cancellation between the s-channel and the t-channel contributions that reduces the effect substantially.

From the Bhabha data at PEP and PETRA, lower limits of Λ's around 1 - 2 TeV have been derived [56,58].

The R-value and charge asymmetry of muon pair production is then modified as

$$R = \frac{1}{2}(C_2 + C_1), \tag{C.7}$$

$$A_{\mu\mu} = \frac{3}{4} \cdot \frac{C_2 - C_1}{C_2 + C_1}. \tag{C.8}$$

Neglecting the weak contribution, the correction to the total cross section can be written as a form factor. By definition, $\Lambda'_{\pm}$ differs from $\Lambda_{\pm}$ (as defined in Eq 4.8) by approximately a factor of $1/\sqrt{\alpha}$,

$$\Lambda'_{\pm} \sim \frac{1}{\sqrt{\alpha}}\Lambda_{\pm}. \tag{C.9}$$

Extended gauge models, in the general class governed by the group structure SU(2)⊗U(1)⊗G, where G is the additional group, can be constructed such that they are consistent with the existing experimental data at present energy with, however, some new phenomena predicted at higher momentum transfer [46]. One of the common implications of the models is the existence of extra neutral gauge bosons. This can be revealed in the experiments through contributions from additional neutral currents, including the the possible mixing between the standard and "new" weak eigenstates. The Lagrangian of this class of gauge theories is given in Ref [45] as,

$$L_{NC} = e j_\mu^{em} A^\mu + \sum_{j=1}^{N} f_j \left[j_\mu^{(3)} + \left(\frac{M_W^2}{m_j^2} - 1 \right) j_\mu^{em} \right] Z_j^\mu \qquad \text{(C.10)}$$

where f_j is a constant depending on the masses and the coupling in the models. Although the deviation depends on the specific models, they all have a common feature that when the momentum transfer is much less than the mass of the neutral bosons, an effective four fermion coupling exists,

$$H_{eff}(q^2 \to 0) = -\frac{e^2}{2q^2} j_\mu^{em} j_{em}^\mu + \frac{4G_F}{\sqrt{2}} \left[(j_\mu^{(3)} - \sin^2\theta_w j_2^{em})^2 + C(G) j_\mu^{em} j_{em}^\mu \right] \qquad \text{(C.11)}$$

The coefficient $C(G)$ is thus a measure of the deviation from the standard model due to extended gauge models.

Comparing this effective Hamiltonian with the above composite Lagrangian, we can easily get the 95% confidence level limit using the VV coupling,

$$C < \frac{\pi}{\sqrt{2} G_F \Lambda_+'^2 (VV)} \qquad \text{(C.12)}$$

For a specific model with a known structure of the interactions, the cross section of various processes can be calculated. To give an example, if there exists a second Z° and the couplings and the mass are given, the neutral current part of the Lagrangian can be written as,

$$L = -i(e A_\mu J_{em}^\mu + g_Z Z_\mu J_Z^\mu + g_{Z'} Z_\mu' J_{Z'}^\mu) \qquad \text{(C.13)}$$

where J^{μ}_{em} and J^{μ}_{Z} are the normal electromagnetic and the weak neutral currents, and $J^{\mu}_{Z'}$ is the current of the second neutral boson.

$$g_Z J^{\mu}_Z = g_Z(\bar{\Psi}_L L\gamma^{\mu}\Psi_L + \bar{\Psi}_R R\gamma^{\mu}\Psi_R) \tag{C.14}$$

$$= e\Psi\gamma^{\mu}(v - a\gamma^5)\Psi, \tag{C.15}$$

$$g_{Z'} J^{\mu}_{Z'} = g_{Z'}(\bar{\Psi}_L L'\gamma^{\mu}\Psi_L + \bar{\Psi}_R R'\gamma^{\mu}\Psi_R) \tag{C.16}$$

$$= e\Psi\gamma^{\mu}(v' - a'\gamma^5)\Psi. \tag{C.17}$$

Taking into account the Z-Z' mixing, the mass eigenstates of the normal neutral bosons and their couplings can be expressed as,

$$Z_1 = Z\cos\theta + Z'\sin\theta, \tag{C.18}$$

$$Z_2 = -Z\sin\theta + Z'\cos\theta, \tag{C.19}$$

$$a_1 = a\cos\theta + a'\sin\theta, \tag{C.20}$$

$$a_2 = -a\sin\theta + a'\cos\theta, \tag{C.21}$$

$$v_1 = v\cos\theta + v'\sin\theta, \tag{C.22}$$

$$v_2 = -v\sin\theta + v'\cos\theta. \tag{C.23}$$

The couplings of the standard Z° are,

$$a = -\frac{1}{2\sin 2\theta_w}, \quad v = \frac{4\sin^2\theta_w - 1}{2\sin 2\theta_w}. \tag{C.24}$$

The R-value and asymmetry of muon pairs should therefore be modified as,

$$R_{\mu\mu} = 1 + \sum_{i=1}^{2}\left(2v_i^2\frac{s}{s - M_i^2} + (a_i^2 + v_i^2)^2\left(\frac{s}{s - M_i^2}\right)^2\right) + 2(a_1a_2 + v_1v_2)^2\frac{s^2}{(s - M_1^2)(s - M_2^2)}, \tag{C.25}$$

$$A_{\mu\mu} = \frac{3}{2R_{\mu\mu}}\sum_{i=1}^{2}\left(2a_i^2\frac{s}{s - M_i^2} + 2v_i^2a_i^2\left(\frac{s}{s - M_i^2}\right)^2\right) + (a_1v_2 + a_2v_1)^2\frac{s^2}{(s - M_1^2)(s - M_2^2)}. \tag{C.26}$$

With the above formula, limits on the mass of the second Z° and mixing angle can be obtained from the experimental data.

Appendix D

Notes on statistics

Many statistical methods have been applied in this study. Based upon the experimental measurements, two kinds of results have been presented in the thesis: the determination of certain parameters of the accepted theory, and the test of some hypotheses or proposed theories with limits on their parameters at a given confidence level.

D.1 Maximum likelihood method

The maximum likelihood method is a very powerful tool in determining the unknown parameters of a given distribution. In general, a normalized distribution can be written as

$$y = f(\mathrm{x},,\mathrm{p}), \tag{D.1}$$

where x is a set of variables and p a set of parameters. For a measured event sample, the maximum likelihood function is then defined as

$$\mathcal{L}(\mathrm{p}) = \prod_{i=1}^{n} f(\mathrm{x}_i, \mathrm{p}). \tag{D.2}$$

$\mathcal{L}$ is the joint probability density for obtaining this set of measurements. By maximizing this probability with respect to the parameters, the best estimates of the parameters are obtained.

$$\frac{\partial \mathcal{L}(,\mathrm{p})}{\partial \mathrm{p}} = 0. \tag{D.3}$$

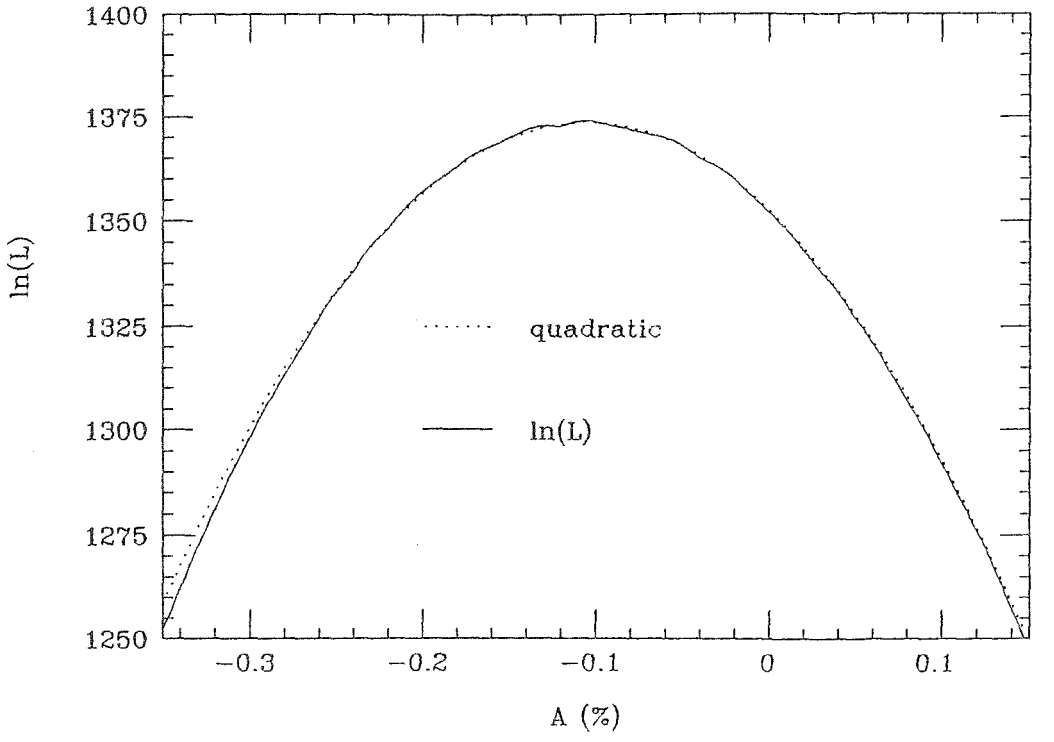

Figure D.1 Maximum likelihood function for fitting the asymmetry in comparison with the gaussian distribution.

For the application in this analysis,

$$f(\theta, A^{Born}) = N\epsilon(\theta)\frac{d\sigma}{d\Omega}. \tag{D.4}$$

where the cross section is given in Eq 4.2, N is the normalization factor, and $\epsilon(\theta)$ is the acceptance. As long as the acceptance is symmetric, *i.e.*, $\epsilon(\theta) = \epsilon(\pi - \theta)$, which is true for our detector up to 1% systematic uncertainty, the normalization factor is independent of the parameter A^{Born} because $\cos\theta$ term does not contribute to the integral. Maximizing the logarithm of the maximum likelihood function, we obtain A^{Born} as the zero of the following equation,

$$\sum_{i=1}^{n} \frac{\cos\theta_i}{C(1+\cos^2\theta_i)(1+\delta(\theta_i)) + A^{Born}\cos\theta_i} = 0. \tag{D.5}$$

To estimate the statistical uncertainty, we may expand $\mathcal{L}$ near the best estimated

value (for simplicity, consider only one parameter),

$$\mathcal{L} \simeq \mathcal{L}_0 exp(-\frac{(p-p_0)^2}{2\sigma_p^2}) \tag{D.6}$$

$$\sigma_p = \left[-\frac{\partial^2(\ln \mathcal{L})}{\partial p^2}\right]^{-1/2} \tag{D.7}$$

It is assumed that gaussian distribution is a good approximation for $\mathcal{L}$ near the maximum, or in other words, $\ln \mathcal{L}$ tends to be parabolic. Fig D.1 shows the maximum likelihood function in comparison with the gaussian distribution when fitting the asymmetry. In this case, the uncertainty is

$$\sigma = \left\{\sum_{i=1}^{n} \frac{\cos^2\theta_i}{[C(1+\cos^2\theta_i)(1+\delta(\theta_i)) + A^{Born}\cos\theta_i]^2}\right\}^{-1/2} \tag{D.8}$$

The maximum likelihood method has many advantages. Because it is based on individual events, there is no need to construct a histogram, and it works for even very low event density. In our case, the dependence of the asymmetry on the acceptance is left out, which can not be avoided by calculating forward-backward events or using a $\mathcal{X}^2$ fit.

D.2 $\mathcal{X}^2$ fit of parameters and testing hypothesis

$\mathcal{X}^2$ fitting is a frequently used procedure to compare an experimental distribution with the theoretical prediction. It is the sum of squared differences weighted by the square of the inverse of the standard deviations:

$$\mathcal{X}^2 = \sum_{i=1}^{n} \left(\frac{y_i^{exp} - y_i^{th}(\mathrm{p})}{\sigma_i}\right)^2, \tag{D.9}$$

where σ_i is the standard deviation of the measurement in the i^{th} bin. The theoretical expression y^{th} may depend on a set of parameters that is to be determined. Minimization of $\mathcal{X}^2$ with respect to the parameters gives the best estimation of the parameters. Mathematically, if y_i^{exp} is a random variable of a gaussian distribution with the mean and variance being y_i^{th} and σ_i^2, $\mathcal{X}^2_{min}$ follows the $\mathcal{X}^2$ distribution with

ν degrees of freedom, where $\nu = n - m$ and m is the number of free parameters allowed to vary in the search for the minimum. If the χ^2 is quadratic in the parameters to be determined, or approximately is, the uncertainty of the parameters can be estimated easily by expanding the χ^2,

$$\chi^2 \simeq \chi^2_{min} + \sum_{i=1,j=1}^{m,m} \frac{1}{2}\frac{\partial^2\chi^2}{\partial p_i \partial p_j}(p_i - p_i^0)(p_j - p_j^0) \qquad (D.10)$$

$$\sigma_{ij} = (\frac{1}{2}\frac{\partial^2\chi^2}{\partial p_i \partial p_j})^{-1} \qquad (D.11)$$

Obviously the errors may be correlated.

In fitting the electroweak parameters using the asymmetry and R-values, the χ^2 distribution happens to be asymmetric. The contour corresponding to a certain confidence level (or the quoted error in case for one parameter) can be obtained by incrementing χ^2 by Δ, The values of Δ are

	68%	95%
1 *parameter*	1.0	3.84
2 *parameters*	2.4	5.99

The χ^2 fit of the experimental data not only gives the estimates of the parameters, but also tells how well the model fits the experimental data. For our fit of electroweak parameters (Eq 4.4), $\chi^2_{min} = 5.7$ with 8 degrees of freedom. The probability of having a χ^2 equal or greater than this value is 68%, which confirms that the theory is quite consistent with the experimental data. This is a very powerful feature of this method in discriminating different theories.

For the applications in this thesis, testing a hypothesis is to derive a constraint on the parameters with 95% confidence level, such as, the limits on the cutoff parameters or the mass of μ^*. This is done in the same fashion as in fitting the parameters except that the boundary is usually open at one end, that is to say, the standard theory is so consistent with the data that there is little room for the extension.

References

[1] S. L. Glashow, Partial-symmetries of weak interaction., *Nucl. Phys.* **22** (1961) 579.

[2] S. Weinberg, A model of leptons., *Phys. Rev. Lett.* **19** (1967) 1264.

[3] A. Salam, Weak and electromagnetic interactions., In N. Svartholm (Almqvist and Wiksell, Stockholm), editor, Elementary particle physics page 367 1968.

[4] E. Fermi, Versuch einer theorie der β–strahlen. I., *Z. Phys.* **88** (1934) 161.

[5] T. D. Lee and C. N. Yang, Questions of parity conservation in weak interactions, *Phys. Rev.* **104** (1956) 254.

[6] C. S. Wu *et al.*, Experimental test of parity conservation in beta decay, *Phys. Rev.* **105** (1957) 1413.

[7] P. W. Higgs, Broken asymmetries, massless particles and gauge fields., *Phys. Lett.* **12** (1964) 132.

[8] P. W. Higgs, Spontaneous symmetry breakdown without massless bosons., *Phys. Rev.* **145** (1966) 1156.

[9] F. J. Hasert *et al.*, Observation of neutrino-like interactions without muon or electron in the Gargamelle neutrino experiment., *Phys. Lett.* **46B** (1973) 138.

[10] F. J. Hasert *et al.*, Observation of neutrino-like interactions without muon or electron in the Gargamelle neutrino experiment., *Nucl. Phys.* **B73** (1974) 1.

[11] The UA1 Collab. G. Arnison *et al.*, Experimental observation of isolated large transverse energy electrons with associated missing energy at $\sqrt{s} = 540$ GeV., *Phys. Lett.* **122B** (1983) 103.

[12] The UA1 Collab. G. Arnison *et al.*, Experimental observation of lepton pairs of invariant mass around 95 GeV/c^2 at the CERN SPS collider., *Phys. Lett.* **126B** (1983) 398.

[13] The UA2 Collab. G. Banner *et al.*, Observation of single isolated electrons of high transverse momentum in events with missing transverse energy at the CERN $\bar{p}p$ collider., *Phys. Lett.* **122B** (1983) 476.

[14] The UA2 Collab. G. Banner *et al.*, Evidence for $Z^0 \rightarrow e^+e^-$ at the CERN $\bar{p}p$ collider., *Phys. Lett.* **129B** (1983) 130.

[15] The UA2 Collab. R. Ansari *et al.*, measurement of W and Z production properties at the CERN $\bar{p}p$ collider., CERN-EP/87-48 1987.

[16] The UA1 Collab. G. Arnison *et al.*, Intermediate vector boson property at the CERN super proton synchrotron collider., *Phys. Lett.* **166B** (1986) 484.

[17] P. G. Reutens *et al.*, Measurement of $\sin^2\theta_w$ and ρ in deep inelastic neutrino-nucleon scattering., *Phys. Lett* **152B** (1985) 404.

[18] J. V. Allaby *et al.*, A precise determination of the electroweak mixing angle from semileptonic neutrino scattering., *Phys. Lett* **177B** (1986) 446.

[19] H. Abramowicz *et al.*, A precision measurement of $\sin^2\theta_w$ from semileptonic neutrino scattering., *Phys. Rev. Lett.* 57 (1986) 298.

[20] C. L. Smith, On the determination of $\sin^2\theta_w$ in semileptonic neutrino interactions., *Nucl. Phys.* B228 (1983) 205.

[21] L. A. Ahrens *et al.*, Measurements of the ratio of cross sections for neutrino and antineutrino scattering from electrons., *Phys. Rev. Lett.* 54 (1985) 18.

[22] J. V. Allaby *et al.*, A new measurement of the ratio of the cross sections of muon-neutrino and muon antineutrino scattering on electrons., *Phys. Lett* 177B (1986) 446.

[23] D. Yu. Bardin and V. A. Dokuchaeva, On the radiative corrections to the neutrino deep inelastic scattering., JINR–E2–86–260 1986.

[24] R. C. Allen *et al.*, First observation and cross section measurement of $\nu_e + e^- \rightarrow \nu_e + e^-$., *Phys. Lett.* 55 (1985) 2401.

[25] B. Kayser *et al.*, Charged and neutral current interference in ν_e–e scattering., *Phys. Rev. D* 20 (1979) 87.

[26] C. Y. Prescott *et al.*, Further measurements of parity non-conservation in inelastic electron scattering., *Phys. Lett.* 84B (1979) 524.

[27] A. Barroso *et al.*, Electroweak radiative corrections at LEP energies., CERN-EP/87-70 1987.

[28] F. A. Berends and R. Kleiss, Distributions in the process $e^+e^- \rightarrow \mu^+\mu^-(\gamma)$., *Nucl. Phys.* B177 (1981) 237.

[29] M. Boehm and W. Hollik, Electroweak radiative corrections to the $e^+e^- \rightarrow \mu^+\mu^-$ asymmetry., *Phys. Lett.* 139B (1984) 213.

[30] F. A. Berends, R. Kleiss, and S.Jadach, Radiative corrections to muon pair and quark prodction in electron-positron collision in the Z^o region., *Nucl. Phys.* B202 (1982) 63.

[31] F. A. Berends, R. Kleiss, and S. Jadach, Monte Carlo simulation of radiative corrections to the processes $e^+e^- \to \mu^+\mu^-$ and $e^+e^- \to \bar{q}q$ in the Z° region., *Comp. Phys. Comm.* **29** (1983) 185.

[32] W. Wetzel, Electroweak radiative corrections for $e^+e^- \to \mu^+\mu^-$ at PETRA energies, Heidelberg preprint HD-THEP-82-18 1983.

[33] W. Hollik and H.–J. Timme, Renormalization scheme dependence of electroweak radiative corrections., *Z. Phys. C* **333** (1986) 125.

[34] G. 't Hooft, Renormalizable lagrangians for massive Yang-Mills fields., *Nucl. Phys.* **B35** (1971) 167.

[35] M. Boehm, W. Hollik, and H. Spiesberger, The renormalization of the electroweak standard model., DESY Preprint DESY 84-027 1984.

[36] Y. S. Tsai, Radiative corrections to e^+e^- reactions to all orders in α using renormalization group., SLAC Preprint SLAC-PUB-3129 1983.

[37] PETRA Proposal (Updated Version)., DESY 1976.

[38] the MARK J Collab. D. P. Barber *et al.*, Physics with high energy electron-positron colliding beams with the MARK J detector (1st year at MARK J)., *Phys. Rep.* **63** (1980) 337.

[39] the MARK J Collab. B. Adeva *et al.*, A summary of recent experimental results from MARK J: high energy e^+e^- collisions at PETRA., *Phys. Rep.* **109** (1984) 131.

[40] M. C. Ho, The trigger and data taking system of the MARK J detector., PhD thesis NIKHEF, Amsterdam 1983.

[41] F. A. Berends and R. Kleiss, Distributions for electron-positron annihilation into two and three photons., *Nucl. Phys.* **B178** (1981) 41.

[42] The UA2 Collab. R. Ansari *et al.*, Measurement of the standard model parameters from a study of W and Z bosons., *Phys. Lett.* **186B** (1987) 440.

[43] E. J. Eichten, K. D. Lane, and M. E. Peskin, New tests for quark and lepton substructure., *Phys. Rev. Lett.* **50** (1983) 811.

[44] V. Barger, W. Y. Keung, and Ernest Ma, Gauge model with light W and Z bosons., *phys. Rev.* **22D** (1980) 727.

[45] E. H. de Groot, G. J. Gounaris, and D. Schildknecht, Possible structures of the neutral current within a gauge theory framework., *Z. Phys. C* **5** (1980) 127.

[46] E. H. de Groot, G. J. Gounaris, and D. Shildknecht, General electroweak mixing models and extended gauge theories., *Z. Phys. C* **10** (1981) 55.

[47] P. H. W. M. Daverveldt, Monte Carlo simulation of two-photon processes., PhD thesis Leiden 1983.

[48] F. E. Low, Heavy electrons and muons, *Phys. Rev. Lett.* **14** (1965) 238.

[49] CELLO Collab. H. J. Behrend *et al.*, An investigation of the process $e^+e^- \rightarrow \mu^+\mu^-\gamma$., *Phys. Lett.* **158B** (1985) 536.

[50] F. M. Renard, Limits on masses and couplings of excited electrons and muons., *Phys. Lett.* **116B** (1982) 264.

[51] F. Combley, F. J. M. Fairley, and E. Picasso, The CERN muon (g-2) experiment., *Phys. Rep.* **68** (1981) 94.

[52] T. Kinoshita, B. Nižić, and Y Okamoto, Improved theory of the muon anomalous magnetic moment., *Phys. Rev. Lett.* **52** (1984) 717.

[53] The CELLO Collab. H. J. Behrend *et al.*, Measurement of the reaction e^+e^- $\rightarrow \mu^+\mu^-$ for $14 \leq \sqrt{s} \leq 36.4$ GeV., *Z. Phys. C* **14** (1982) 283.

[54] The CELLO Collab. H. J. Behrend *et al.*, A measurement of the muon pair production in e^+e^- annihilation at $38.3 \leq \sqrt{s} \leq 46.8$ GeV., DESY Preprint DESY 87-005 1987.

[55] The JADE Collab. W. Bartel *et al.*, New results on $e^+e^- \rightarrow \mu^+\mu^-$ from the JADE detector at PETRA., *Z. Phys. C* **26** (1985) 507.

[56] The PLUTO Collab. Ch. Berger *et al.*, Tests of the standard model with lepton pair production in e^+e^- reactions., *Z. Phys. C* **27** (1985) 341.

[57] TASSO Collab. R. Brandelik *et al.*, Charge asymmetry and weak interaction effects in $e^+e^- \rightarrow \mu^+\mu^-$ and $e^+e^- \rightarrow \tau^+\tau^-$., *Phys. Lett.* **110B** (1982).

[58] TASSO Collab. M. Althoff *et al.*, An inproved measurement of electroweak couplings from $e^+e^- \rightarrow e^+e^-$ and $e^+e^- \rightarrow \mu^+\mu^-$., *Z. Phys. C* **22** (1984).

[59] HRS Collab. M. Derrick *et al.*, New results on the reaction $e^+e^- \rightarrow \mu^+\mu^-$ at $\sqrt{s} = 29$ GeV., *Phys. Rev.* **31D** (1985) 2352.

[60] MAC Collab. W. W. Ash *et al.*, Precision measurement of electroweak effects in $e^+e^- \rightarrow \mu^+\mu^-$ at $\sqrt{s} = 29$ GeV., *Phys. Rev. Lett.* **55** (1985) 1831.

[61] MARK II Collab M. E. Levi *et al.*, Weak neutral currents in e^+e^- collisions at $\sqrt{s} = 29$ GeV., *Phys Rev. Lett.* **51** (1983) 1941.

[62] B. Naroska, e^+e^- physics with the JADE detector at PETRA., *Phys. Rep.* **148** (1987) 67.

[63] L. A. Ahrens *et al.*, Measurement of neutrino-proton and antineutrino-proton elastic scattering., *Phys. Rev. D* **35** (1987) 785.

[64] E. N. Fortson and L. L. Lewis, Atomic parity nonconservation experiments., *Phys. Rep.* **113** (1984) 289.

[65] Ugo Amaldi *et al.*, A comprehensive analysis of data pertaining to the weak neutral current and the intermediate vector boson masses., UPR–0331T 1987.

[66] JADE Collab. W. Bartel *et al.*, Observation of radiative e^+e^- annihilation into $\mu^+\mu^-\gamma$ and $\mu^+\mu^-\gamma\gamma$., *Z. Phys. C* **24** (1984) 223.

[67] CELLO Collab. H. J. Behrend *et al.*, Excited lepton search., *Phys. Lett.* **168B** (1986).

[68] MAC Collab. W. T. Ford *et al.*, Experimental test of higher-order QED and a search for excited muon states., *Phys. Rev. Lett.* **51** (1983) 257.

[69] J. Ellis and R. Peccei, Physics at LEP., CERN 86-02 1986.

[70] B. Schrempp *et al.*, Bounds on new contact interactions from future e^+e^- colliders., CERN 87-34 1987.